ELECTRONIC, MAGNETIC AND OPTICAL PROPERTIES OF ATOMICALLY CONTROLLED COMPLEX OXIDE HETEROSTRUCTURES AND INTERFACES

XIAO WANG

NATIONAL UNIVERSITY OF SINGAPORE

2012

ELECTRONIC, MAGNETIC AND OPTICAL PROPERTIES OF ATOMICALLY CONTROLLED COMPLEX OXIDE HETEROSTRUCTURES AND INTERFACES

XIAO WANG

(B.Sc, Shandong University, P.R. China)

A THESIS SUBMITTED

FOR THE DEGREE OF DOCTOR OF PHILOSOPHY IN SCIENCE

DEPARTMENT OF PHYSICS

NATIONAL UNIVERSITY OF SINGAPORE

2012

DECLARATION

I hereby declare that the thesis is my original work and it has been written by me in its entirety. I have duly acknowledged all the sources of information which have been used in the thesis.

This thesis has also not been submitted for any degree in any university previously.

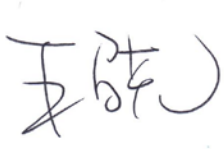

Xiao Wang

7 August 2012

TABLE OF CONTENTS

ACKNOWLEDGEMENTS

I would first like to express my thanks to my Ph.D. thesis advisor Dr. Ariando, who in my opinion is the best thesis advisor and friend I could ever imagine. Back to the days when I was about to choose a thesis advisor, I clearly remember that he told me “we are colleagues”. This attitude catalyzed my choice and time proved that this is one of the best choices I have ever made in my life. Integrity, gentleness, hardworking, humbleness, enthusiasm, humorous wisdom, carefulness and especially *thinking big* are the words that come to my mind when I think of him and these are also the virtues I always want to learn from him. To me, the Ph.D. period is all about developing the correct research habits and Dr. Ariando just helped me so much that I could never thank him enough. So, I want to thank him again and wish him a brilliant future. I also want to thank my Ph.D. thesis co-advisor Prof. T. Venky Venkatesan. Apart from being a successful senior, he is also kind, accessible and willing to encourage young people. I am grateful for all the knowledge and thinking techniques that he taught me. Besides research skills that he passed on to me, thinking big and thinking positive are two life-long treasures I received from him. “Be enthusiastic” and “Work hard and work smart as sky is the limit” were the two sentences Prof. Venky gave to me. The philosophy behind these two sentences inspired me during my Ph.D. period and will continue to inspire me even beyond this period. I also want to express my thanks to Prof. Hans Hilgenkamp. He accepted me for a two-month internship at the University of Twente, where I learned experimental skills and obtained valuable data. Besides that, Prof. Hans Hilgenkamp also helped me to successfully apply for the Rubicon grant and I thank him for his time and effort. I also thank our department head Prof. Feng Yuanping, who brought me to this wonderful place by recruiting me 4 years ago. I also thank the recommendation letter for my Rubicon grant application from him, even though he was very

busy with a conference at that time. As a student, it is a big honor to get in touch with the department head and to receive recommendation letters.

My special thank goes to my family too. I am sorry that I chose to study abroad and left my mother alone at our hometown. She never complained at all and also very frequently reminded me to take good care of my health and safety. I certainly wish I could have been around with my mother and be of help to her when days were difficult. I also want to thank my younger brother who brought me lot of joy and laughter throughout these years. As a hardworking good boy, he is also an idol from whom I can learn a lot.

To my colleagues, collaborators and friends, Dr. Weiming Lü, Dr. Huang Zhen, Zhiqi Liu, Anil Annadi, Denise P. Leusink, Dr. Daniel Lubrich, Mallikarjunarao Motapothula, Jeroen Huijben, Dr. Arkajit Roy Barman, Dr. Xuepeng Qiu, Dr. Sankar Dhar, Dr. Lanfei Xie, Dr. Jiabo Yi, Tom Wijnands, Wentao Xu, Dr. Kalon Gopinadhan, Prof. Alexander Brinkman, Asst. Prof. Wei Chen, Prof. Ganaphathy Baskaran, Assoc. Prof. Jun Ding, Asst. Prof. Andrivo Rusydi, Joost Beukers, Jae Sung Son, Yongliang Zhao, Teguh Citra Asmara, Tarapada Sarkar, Dr. Guanjun You, Changjiang Li, Amar Srivasta, Naomi Nadakumar and all the other great people I met in these years: I thank everybody for the experimental and also emotional support. In days when I sought discussion and in days when I needed comfort, their unselfish help touched and encouraged me a lot.

My Ph.D. period has been a fruitful and happy period. I am extremely happy for all the things I was able to explore, such as research, 3 dimensional graphics, video editing and ASP.net. I thank the Physics Department of National University of Singapore (NUS) for providing me with a Research Scholarship, so that I could spend all my time in research.

With so much support and encouragements, I will certainly work hard and work smart in the future.

At last, may everyone mentioned here and NUS have a great future ahead!

Xiao Wang

2012.03

ABSTRACT

Owing to the strong interplay between charge, spin and orbital degree of freedom in complex oxides, new properties can emerge at the interfaces of atomically flat oxide heterostructures, because of the inherent discontinuities at the interfaces. Understanding the driving mechanism behind these emerging properties will allow us to control and use them in novel multifunctional oxide-based devices. The main objective of this thesis is to explore and understand possible new phenomena in various oxide heterostructures based on high quality $LaAlO_3$ (LAO) and $La_{0.5}Sr_{0.5}TiO_3$ (LSTO) films grown layer-by-layer by Pulsed Laser Deposition (PLD) on various single-terminated substrates with the help of *in-situ* Reflection High Energy Electron Diffraction (RHEED).

To study the role of defects in the $LaAlO_3/SrTiO_3$ (LAO/STO) heterostructures, static and ultrafast dynamics of defects in STO were optically investigated for samples prepared at low oxygen partial pressures. Using ultraviolet-visible-infrared and femtosecond laser spectroscopy, the transmittance, transient absorption and relaxation times for various transitions were determined. The relaxations are discussed on the basis of a proposed defect-band diagram which can be attributed mainly to the presence of dominant oxygen defects in STO substrate.

Magnetoresistance (MR) study on the LAO/STO heterostructure was conducted to investigate the influence of magnetic ordering, interface scattering and dimensionality. Magnetoresistance anisotropy at LAO/STO interfaces was compared between samples prepared in high and low oxygen partial pressures. By varying the measurement temperature and magnetic field orientation with respect to the film surface, this study demonstrates that

MR can be used to distinguish the dimensionality of the charge transport and various (phonon, magnetic center and interface boundary) scattering processes in this system.

Using a superconducting quantum interference device (SQUID) magnetometer, magnetic properties of LAO/STO interfaces were studied. For the first time, electronic phase separation (EPS) was demonstrated in this system, where the interface charges are separated into regions of a two-dimensional electron gas, a ferromagnetic phase, which persists even above room temperature, and a diamagnetic/paramagnetic phase below 60 K. The EPS is attributed to the selective occupancy of interface subbands of the nearly degenerate Ti orbital in the STO.

To explore new type of interfaces and to understand the driving mechanisms behind the emerging properties in LAO/STO, LSTO thin films, which have frustrated valences of Ti^{3+} and Ti^{4+} similar to the interface of the LAO/STO system, were prepared on different substrates. LSTO/STO interfaces interestingly exhibit both a 3D Fermi electron liquid and a 2D electron gas. This two channel conducting model was verified by the observed nonlinear Hall resistance and by fitting its dependence on film thickness, temperature and back gate voltage. On further reduction of the thickness, LSTO showed a metallic to insulator (MIT) transition. Based on the properties of LSTO prepared on various substrates with different lattice constants, this MIT can be attributed to the interface strain effect.

These results provide insight into the possible driving mechanisms of the emerging properties at oxide interfaces and demonstrate a novel conducting system with potentially new physics and possible applications.

LIST OF PUBLICATIONS

Articles

1. Ariando*, X. Wang*, G. Baskaran, Z.Q. Liu, J. Huijben, J.B. Yi, A. Annadi, A. Roy Barman, A. Rusydi, S. Dhar, Y.P. Feng, J. Ding, H. Hilgenkamp, and T. Venkatesan. *"Electronic phase separation at the $LaAlO_3/SrTiO_3$ interface"*, **Nature Communications** 2, 188 (2011). (* both authors contribute equally)

2. X. Wang, W.M. Lü, A. Annadi, Z.Q. Liu, K. Gopinadhan, S. Dhar, T. Venkatesan, and Ariando. "*Magnetoresistance of 2D and 3D electron gas in $LaAlO_3/SrTiO_3$ heterostructures: Influence of Magnetic Ordering, Interface Scattering and Dimensionality"*, **Phys. Rev. B.** 84, 075312 (2011).

3. X. Wang, J.Q. Chen, A. Roy Barman, S. Dhar, Q-H. Xu, T. Venkatesan, and Ariando. "*Static and ultrafast dynamics of defects of $SrTiO_3$ in $LaAlO_3/SrTiO_3$ heterostructures"*, **Appl. Phys. Lett.** 98, 081916 (2011).

(selected for the March 2011 issue of Virtual Journal of Ultrafast Science - **Virt. J. Ultrafast Sci.,Vol. 10, Issue 3**/Condensed Matter Physics)

4. W.M. Lü, X. Wang, Z.Q. Liu, S. Dhar, A. Annadi, K. Gopinadhan, A. Roy Barman, T. Venkatesan, Ariando. **"***Metal-insulator transition at a depleted $LaAlO_3/SrTiO_3$ interface: evidence for charge transfer variations induced by $SrTiO_3$ phase transitions"*, **Appl. Phys. Lett.** 99, 172103 (2011). *(Journal highlight)*

5. Lanfei Xie, Xiao Wang, Hongying Mao, Rui Wang, Mianzhi Ding, Yu Wang, Barbaros Ozyilmaz, Kian Ping Loh, Andrew T. S. Wee, Ariando, and Wei Chen. "*Electrical measurement of non-destructively p-type doped graphene using molybdenum trioxide"*, **Appl. Phys. Lett.** 99, 012112 (2011).

6. J.Q. Chen, X. Wang, Y.H. Lu, A.R. Barman, S. Dhar, Y.P. Feng, Ariando, Q.H. Xu, and T. Venkatesan. "*Defect dynamics and spectral observation of twinning in single crystalline $LaAlO_3$ under sub-bandgap excitation",* **Appl. Phys. Lett.** 98, 041904 (2011).

7. Lanfei Xie, Xiao Wang, Jiong Lu, Zhenghua Ni, Zhiqiang Luo, Hongying Mao, Rui Wang, Yingying Wang, Han Huang, Dongchen Qi, Rong Liu, Ting Yu, Zexiang Shen, Tom Wu, Haiyang Peng, Barbaros Ozyilmaz, Kianping Loh, Andrew T. S. Wee, Ariando, and Wei Chen. "*Room temperature ferromagnetism in partially hydrogenated epitaxial graphene",* **Appl. Phys. Lett.** 98, 193113 (2011).

8. Z.Q. Liu, D.P. Leusink, Y.L. Zhao, X. Wang, X.H. Huang, W.M. Lü, A. Srivastava, A. Annadi, S.W. Zeng, K. Gopinadhan, S. Dhar, T. Venkatesan, Ariando. *"Metal-insulator transition in $SrTiO_{3-x}$ thin film induced by frozen-out carriers",* **Phys. Rev. Lett.** 107, 146802 (2011).

9. Z.Q. Liu, D.P. Leusink, W.M. Lü, X. Wang, X.P. Yang, K. Gopinadhan, L.Y. Teng, Y.L. Zhao, A. Annadi, A. Roy Barman, S. Dhar, Y.P. Feng, H.B. Su, G. Xiong, T. Venkatesan, Ariando. *"Resistive switching mediated by the formation of quasi conduction band in a large band gap insulating oxide",* **Phys. Rev. B.** 84, 165106 (2011).

10. S. Dhar, A.R. Barman, G.X. Ni, X. Wang, X.F. Xu, Y. Zheng, S. Tripathy, Ariando, A. Rusydi, K.P. Loh, M. Rubhausen, A.H. Castro Neto, B. Ozyilmaz, and T. Venkatesan. "*A New Route to Graphene Processing by Selective Laser Ablation",* **AIP Advances** 1, 022109 (2011).

11. X.H. Huang, Z.Y. Zhan, X. Wang, Z. Zhang, G. Z. Xing, D. L. Guo, D. P. Leusink, L. X. Zheng, and T. Wu. "*Rayleigh-instability-driven simultaneous morphological and compositional transformation from Co nanowires to CoO octahedral",* **Appl. Phys. Lett.** 97, 203112 (2010).

12. Z. Q. Liu, Z. Huang, W. M. Lü, K. Gopinadhan, X. Wang, A. Annadi, T. Venkatesan, and Ariando. *"Atomically flat interface between a single-terminated $LaAlO_3$ substrate and $SrTiO_3$ thin film is insulating"*, **AIP Advances** 2, 012147 (2012).

13. T. Wang, Z. Yang, P. Dong, J. D. long, X. Z. He, X. Wang, K. Z. Zhang, and L. W. Zhang. *"Electrical shielding box measurement of the negative hydrogen beam from Penning ion gauge ion source"*, **Review of Scientific Instruments** 83, 063302 (2012).

14. Z. Q. Liu, W. M. Lü, X. Wang, Z. Huang, A. Annadi, S. W. Zeng, T. Venkatesan, and Ariando. "*Magnetic-field induced resistivity minimum with in-plane linear magnetoresistance of the Fermi liquid in $SrTiO_{3-x}$ single crystals"*, **Phys. Rev. B** 85, 155114 (2012).

15. S.W. Zeng, X. Wang *et al*., "*Metallic state in La-doped $YBa_2Cu_3O_y$ thin films with n-type charge carriers"*, **Phys. Rev. B** 86, 045124 (2012).

16. S.W. Zeng, Z. Huang, X. Wang *et al*., "*The influence of La substitution and oxygen reduction in ambipolar La-doped $YBa_2Cu_3O_y$ thin films"*, **Superconductor Science and Technology** 25, 124003 (2012).

17. S.W. Zeng, X. Wang *et al*., "*Metallic state in La-doped $YBa_2Cu_3O_y$ thin films with n-type charge carriers"*, **Phys. Rev. B** 86, 045124 (2012).

18. Ram Sevak Singh, Xiao Wang, Wei Chen, Ariando, and Andrew T. S. Wee, "*Large room-temperature quantum linear magnetoresistance in multilayered epitaxial graphene: Evidence for two-dimensional magnetotransport*", **Appl. Phys. Lett.** 101, 183105 (2012).

19. Z. Q. Liu, Y. Ming, W. M. Lu, Z. Huang, X. Wang, B. M. Zhang, C. J. Li, K. Gopinadhan, S. W. Zeng, A. Annadi, Y. P. Feng, T. Venkatesan, and Ariando, "*Tailoring the electronic properties of $SrRuO_3$ films in $SrRuO_3/LaAlO_3$ superlattices*", **Appl. Phys. Lett.** 101, 223105 (2012).

20. A. Annadi, A. Putra, Z. Q. Liu, X. Wang, K. Gopinadhan, Z. Huang, S. Dhar, T. Venkatesan, and Ariando, "*Electronic correlation and strain effects at the interfaces between polar and nonpolar complex oxides*", **Phys. Rev. B** 86, 085450 (2012).

21. A. Annadi, A. Putra, A. Srivastava, X. Wang, Z. Huang, Z. Q. Liu, T. Venkatesan, and Ariando, "*Evolution of variable range hopping in strongly localized two dimensional electron gas at $NdAlO_3/SrTiO_3$ (100) heterointerfaces*", **Appl. Phys. Lett.** 101, 231604 (2012).

22. X. Wang, *et al.*, "*Coexistence of 3D Fermi electron liquid and a 2D electron gas in a $La_{0.5}Sr_{0.5}TiO_3/SrTiO_3$ heterostructure*", to be submitted.

Patents

1. **US Provisional Patent** No. 61/286,092 (14 December 2009)

Synthesis of specific number of graphene layers by thickness selective laser ablation.

T. Venkatesan, S. Dhar, A. R. Barman, X. Wang, Ariando, B. Oezyilmaz.

2. **US Provisional Patent** No. 61/404,975 (12 October 2010)

Fabrication of room-temperature ferromagnetic graphene by surface modification with high work function metal oxides.

Chen Wei, Xie Lanfei, Wang Xiao, Sun Jiatao, Ariando, Andrew Wee T S.

3. **Singapore Patent** PCT/SG2011/000177 (05 May 2011)

Surface transfer hole doping of epitaxial graphene using high work function metal oxide thin film.

Chen Wei, Xie Lanfei, Wang Xiao, Sun Jiatao, Ariando, Andrew Wee T S.

4. **Brazil Patent Application** No. BR 11 2012 028292-1, ILO Ref: 10133N-PCT/BR

Hole Doping of Graphene

Chen Wei, Xie Lanfei, Wang Xiao, Sun Jiatao, Ariando, Andrew Wee T S.

5. **US Patent Application** No. 13/696,189, ILO Ref: 10133N-PCT/US

Hole Doping of Graphene

Chen Wei, Xie Lanfei, Wang Xiao, Sun Jiatao, Ariando, Andrew Wee T S.

6. **Singapore Patent Application**, ILO Ref: 10133N-PCT/SG

Hole Doping of Graphene

Chen Wei, Xie Lanfei, Wang Xiao, Sun Jiatao, Ariando, Andrew Wee T S.

7. **Japan Patent Application**, ILO Ref: 10133N-PCT/JP

Hole Doping of Graphene

Chen Wei, Xie Lanfei, Wang Xiao, Sun Jiatao, Ariando, Andrew Wee T S.

Conferences

1. **ICMAT, Singapore.** (2009.06)

   (*Oral presentation & poster*: Femto-second laser excitation studies of oxide thin films and heterostructures)

2. **WOE 16, Tarragona, Spain.** (2009.10)

3. **APS March Meeting, Portland, USA.** (2010.03)

   (*Oral presentation I*: Signature of Phase Separation in $LaAlO_3/SrTiO_3$ from Magnetoresistance Studies & *Oral presentation II*: Structural and dynamical studies of the $LaAlO_3/SrTiO_3$ interface)

4. **Institute of Physics Singapore Meeting 2011, Singapore** (2011.02)

   (*Oral presentation:* Electronic Phase Separation at $LaAlO_3/SrTiO_3$ Interfaces)

5. **ICMAT, Singapore.** (2011.06)

(*Oral presentation*: Magnetoresistance Anisotropy in $LaAlO_3/SrTiO_3$ Interfaces)

6. ISOE 2011, Corsica, France. (2011.10)

(*Poster*: Electronic Phase Separation at $LaAlO_3/SrTiO_3$ Interfaces)

7. 5th MRS-S conference on Advanced Materials, Singapore. (2012.03)

(*Poster I:* Atomic Charge Modulation in the La Doped $SrTiO_3$ Thin Film & *Poster II:* Electronic Phase Separation and Magnetoresistance Studies at the LAO/STO Interface)

8. Frontiers in Electronic Materials: Correlation Effects and Memristive Phenomena, Aachen, Germany. (2012.06)

(*Oral presentation*: Is It Possible for a $La_{0.5}Sr_{0.5}TiO_3$ Fermi Liquid to Exist in a Confined Two-dimensional System? & *Poster*: Is It Possible for a $La_{0.5}Sr_{0.5}TiO_3$ Fermi Liquid to Exist in a Confined Two-dimensional System?)

LIST OF TABLES

LIST OF FIGURES

LIST OF SYMBOLS

R	Resistance
ρ	Resistivity
R_s	Sheet resistance
σ	Conductivity
HR	Hall resistance
T	Temperature
K	Kelvin
t	Time
V	Voltage
V_g	Gate voltage
e	Electronic charge
I	Current
M	Magnetization
H	Magnetic field
n	Carrier density without thickness normalization
μ	Carrier Hall mobility
ps	picosecond
fs	femtosecond
BBO	β-barium borate
uc	Unit cell
CMOS	Complementary metal-oxide-semiconductor
2DEG	Two dimensional electron gas
PLD	Pulsed laser deposition
P_{O2}	Oxygen partial pressure
ΔT/T	Normalized transmission change
CB	Conduction band
VB	Valence band
UV-Vis-NIR	Ultra violet- visible-near infrared
OD	Optical density
SIMS	Secondary ion mass spectrometry
SQUID	Superconducting quantum interference device

PPMS	Physical properties measurement system
LAO	Lanthanum aluminium oxide
STO	Strontium titanium oxide
LSAT	$(LaAlO_3)_{0.3}(Sr_2AlTaO_6)_{0.7}$ (001)
NGO	$NdGaO_3$ (110)
LSTO	50% Lanthanum doped Strontium Titanate
RHEED	Reflection high energy electron diffraction
MR	Magnetoresistance
STM	Scanning tunneling microscopy
SIMS	Secondary ion mass spectrometry

Chapter 1 Introduction

1.1 Introduction

In the past half century, semiconductor technology has been one of the biggest driving forces of modern industries and has changed many aspects of our lives. With progression of time, silicon technology embracing Moore's law is now in the nanotechnology regime with the transistor dimensions approaching 10 and 5 nm in the year 2015 and 2020 respectively [1, 2]. As the transistor size reaches nano dimensions, quantum phenomena impose challenges on the conventional complementary metal-oxide-semiconductor (CMOS) design. In the next decades, further reduction in size of transistors is expected to hit a wall. In order to beat Moore's law, we need numerous breakthroughs in material technology. Furthermore, our growing demand for more intelligent, user-friendly products requires additional functions from a single device. Devices based merely on conventional silicon cannot meet the growing diverse demand anymore and this thus creates an opportunity for new classes of materials.

Among various interesting material systems, complex oxide, which is a class of oxide compounds containing three or more elements, is particularly interesting and promising. Resistive switching [3], high temperature superconductivity [4], diluted magnetic semiconductor oxides and colossal magnetoresistance (MR) [5], all observed in complex oxides have been heavily studied for their intriguing physics as well as the potential for multifunctional devices. Furthermore, complex oxides usually respond actively to external stimuli (*e.g.* electric field [6], magnetic field [5] and strain [7]), showing potential for increasing the functionalities of devices. Recently, controlled synthesis of oxide materials

has reached an unprecedented level of precision at the atomic scale paving the way to exploit novel properties arising from such engineered interfaces [8-13].

Exploration of novel properties at atomically engineered interfaces and heterostructures of complex oxides has become an exciting area of research. In 2004, a conducting two dimensional electron gas (2DEG) was demonstrated at the atomically abrupt interface between two insulators $LaAlO_3$ (LAO) and $SrTiO_3$ (STO) by Ohtomo and Hwang [9]. After this breakthrough, intensive studies have been conducted [8–13] to explore different interface material systems, mechanisms and possible devices. The observation of the 2DEG at the interface between two insulators is extremely interesting because it demonstrates the possibility of generating new properties at interfaces that do not exist in either of the bulk materials. However to fully utilize these materials and structures, exploration of the properties, understanding of the underlying mechanisms and novel designs of possible devices are needed.

This chapter aims to give an overview of my research topic throughout my graduate studies. Firstly, a general description will be given on the properties of perovskites, which form an important class of crystalline complex oxides, followed by an introduction to several well-studied examples. Secondly, a literature review on materials will be given. Finally, the purpose of the research and key results of my studies will be briefly discussed.

1.2 Perovskite Oxide and Interfaces

1.2.1 Perovskite Oxides

Perovskite oxide is a class of complex oxides with the general chemical formula of ABX_3 with the element X in the face centers originates from calcium titanium oxide ($CaTiO_3$) and is named after the Russian mineralogist L. A. Perovski (1792 - 1856) [14]. The perovskite oxide has a cubic or pseudo cubic structure. In Fig 1.1, an ideal cubic perovskite structure is shown where 'A' is a cation generally larger in size than the 'B' cation and X is an anion (generally oxygen) that bonds to both the 'A' and 'B' cations. In terms of symmetry, this cubic-symmetry structure has the 'B' cation in a 6-fold coordination, surrounded by an octahedron of anions, and the 'A' cation in a 12-fold cuboctahedral coordination.

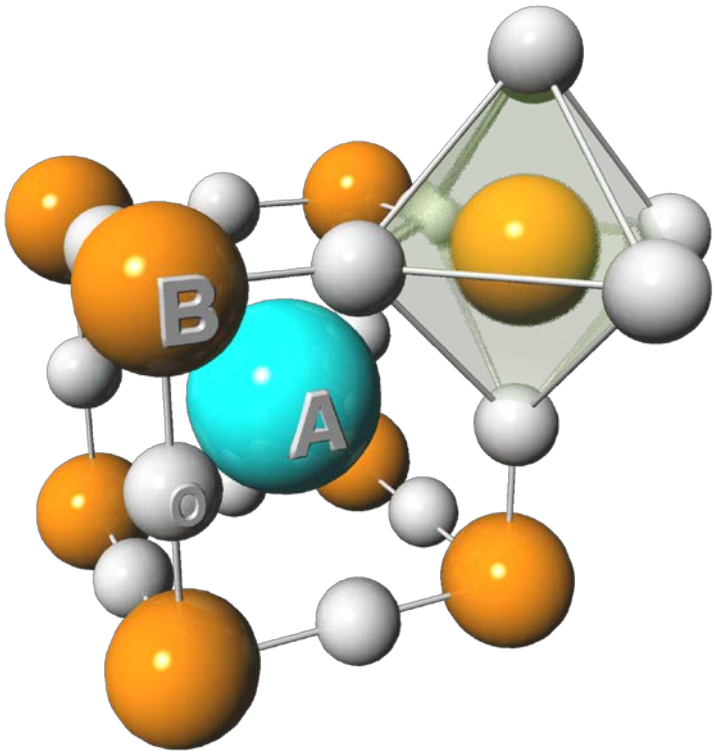

Figure 1. 1: *A sketch of an ideal cubic perovskite structure. The gray spheres are usually oxygen, the orange B-atoms and the ligh blue A-atoms. The light green octahedron surrounded by oxygen is the fingerprint octahedron in perovskite structure.*

Along the [001] direction, the ABO_3 perovskite unit cell (uc) can be considered as two sub-unit-cells or sublayers: AO and BO_2. Depending on the valence of the cations and the total charge states of these sublayers, the perovskite can be considered as non-polar and polar. For instant, $A^{2+}B^{4+}O_3$ is a non-polar perovskite with neutral sublayer stacking of $(AO)^0$ – $(BO_2)^0$ – $(AO)^0$ – $(BO_2)^0$ where A valence is 2+ and B 4+. However, $A^{3+}B^{3+}O_3$ is a polar perovskite with non-neutral sublayer stacking of $(AO)^{1+}$ – $(BO_2)^{1-}$ – $(AO)^{1+}$ – $(BO_2)^{1-}$ where A valence is 3+ and B 3-. The non-polar and polar properties can lead to interesting properties at the interface between perovskite materials due to charge discontinuity and it will be discussed in details later.

Owing to the complexity of structural transitions and subtle interactions between charge, orbital, spin and external energies, perovskite materials can exhibit many intriguing properties [15, 16], such as colossal MR, ferroelectricity, superconductivity, charge ordering, electronic phase separation, spin dependent transport and high thermopower. In this thesis, STO, LAO, LTO and $La_{0.5}Sr_{0.5}TiO_3$ (LSTO), four basic materials, have been extensively studied and utilized for interfaces. In the following, these four material systems will be introduced.

STO is a band insulator with a band gap of around 3.2 eV and a lattice constant of 3.905 Å. The STO crystal is a very important substrate material for oxide research and a lot of applications in other fields. For example, it has been utilized as a grain-boundary barrier layer capacitor [17], oxygen gas sensor [18] and a key substrate for epitaxial growth of high temperature superconducting thin films [19]. STO has a cubic to tetragonal phase transition at around 105 K, a tetragonal to orthorhombic phase transition at around 60 K and another orthorhombic to rhombohedral phase transition at around 30 K [20–22]. The presence of

defects is an important issue for complex oxides. Oxygen vacancies are easily to be induced in STO by thermal annealing in vacuum or ion milling [23–27]. STO with a low concentration of oxygen vacancies has a gray color, and the color changes to dark blue or even black when the oxygen vacancy concentration increases. Photoluminance can also be induced by oxygen vacancies in STO [27, 28].

LAO is also a band insulator with a band gap of 5.6 eV and a lattice constant of 3.791 Å. Similar to STO, LAO serves also as an important substrate for the growth of many oxide materials, such as $YBa_2Cu_3O_7$ (YBCO) and TiO_2 [29]. Although both LAO and STO have a perovskite structure, LAO maintains a rhombohedral phase at room temperature and transforms into a cubic phase at temperatures above 875 K [30, 31]. Due to the rhombohederal phase at room temperature, LAO develops mesoscopic twin structures that are visible to the naked eye.

In contrast with the previous two materials, LTO is a Mott insulator with an optical band gap of 0.2 eV due to electron correlations [32]. It has the orthorhombic perovskite structure with a = 3.97 Å at room temperature [33–35]. LTO is a magnetic material with a G-type antiferromagnetic ordered ground state and a Néel temperature of approximately 146 K [36]. LTO is a semiconductor at high temperatures and an antiferromagnetic insulator below the Néel temperature. Depending on the oxygen stoichiometry, the transport properties of $LaTiO_{3+x}$ can vary from insulating to metallic.

Doping which can be used to modify not only the conductivity but also many other properties is an important technique in complex oxide research. $La_xSr_{1-x}TiO_3$ is also a perovskite-like complex oxide in which a number of *3d* electrons can be varied from 0 to 1

with a change of x from 0 (STO) to 1 (LTO). So La substitutes Sr and acts as an electron donor. $La_{1-x}Sr_xTiO_3$ can be metallic ($x \leq 0.70$) or semiconducting ($x \geq 0.90$). In addition, there is a quadratic temperature dependence of the resistivity for metallic behavior over a wide temperature range indicating that the strong electron-electron scattering process dominates the electron-phonon scattering process. The crystal structure of $La_{1-x}Sr_xTiO_3$ varies with La concentration as well. Depending on the La concentration, $La_{1-x}Sr_xTiO_3$ belongs to the orthorhombic space groups *Pbnm* ($x \leq 0.30$) and *Ibmm* ($0.30 < x < 0.80$), or the cubic space group *Pm3m* ($x \geq 0.80$) [37].

1.2.2 $LaAlO_3/SrTiO_3$ Interface

For the perovskite oxides, due to the incredibly broad range of physical properties and the lattice-matched crystal structures within a few percent, an interesting question related to the interface can be raised. If an interface between two different complex oxides can be fabricated with atomic-scale precision, what properties will be present at this interface? Specifically, would it be just a simple mixture of two bulks' properties or will some novel properties manifest?

In 2004, A. Ohtomo *et al*. demonstrated one example of such interfaces, $LaAlO_3/SrTiO_3$ (LAO/STO), prepared with atomic-scale precision [9]. Specifically, two different types of interfaces are expected in this LAO/STO system: the AlO_2-LaO/TiO_2-SrO interface (Fig. 1.2a) that was found to be conducting and the LaO-AlO_2/SrO-TiO_2 interface (Fig. 1.2b) that was found to be insulating. The unexpected high mobility 2DEG at the interface between these two insulators indicates the possibility of unexpected properties at such interfaces. As there are already rich properties observed in individual complex oxides, novel properties at

this oxide interface suggest that a more colorful spectrum is waiting to be discovered. Hence, the result quickly attracted intensive research activities.

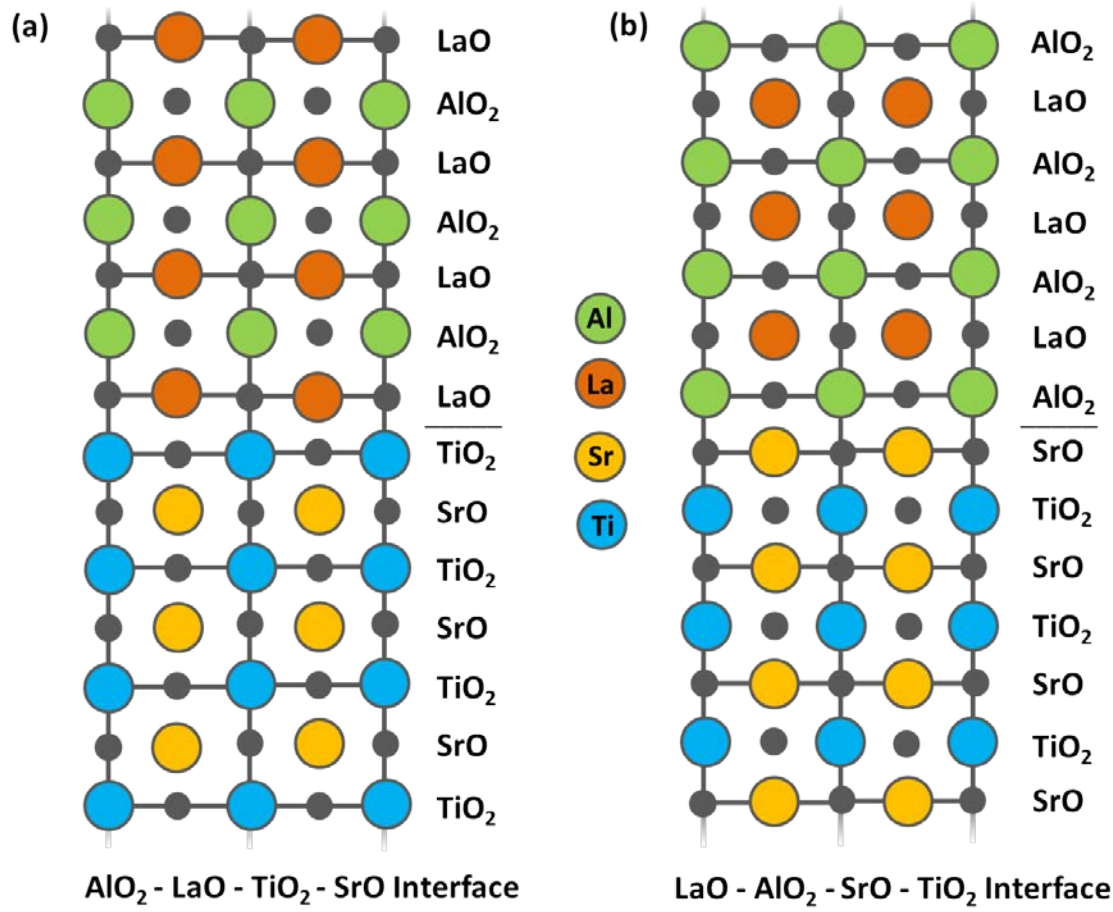

Figure 1. 2: *Schematic representation of the two types of LAO/STO interfaces. (a) Conducting AlO_2-LaO-TiO_2-SrO interface; (b) Insulating LaO-AlO_2-SrO-TiO_2 interface.*

1.2.3 Other Atomically Flat Interfaces and Heterostructures

Besides the LAO/STO interface, other atomically flat interfaces and heterostructures are also very intriguing. The 2DEG was also observed at LTO/STO interface [8], and also orbital reconstructions at the interface between (Y,Ca)$Ba_2Cu_3O_7$ and $La_{0.67}Ca_{0.33}MnO_3$ [38], colossal ionic conductivity at interfaces of epitaxial ZrO_2:Y_2O_3/STO [39], superconducting

temperature enhancement at the interface between La_2CuO_4 and $La_{1.55}Sr_{0.45}CuO_4$ [40], and dielectric constant enhancement at ultrathin $PbTiO_3$ [41], are some examples of different intriguing properties observed at complex oxide interfaces which further enrich the material function spectrum of oxides significantly.

1.3 The Possible Origins of the Two-Dimensional Electron Gas at Oxide Interfaces

The observed phenomena at LAO/STO interfaces are interesting and so are the underlying mechanisms. Researchers have studied both experimentally and theoretically the possible mechanisms. Nakagawa *et al.* proposed a currently commonly believed mechanism – the polarization catastrophe – to explain the 2DEG based on the polarization discontinuity at the interface [42]. Besides the polarization catastrophe, oxygen vacancies [43], intermixing and strain [44] also contribute to the conductivity at the interface.

1.3.1 Polarization Catastrophe

To understand the polarization catastrophe model, the explanation starts from the polarization of LAO and STO. LAO is a polar material stacked by positively charged sublayers $(LaO)^+$ and negatively charged sublayers $(AlO_2)^-$. In contrast, STO is a non-polar material stacked by the neutral sublayers $(SrO)^0$ and $(TiO_2)^0$. Consequently, a polarization discontinuity [42] occurs at both the AlO_2-LaO/TiO_2-SrO interface and LaO-AlO_2/SrO-TiO_2 interface.

According to the polarization catastrophe model illustrated in Fig. 1.3, the (001) planes of LAO have alternating net charges (ρ) which lead to an increasing potential as the LAO thickness increases. The catastrophe of this diverging potential could generally be avoided

by atomic disordering or stoichiometry change at traditional semiconductor interfaces. However due to the multivalence Ti states in STO, electronic transition becomes a preferable option and the atoms do not have to reconstruct [42]. Taking the AlO_2-LaO/TiO_2-SrO interface as an example (Fig. 1.3a and 1.3b), the internal electric field of the LAO layer induced by the charged sublayer injects 0.5 electrons per LAO uc into the interface and the injected electrons form an n-type conducting interface. On the contrary, LaO-AlO_2/SrO-TiO_2 interface shown in Fig. 1.3c and 1.3d will be a p-type insulating interface by accepting 0.5 holes per LAO uc. Because Sr has only a single valence, a $SrO_{0.75}$ layer is expected and the atomic reconstruction results in an insulating interface. Experimentally, this mechanism was also strongly supported by a critical thickness of LAO observed by J. Mannhart *et al*. [10]. They observed that the 2DEG only occurs when the thickness of the grown LAO film is larger than 3 uc when the built in potential (0.9 eV/uc) exceeds the STO bandgap of 3.2 eV.

So only the n-type LAO/STO interface is conducting and interesting. In this thesis, LAO/STO interface only indicates the n-type LAO/STO interface.

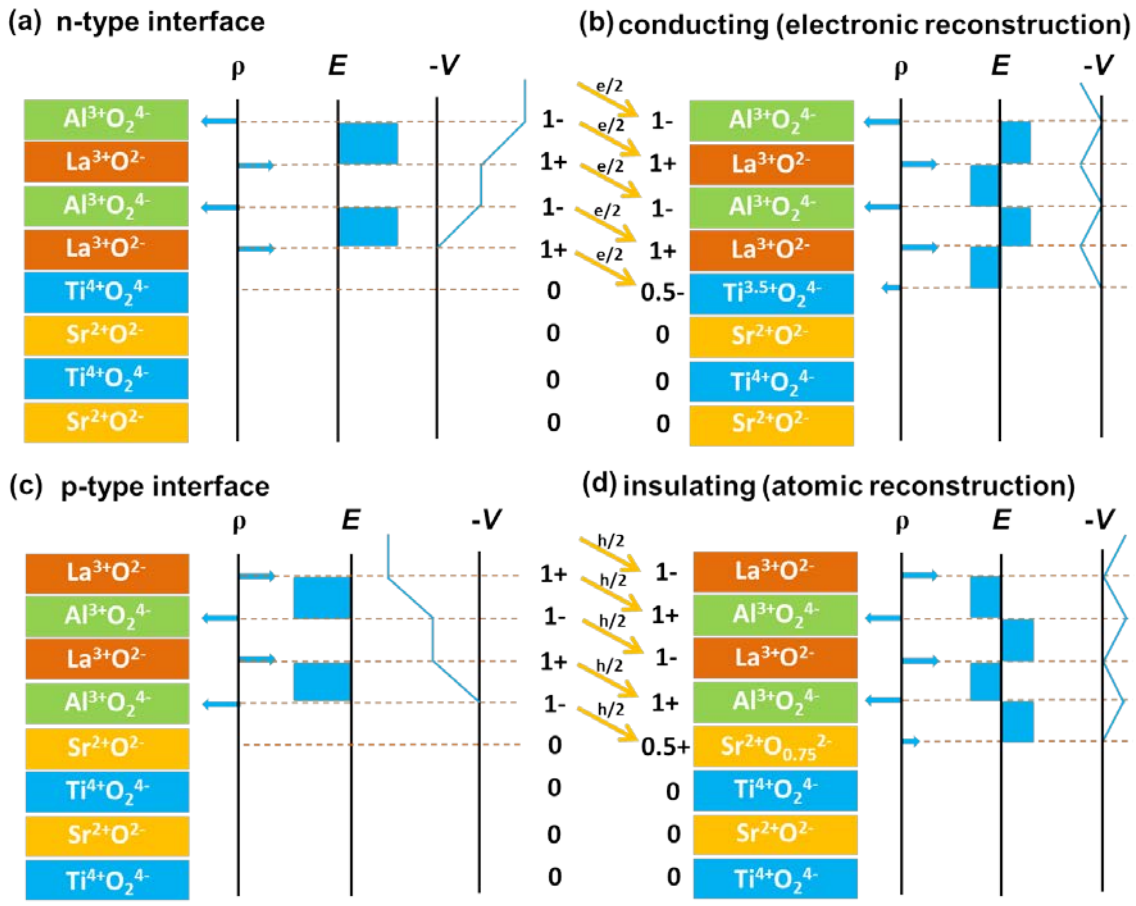

Figure 1. 3: *Polarization catastrophe illustrated for atomically abrupt interfaces between LAO and STO along (001) axis. (a) n-type interface before reconstruction; (b) n-type interface after reconstruction; (c) p-type interface before reconstruction; (d) p-type interface after reconstruction.*

1.3.2 Effects from Oxygen Vacancies and Intermixing

The actual mechanism behind the conducting interface is more complicated, because oxygen vacancies and intermixing also could occur during the fabrication process.

The LAO/STO interface can be prepared by depositing LAO on the STO substrate in a wide range of oxygen partial pressures (P_{O2}). Depending on the P_{O2}, the samples fall under two classes, the ones grown at low P_{O2} ($\leq 10^{-5}$ mbar) and the ones grown at high P_{O2} ($\geq 10^{-4}$

mbar). The sheet resistances of the samples grown at $P_{O2} \leq 10^{-5}$ mbar (low pressure samples) are ~10 Ω/□ at 300 K and ~1 mΩ/□ at 5 K with an almost temperature-independent carrier density n of ~10^{17} cm^{-2} and an increase of Hall mobility μ to ~10^{4} $cm^{2}V^{-1}s^{-1}$ at 5 K [9–13], [43]. The large n of the samples grown in this pressure range indicates a 3D conductivity that is most likely dominated by oxygen vacancies [43]. The sheet resistances of samples grown at $P_{O2} \geq 10^{-4}$ mbar (high pressure samples) are 9–13 kΩ/□ at 300 K and gradually decrease to ~200 Ω/□ at 5 K; n is reduced by a factor of four from (0.8–1.0)×10^{14} cm^{-2} at 300 K to (2.0–2.5)×10^{13} cm^{-2} at 5 K, and the μ increases significantly to ~10^{3} $cm^{2}V^{-1}s^{-1}$ at 5 K.

Although for samples prepared with P_{O2} from 10^{-6} to 10^{-2} mbar, the carrier density varies from 10^{17} to 10^{13} cm^{-2} at 2 K and 10^{17} to 10^{14} cm^{-2} at 300 K respectively [45], only 0.5 electrons per LAO uc is expected at the n-type interface based on the polarization catastrophe model, which corresponds to a n of 3.2×10^{14} cm^{-2}. Obviously, the n for samples grown at low P_{O2} is larger than the expected n. By doing a thermal annealing experiment, it was found that the dominating carriers at LAO/STO interfaces prepared under 10^{-5} mbar of P_{O2} are generated by enormous amount of oxygen vacancies in STO substrate [43]. However, according to the same study, it is impossible to get conductivity in STO by annealing in P_{O2} greater than 10^{-4} mbar. Therefore, the electron gas in LAO/STO prepared in P_{O2} above 10^{-4} mbar cannot be due to oxygen vacancies and it is most probably caused by charge injection due to the polarization catastrophe.

Because there is the negligible amount of oxygen defects in high P_{O2} samples, the high P_{O2} samples are considered as 2D interface sample or 2DEG samples. And the low P_{O2} samples are considered as 3D interface sample.

Intermixing could also be an issue, because doping STO by La could introduce conductivity as well. This model can be simply considered as several uc conducting $La_{1-x}Sr_xTiO_3$ formed by atomic intermixing at the n-type LAO/STO interfaces [46, 47]. However, this model could not explain the insulating behavior at p-type LAO/STO interfaces. Furthermore, in the La doped STO experiments, it was found that ultrathin La doped STO films with a thickness below 6 uc grown on STO substrate are insulating. This result also directly disproves that the possible origin of 2DEG is from intermixing and we will discuss this in details in this thesis.

Overall, polarization catastrophe induced by polarization discontinuity at the LAO/STO interface is the most possible mechanism.

1.4 Emergent Properties at Oxide Interfaces

The 2DEG is not the only unexpected phenomenon happening at the LAO/STO interface. After intensive studies, many other novel properties were also observed at this interface. In this section some unexpected properties will be discussed.

Comparing LAO/STO interfaces prepared under different P_{O2}, the LAO/STO interface exhibits bulk conductivity for films grown in pressures below 10^{-4} mbar [43], two dimensional superconductivity with a transition temperature of ~200 mK for pressures of 10^{-4} mbar [48], and magnetism for pressures above 10^{-3} mbar [11, 45]. As closely related to the research in this thesis, I want to emphasize the observation of the weak magnetism by Brinkman *et al.* [11], who summarized the relation between observed properties and P_{O2} at

the LAO/STO interface and for the first time demonstrated the magnetic property at this nonmagnetic-material-based interface. In the year of 2011, four different groups [49–51] further demonstrated the coexistence of superconductivity and ferromagnetism at the LAO/STO interfaces using different techniques, such as Superconducting Quantum Interference Devices (SQUID), MR study, torque study and scanning SQUID microscopy. Under external electrical field, the interface exhibits quantum phenomena as well: by applying a back gate, the electrical field, quantum critical point [12] and tunable Rashba effect [52] were demonstrated.

Various investigations for technical applications were also performed and they made significant contributions to push complex heterostructures into applications. On integrating complex oxide 2DEG with conventional semiconductor industry, C. B. Eom and coworkers demonstrated the 2DEG of LAO/STO by growing the oxides on Si [53]. This proved the possibility to combine LAO/STO with commercialized Si based devices. Mannhart's group developed a technique to pattern the buried interface into different devices [54]. Furthermore, new techniques and new structures were also developed to make use of novel and rich properties of complex oxides and interfaces. J. Levy *et al*. employed atomic force microscopy (AFM) to structure fine patterns on 2DEG interfaces [13] and they used this technique to fabricate a single-electron field-effect-transistor [55].

1.5 Dark Clouds in the Sky

Although a lot of significant results have already been achieved at the complex oxide interfaces and heterostructures, there are still unresolved issues [15, 16]. In particular, the gaps related to this thesis research are briefly listed:

1. The underlying mechanism for 2DEG at LAO/STO interfaces requires further clarification. Even though the polarization catastrophe model is able to explain most of the phenomena, there is still no experimental evidence showing the existence of the internal electrical field in LAO. In addition, effects from oxygen vacancy, strain and intermixing needs to be studied in detail and quantified.

2. The reason why low dimensional oxide materials and heterostructures behave very differently from their bulk is still not fully understood. As commonly believed, new properties and new physics emerge when material dimensionality is changed. Therefore, an investigation of properties changes before and after dimensional crossover is critical.

3. Exploring new properties by varying fabrication conditions in existing systems is interesting because new and unexpected properties may emerge, and this can help our understanding of the responsible mechanism. For example, there have been a lot of reports on properties of LAO/STO grown in pressures up to 10^{-3} mbar. However, there has been very little study on the interface properties with growth pressures higher than 10^{-3} mbar. Hence when we prepared these interfaces at a pressure of 10^{-2} mbar we were surprised by the observation of electronic phase separation at these interfaces.

4. A system with $Ti^{3.5+}$ similar to the LAO/STO interface can be achieved by doping STO with 50% La. It will be interesting to study this LSTO as a comparison to the LAO/STO interface. Properties such as critical thickness and field effect of both systems can help our understanding of LAO/STO interfaces and facilitate exploration of new interfaces.

1.6 Outline

The main purpose of the research in this thesis was to explore new properties and investigate the underlying mechanisms for the 2DEG at LAO/STO interfaces. All relevant contents are divided into chapters and listed as follows.

In chapter 2 a variety of fabrication and analysis techniques are introduced. These techniques include the functions of substrate surface preparation, film fabrication, structural characterization, transport property measurement, magnetic property measurement and optical property measurement.

In chapter 3 static and dynamic optical properties on oxygen defects in LAO/STO heterostructures prepared at low P_{O2} are investigated using Ultraviolet-Visible-Near infrared (UV-Vis-NIR) spectrometry and femtosecond pump-probe technique. The defect behaviors under the influence of the LAO polarization catastrophe model are discussed.

In chapter 4 MR differences are presented in comparison with high P_{O2} 2D conducting and low P_{O2} 3D conducting LAO/STO interfaces. In these samples, there are at least three difference related scattering processes: magnetic, phonon and interface scattering. In addition, it is found that MR is able to serve as an indicator of the conducting channel dimensionality at LAO/STO interfaces.

In chapter 5 the growth pressure P_{O2} for LAO/STO interfaces was pushed up to an unexplored regime (above 10^{-2} mbar). Interestingly, novel magnetic properties called electronic phase separation were observed and this is the first experimental evidence for the coexistence of different electronic and magnetic phases.

In chapter 6 LSTO films, which is a system with $Ti^{3.5+}$ similar to LAO/STO interfaces, are fabricated on STO substrates with different film thicknesses and a coexistence of two types of electrons are observed in this system. Investigation by varying temperature, film thickness and back gate electric field revealed the properties of these electrons. Furthermore, an abrupt metal-to-insulator transition in LSTO is observed, by reducing the LSTO film thickness to below 6 uc. In order to understand the origin of this transition, various experiments were conducted, such as strain effect by using different substrates with lattice constants and scanning tunneling microscopy measurement.

Chapter 7 summarizes the studies in this thesis and also suggestions for possible experiments.

Chapter 2 Sample Preparation and Measurement Techniques

2.1 Atomic Control of Substrate Surface

Atomically flat substrates are required to create the atomically aligned heterostructures or interfaces. STO is the most commonly used substrate mainly because of our ability to prepare a single terminated surface in addition to its interesting physical and chemical properties as discussed in Chapter 1. To achieve a TiO_2 surface termination on STO substrates (CrysTec GmbH), they were first treated with buffer hydrofluoric acid (BHF) with NH_4:HF = 87.5:12.5 and pH = 5.5 for 30 seconds, two times of short immersions in deionized water and then subsequently annealed at 950 °C for 1.5 hours in air with 5 °C per min ramping up rate and 3 °C per min ramping down rate [56, 57]. A similar thermal treatment can also be applied to other substrates such as LAO (a = 3.791 Å), $DyScO_3$ (110)(a = 3.944 Å), $NdGaO_3$ (110) (NGO) (a = 3.859 Å) and $(LaAlO_3)_{0.3}(Sr_2AlTaO_6)_{0.7}$ (001) (LSAT) (a = 3.868 Å) to obtain atomically flat surfaces [44].

Substrate morphology is generally characterized by AFM (Agilent 5500) [58]. The basic features of an AFM consist of tip, laser and detector. During the scanning, the tip movement is amplified by a laser with the beam deflection measured by a photo detector. As AFM is able to probe a variety of interactions by using different types of tips, information of morphology, magnetic domain, friction, charge polarization can be obtained. In Fig. 2.1, a typical atomically flat surface of STO is demonstrated by AFM with step flow structure (Fig. 2.1a) and one-unit-cell-high (3.905 Å) step height (Fig. 2b).

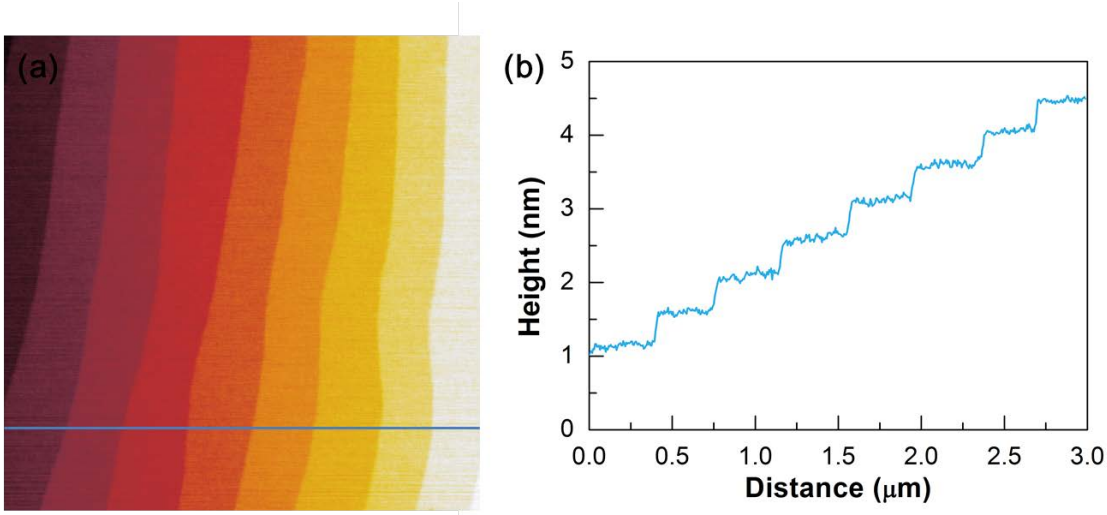

Figure 2. 1: *(a) A 3 micrometers by 3 micrometesr AFM monograph image of TiO_2 terminated STO substrate after treatment which shows clear (b) terraces with 1 uc step height profile.*

2.2 Film and Heterostructure Fabrication with *in-situ* RHEED

Pulsed laser deposition (PLD) with an *in-situ* high pressure reflection high energy electron diffraction (RHEED) (Fig. 2.2a and Fig. 2.2b) is the growth technique used to prepare atomically flat heterostructures and interfaces [59]. In a PLD with *in-situ* RHEED setup shown in Fig. 2.2a, there are three basic components all placed in a high vacuum environment, namely targets, substrates and RHEED.

The targets are mounted on a carousel which can be rotated to select different targets. These PLD targets are prepared by using high purity powders. The powders are carefully weighed, mixed and ground for several hours before being sintered at high temperatures. Then, the sintered mixed powder is pressed into pellets and again calcinated above 1000 °C for typically 24 hours. Before deposition, the PLD chamber pressure is tuned from a base pressure below 10^{-8} mbar to a desired P_{O2} which is kept constant during the deposition. The substrate is mounted exactly in front of the target holder. During the deposition, the

substrates are heated to a desired temperature by using a thermal radiation heater. The Lambda Physik KrF excimer laser with wavelength of 248 nm and pulse width of approximately 15 ns is used for ablating targets. Due to the high power of laser, a plasma of target material can be generated by non-equilibrium laser heating and the evaporated materials is transferred onto the substrate. The laser pulse frequency is typically maintained at 1 Hz for all of the depositions to ensure a slow enough deposition.

Depending on the free energies of the substrate surface, film surface, and film-substrate interface, there are generally four different growth modes in the film fabrication process, namely Frank-Van der Merwe growth, Volmer-Weber growth, Stranski-Krastanov growth and step flow growth [60]. Wetting will dominate if free energy of substrate is higher than the total of that of thin film and interface, and this growth mode is called Frank-Van der Merwe growth [61]. However, if bonding between substrate and film is weak, 3D island growth would occur and coalesce, and this growth mode is called Volmer-Weber growth [62]. The intermediate case is when a strong substrate-film interaction initially leads to continuous layer growth but this is followed by discrete islands, and this growth mode is called Stranski-Krastanov growth [63]. The final mode is the important step flow growth if the diffusion on the terrace is very fast. In this growth mode, this prevents the adsorbed particles from forming nucleated sites or islands, and they will quickly move to the step edges of the terraces to form a layer-by-layer growth.

The layer-by-layer growth mode can be monitored by *in-situ* RHEED. RHEED is a characterization technique, but is included in the film fabrication as it is used *in-situ* during the film deposition to ensure the presence of layer-by-layer growth. It basically consists of an electron gun, a phosphor florescent screen and a processor. Despite the high energy of the

electrons, it is also surface sensitive as it goes by a glancing angle, sensing only the top few atomic layers of the surface. Sensing depth is small, allowing the surface properties to be measured. During the characterization, an electron beam is incident from RHEED gun with a glancing angle (3-5 degrees) onto the substrate. The reflected and diffracted beams are collected by a high quality florescent screen. In the Fig. 2.2b, a typical RHEED pattern for STO (001) is presented. The main spot, the specular spot (circled white spot shown in Fig. 2.2b), is from the reflected electron beam and its intensity provides information of the film growth. Intensity of the specular spot is the parameter monitored by the florescent screen. The intensity of the reflected beam is roughly proportional to the surface flatness. In simple terms, smooth surfaces give high reflected intensities while rough surfaces give low reflected intensities. With this, one oscillation in the RHEED intensity graph would represents one unit cell of the film grown. Figure 2.2c shows typical RHEED intensity oscillations for 26 uc of LAO grown on STO substrate at 10^{-6} mbar P_{O2}. Although RHEED uses electron gun as the source, it can still be used at high pressure even up to 0.1 mbar P_{O2} pressure by using a double pumping system which is able to maintain the high vacuum environment at the electron gun, preventing filament oxidation [64].

The usage of PLD with *in-situ* RHEED allows the complex oxides to be prepared and be reproduced on the atomic level. This is of most importance as the control of growth thickness to the atomic level affects the properties exhibited by the film, and would give us an insight in to the growth dynamics of the oxide interface systems.

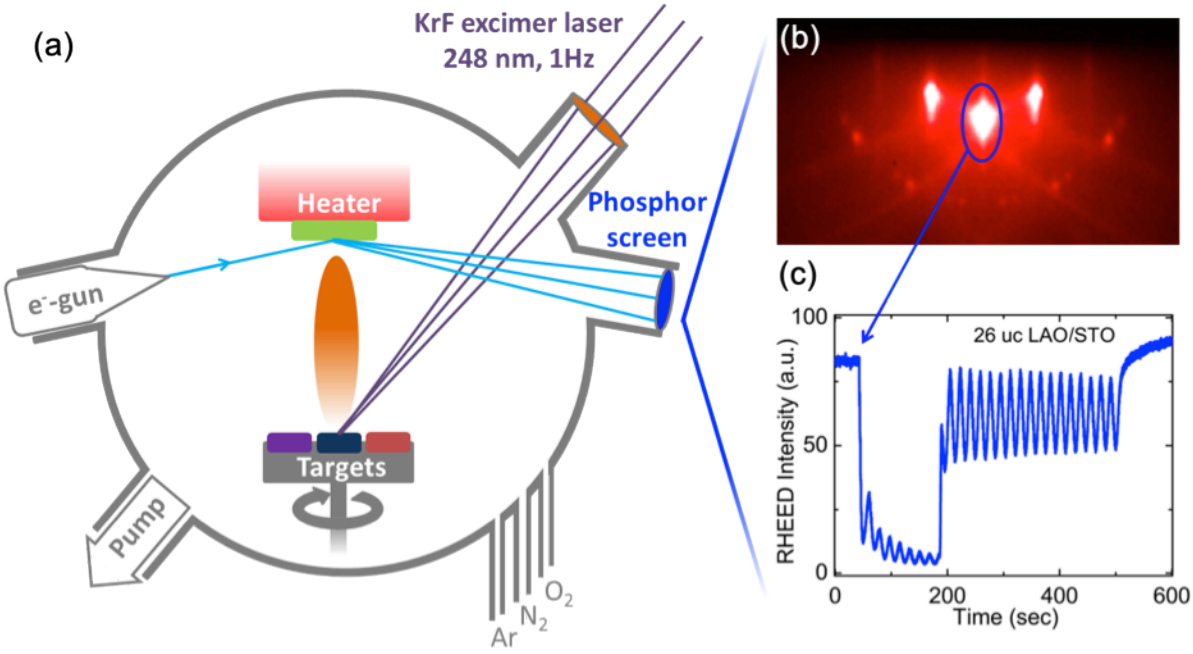

Figure 2. 2: *(a) Schematic diagram of a PLD system with in-situ RHEED. (b) RHEED pattern consists of a combination of diffracted and reflected electron beam and RHEED oscillation (c) where each oscillation corresponds to one unit cell.*

2.3 Structural Property Characterization

After sample fabrication, X-ray diffraction (XRD) is one of the most common techniques used to characterize the material structure, because X-ray can be diffracted by a crystalline material comprises of ordered atom planes. In this thesis, Bruker D8 Discover is the XRD model used. During the measurement, the X-Ray, from Cu-Kα source operated at 40 kV and 40 mA, is diffracted by the sample. A 2D detector of VÅNTEC-2000 is used to collect the diffracted beam which contains the information of the film structure and quality. The formula used in XRD to describe diffraction is the Bragg equation:

$$2d\sin\theta = n\lambda \qquad \textbf{Equation 2-1}$$

where d is the spacing between the crystal planes, theta (θ) is the X-ray incident angle, λ is the wavelength of the X-rays, n is the order of diffraction and = 1,2,3.... As there are a

number of series of atom planes in a crystalline material, the resultant diffraction will consist of several peaks at the corresponding theta values. This not only gives information regarding the crystal structure of the material analyzed, it also enables the composition of the material to be determined.

XRD can also be used to structurally characterize superlattices. Figure 2.3 shows an XRD pattern (counts versus 2theta) on a $[(LAO)_{10}/(STO)_{10}]_8$ superlattice (the sample has 8 times of the superlattice period which consists of 10 uc LAO and 10 uc STO) facilitated by our PLD system. The characteristic lengths in superlattices are modulation length ($\Lambda=t_{LAO}+t_{STO}$), or superlattice period, which is a sum of lengths of these two materials. The satellite peaks besides the (00l) STO substrate peaks in the theta-2theta diffraction profile are caused by the modulation length and is an indication of superlattice quality. The modulation length can be determined by the following equation [65]:

$$\Lambda = \lambda / [2|sin\Theta_{n\pm1} - sin\Theta_n|] \qquad \textbf{Equation 2-2}$$

where λ is the wavelength of the X-ray and Θ_n the theta angle of the n^{th} order satellite peak. In the resulting fitting, modulation length Λ is around ~4 nm. The fitted value agrees well with the expected modulation lengths by using the bulk values for LAO (3.791 Å) and STO (3.905 Å). The figures in the insert are raw image obtained by VÅNTEC-2000 2D detector.

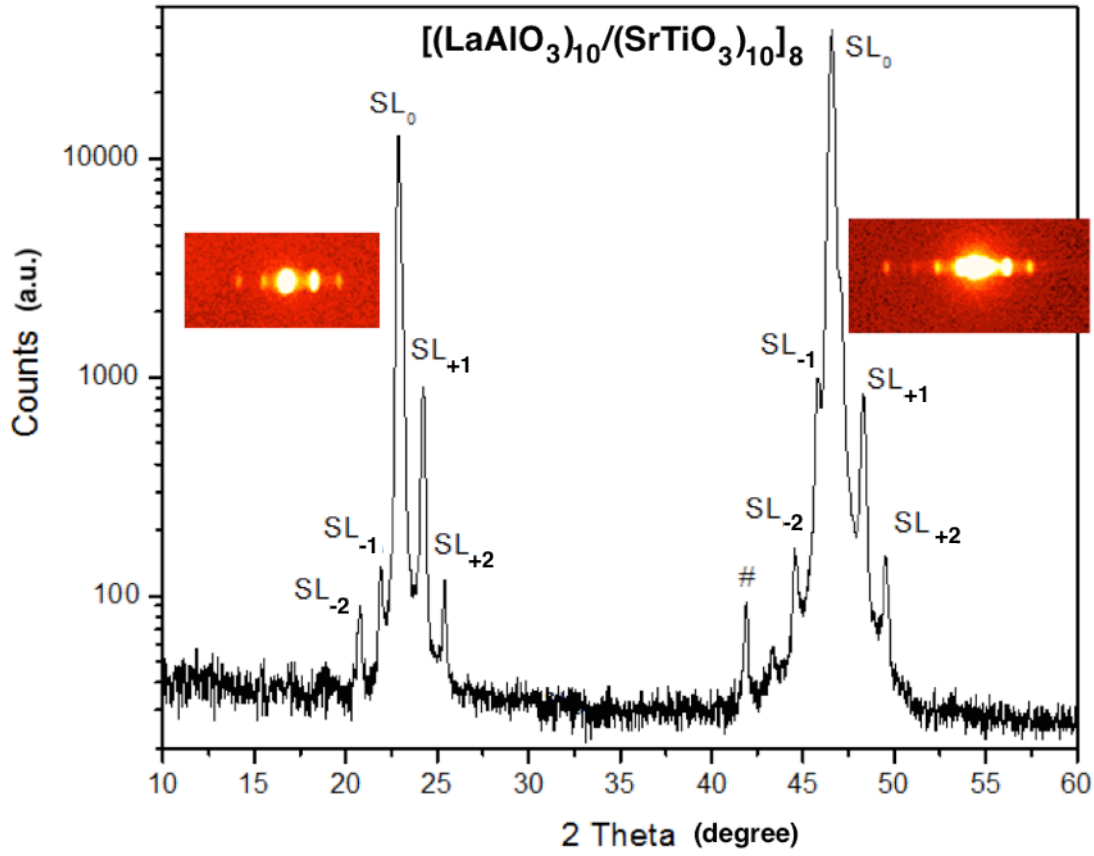

Figure 2. 3: *A theta-2theta diffraction profile for a $[(LAO)_{10}/(STO)_{10}]_8$ superlattice sample with clear satellite peaks. Inserted figures are raw images captured by the 2D detector.*

2.4 Electrical Measurement

A variety of electrical property characterizations can be conducted by employing the Physical Property Measurement System (PPMS, Quantum Design Inc.). There are generally three types of measurements for electrical property characterization: resistance (R) versus Temperature (T) ($R(T)$), MR and Hall resistance (HR). During these measurements, sample environment is varied including the magnetic fields variation up to (zero to ± 9 T) and the temperature variation (1.9 K to 400 K).

Resistance measurements are normally made in van der Pauw geometry [66, 67] (Fig. 2.4a) or linear geometry (Fig. 2.4b) on square shaped samples (5 x 5 mm^2). Ohmic contacts are created by ultrasonically bonded Al wire on the sample corners (West Bond Wire Bonder, power from 350W to 400W and time around 30 ms). For the van der Pauw geometry in Fig. 2.4a, if defining $R_1=V_1/I_1$ and $R_2=V_2/I_2$, the actual sheet resistance R_S can be obtained by the following van der Pauw formula:

$$exp(-\pi R_1/R_S) + exp(-\pi R_1/R_S)=1. \qquad \textbf{Equation 2-3}$$

For the linear geometry in Fig. 2.4b, the actual resistivity ρ can be obtained by applying the formula:

$$\rho = RA/l \qquad \textbf{Equation 2-4}$$

where R is the resistance, A is the area and l is the length.

By varying the magnetic field B between ± 9 T and bonding sample in Hall geometry, the HR measurement (Fig. 2.4c) can also be done. For a typical and simple one-band system, carrier density n and Hall mobility μ can be determined by the formulas:

$$n = IB/qV_H \qquad \textbf{Equation 2-5}$$

$$\mu = 1/qnR \qquad \textbf{Equation 2-6}$$

where I is the current applied, q is the elementary charge (1.602×10^{-19} coulombs) and V_H is the Hall voltage. To be noted that the n is in fact sheet carrier density in this thesis because no thickness normalization was done due to the 2D feature of the samples.

Field effect measurements in combination with the previous measurements are performed. With gate electrodes fabricated at the bottom sides of samples, three used connection geometries are shown in Fig. 2.4c. In this thesis, there are two types of samples, namely conducting film and conducting interface. For the conducting film with known conducting path thickness, these geometries can be used to measure carrier mobility and bulk carrier

density by applying the above equations. For the conducting interface with insulating film and insulating substrates, the measured carrier density and mobility has to be attributed to the conducting interface. However, because the conducting path thickness is unknown, the measured carrier density is in fact only sheet carrier density. That means for the conducting interface with unknown conducting path thickness, the carrier mobility and sheet carrier density can be achieved by applying the above equations.

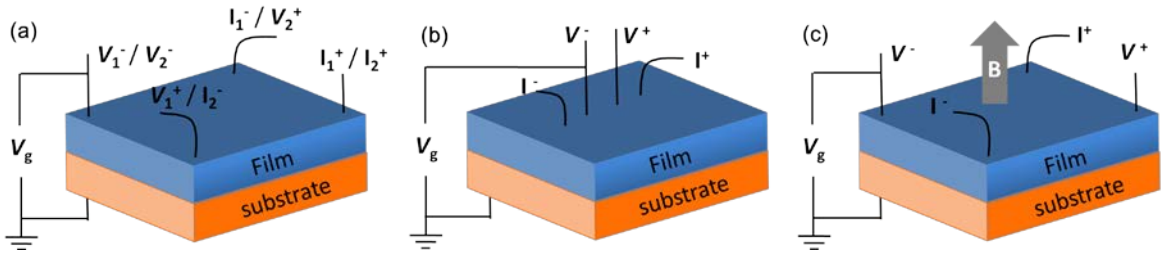

Figure 2. 4: *Diagram for back gate experiment for measuring resistance in (a) van der Pauw geometry and (b) linear geometry and (c) HR measurement.*

2.5 Magnetic Measurement

Based on superconducting loops containing Josephson junctions, the Quantum Design Magnetic Property Measurement System (MPMS) is a family of analytical instruments configured to study the subtle magnetic properties of small experimental samples over a broad range of temperatures and magnetic fields. In my study, MPMS SQUID VSM from Quantum Design Inc. is the system used [68]. In our MPMS system, Vibrating Sample Magnetometers (VSMs) were utilized to optimize speed and sensitivity. Specifically, the sample is vibrated at a known frequency and phase-sensitive detection is employed for rapid data collection and for reducing noises. Unlike traditional (non-superconducting) VSMs, the size of the signal produced by a sample is not dependent on the frequency of vibration, but

only on the magnetic moment of the sample, the vibration amplitude and the design of the SQUID detection circuit.

Generally three types of measurements can be done by MPMS SQUID VSM: moment versus field (M(H)) to characterize the magnetization changes under the influence of magnetic field, moment versus temperature (M(T)) to characterize the magnetization changes under the influence of thermal energy and moment versus time (M(t)) to characterize the magnetization relaxation. During the measurement, the MPMS SQUID VSM utilizes a superconducting Niobium-Titanium (NbTi) magnet (a solenoid of superconducting wire) to subject samples to magnetic fields up to 7 Tesla and uses liquid Helium and the Helium vapor and a sample heater to tune the sample temperature from 400 down to 1.8 K.

Although a lot of advantages exist in the MPMS SQUID VSM, there is also possible signal generated from artifacts during the measurement. In order to acquire reliable data, sample holder effects, loosely mounted samples and environmental sources of noise need to be controlled carefully.

Quantum Design Inc. supplies quartz and brass sample holder for mounting samples. The quartz holders are brittle and fragile, but have a smaller magnetic signal/background. For samples having a large moment, the brass sample holders have negligible magnetic background and may be easier to handle.

Mounting samples firmly to a sample holder is required to achieve accurate magnetic moment readings because the holder will undergo vibration at 14 Hz. In our experiment,

(GE) 7031 varnish is used which can withstand the temperature extremes and sample holder thermal contraction during the experiment. After measurement, (GE) 7031 vanish can be dissolved with alcohol or toluene to remove the sample from the sample holder.

In order to quickly and precisely isolate the sample signal from other noise sources including drifting SQUID signal and mechanical noise sources synchronized to the sample vibration, the lock-in amplification of the SQUID signal is performed. The SQUID VSM measurement technique vibrates the sample at about the very center of the detection coils and generates a SQUID signal by multiplying the measured signal with a phase-corrected reference signal at a certain frequency and then extracting the DC component of the result. Therefore, reliable SQUID signal can be achieved with minimum external noise interference.

2.6 Optical Property Measurement

Transmittance spectrum is measured by Shimadzu SolidSpec-3700 UV-Vis-NIR spectrophotometer. The principle of transmission measurement in the UV-Vis-NIR spectrophotometer is very simple as shown in Fig. 2.5. In transmission measurement, the light is generated by the lamp in a range from 240 nm to 2600 nm with the wavelength accuracy of ± 0.2 nm in both UV and Vis regimes, and ± 0.8 nm in NIR regime. The light is then split into two beams. One of them serves as a reference which is passed through a reference sample or air and detected by a photodetector. The other one passes through the real sample and is detected by the other photodetector. For the detection, the photomultiplier tubes are used to detect UV and Vis light, and the InGaAs together with PbS are used for NIR detection. At last, the transmittance can be obtained by comparing the detected signal after real sample to the detected signal after the reference sample.

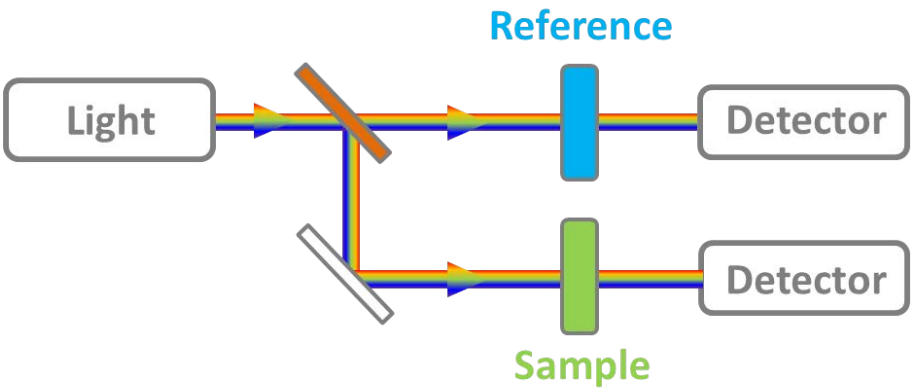

Figure 2. 5: *A diagram for transmission measurement in a spectrophotometer.*

2.7 Ultrafast Optical Property Measurement

Femtosecond (fs) pump-probe technique is an optical technique to detect a system's dynamic optical properties because the thermal fluctuation is negligible in this ultrafast process [69]. Using this technique, two types of different measurements can be performed, namely single wavelength pump-probe and transient absorption. In single wavelength pump-probe measurements, the normalized transmission change ($\Delta T/T$) of the probe beam was detected at a single wavelength at varying delay times after excitation of the system by the pump beam. Depending on the system features, this $\Delta T/T$ relaxation curve can be fitted by exponential curves from different relaxation models. In the transient absorption measurement, the transient changes of the spectra of the sample at a fixed delay time and their temporal evolution were monitored also after excitation of the system by pump beam.

The pump-probe setup employed in our study is illustrated in the Fig. 2.6. The 1 kHz 800 nm laser pulses with horizontal polarization, a pulse width of 100 fs and an energy of 2 mJ are generated from a mode-locked Ti:sapphire oscillator seeded regenerative amplifier laser

system (Spectra Physics). The pulse width is determined by autocorrection technique and the laser energy are controlled by normal density filter. The laser beam is then split into two portions with the same horizontal polarization. The larger portion of the beam is used as a pump beam whose wavelength can be possibly tuned to 400 nm by mounting a β-barium borate (BBO) material. A small portion of the pulses is used to generate white light continuum (WLC) in a sapphire plate. The white light beam was split into two portions: one as probe and the other as a reference to correct pulse-to-pulse intensity fluctuations. To minimize the probe influence, the ratio of the pump pulse energy to the probe pulse energy is tuned to be above 20. The signal and reference beams are detected by photodiodes that are connected to lock-in amplifiers and the computer. The lock-in amplifier frequency control is realized by a chopper with frequency of 500 Hz. The pump beam is focused onto the sample with a beam size of 300 μm and overlaps with the smaller-diameter (200 μm) probe beam. The delay between the pump and probe pulses was varied by using a computer-controlled translation stage. In a pump-probe scan the value of the normalized transmission change ($\Delta T/T$) is determined as a function of the delay time between the pump and probe pulses. Overall, the temporal resolution of the pump-probe experiment is 0.1 ps and the percentage of fluctuation for laser pulses used is smaller than 0.1%.

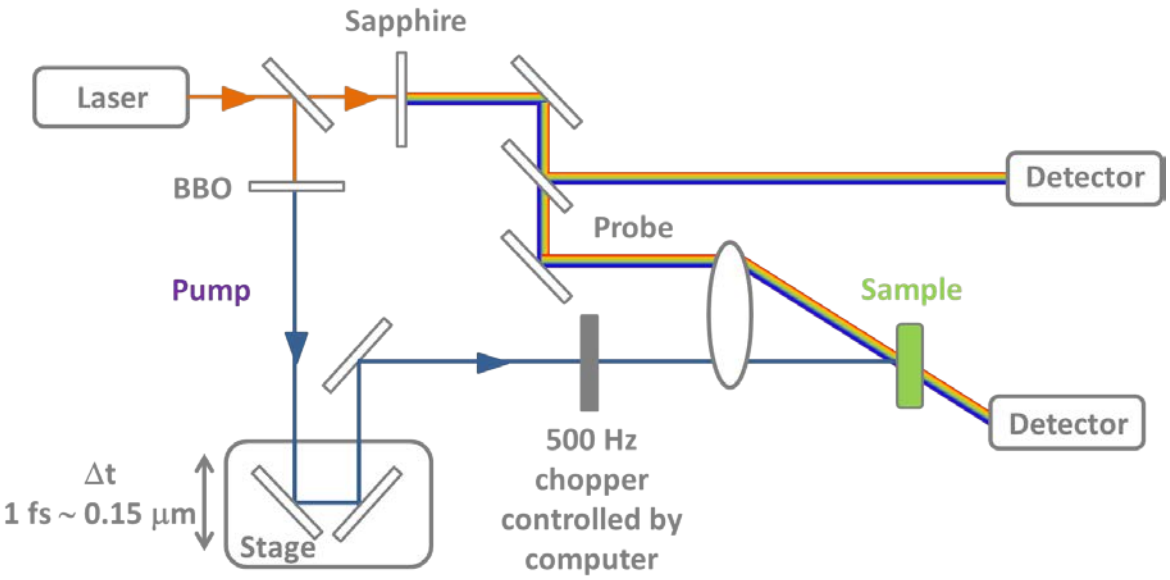

Figure 2. 6: *Pump-probe experimental setup employed in our study.*

Chapter 3 Static and Ultrafast Dynamics of Defects of $SrTiO_3$ in $LaAlO_3/SrTiO_3$ Heterostructures

3.1 Introduction

The observation of the 2DEG at the LAO/STO interface [9–12] has triggered intense research activity. A clear map of all the defect levels in LAO/STO heterostructures and their respective characteristics is critical for the use of these structures in opto-electronic device applications, such as oxide LEDs, FETs, solar cells and so on. As discussed in the introductory chapter, LAO/STO heterostructures prepared in the P_{O2} range above 10^{-4} mbar are interesting as they exhibit a 2DEG. At lower P_{O2}, the electron distribution becomes more three dimensional due to oxygen vacancies in the STO substrate [43]. However, the optical properties of LAO/STO heterostructures prepared at P_{O2} higher than 10^{-5} mbar show very few intra-band features. Therefore, our investigation is focused on heterostructures prepared in a low P_{O2} of 10^{-6} mbar (where oxygen defects are enhanced) from which one may obtain information about heterostructures fabricated in higher growth pressures by extrapolation.

Furthermore, as one of the most important complex oxide materials, STO has attracted significant research attentions over the last several decades. A number of favorable properties, such as the stable cubic perovskite structure at room temperature, small lattice mismatch with a variety of important oxides (*e.g.*, $YBa_2Cu_3O_7$), and atomically controlled flat surfaces, have enabled STO to be a promising material for future oxide electronics applications [20, 21, 41, 56, 57, 59, 70–73]. For the LAO/STO heterostructures prepared at low P_{O2}, it can be assumed that the optical properties of the sample consisting of a very thin LAO layer on a 0.5 mm thick STO substrate will be dominated by the substrate [74]. A picosecond (ps) pump-probe study of intra-band defect levels with a temporal resolution of

15 ps has previously been performed on STO [75]. In that study, electrons were excited from defect levels to the conduction band (CB) and the relaxation of the carriers was measured. It was found that the electrons decay from CB to a defect level centered at 714 nm with a 40 ps relaxation time. It was postulated that further decay from this defect level to another defect level occurs in a time scale longer than 500 ps. However, more detailed characteristics of the dynamic properties of these defect levels could be obtained by employing a higher resolution laser.

In this chapter, a study of static and dynamic transmittance property of the LAO/STO samples prepared in the P_{O2} of 10^{-6} mbar (low P_{O2}) were conducted by employing UV-Vis-NIR spectrometer and a 100 fs pump-probe technique. In addition, LAO/STO samples prepared in the P_{O2} of 10^{-4} mbar were also discussed.

3.2 Experimental Procedure

LAO/STO heterostructures were prepared by depositing LAO on STO (001) substrates with a TiO_2 terminated surface. Using PLD, 26 uc of LAO were deposited on STO at 850 °C in a P_{O2} of 10^{-4} and 10^{-6} mbar from a single-crystal LAO target. The laser energy density on the target was 1.8 J/cm^2 and the repetition rate was 1 Hz. During deposition, layer-by-layer growth was monitored by *in-situ* RHEED.

The transmittance spectrum of the heterostructures was measured using a Shimadzu UV-Vis-NIR spectrometer with a wavelength range from 240 to 2600 nm. The ultrafast dynamics was characterized by fs laser pump-probe technique. This technique enabled

probing the relaxation mechanism of charge carriers which are buried in the film of heterostructures.

3.3 Results and Discussion

3.3.1 Static of Defects in $SrTiO_3$

The transmittance spectrum of STO substrate and LAO/STO heterostructures prepared under different pressures are plotted in Fig. 3.1a, which shows an optical band gap of 3.22 eV (385 nm). The STO substrate (blue curve) and LAO/STO prepared under high P_{O2} pressure (orange curve) are transparent in both visible and near-infrared regions at room temperature. However, for the 26 uc LAO grown on STO substrate in 10^{-6} mbar (red curve), the transmittance spectrum drastically changes while the optical band gap remains the same.

Three absorption peaks and an infrared absorption continuum in the wavelength region above 1.2 μm were observed in the transmittance spectrum of LAO/STO heterostructures prepared under high P_{O2} (Fig. 3.1a). In Fig. 3.1b, the corresponding optical density (OD) of low P_{O2} LAO/STO which is defined as $OD(\lambda) = -\log_{10}[T(\lambda)]$ is plotted. In the formula, $T(\lambda)$ is the transmittance at wavelength λ, normalized by the transmittance of the STO substrate which can take reflectivity of the two surfaces into account. In the region above 1.2 μm, the OD varies with wavelength λ in term of λ^n. This λ^n relation is Drude's law which describes the free carrier absorption in the infrared region and the fitting parameter *n* is found to be 2.61 in this case [23]. Therefore as seen in Fig. 3.1a, the free carrier absorption and absorption peaks are clearly observable only in the low P_{O2} LAO/STO heterostructures. In order to conveniently discuss defects, all mentioned defects mentioned in the following chapters are obtained about low P_{O2} LAO/STO heterostructures.

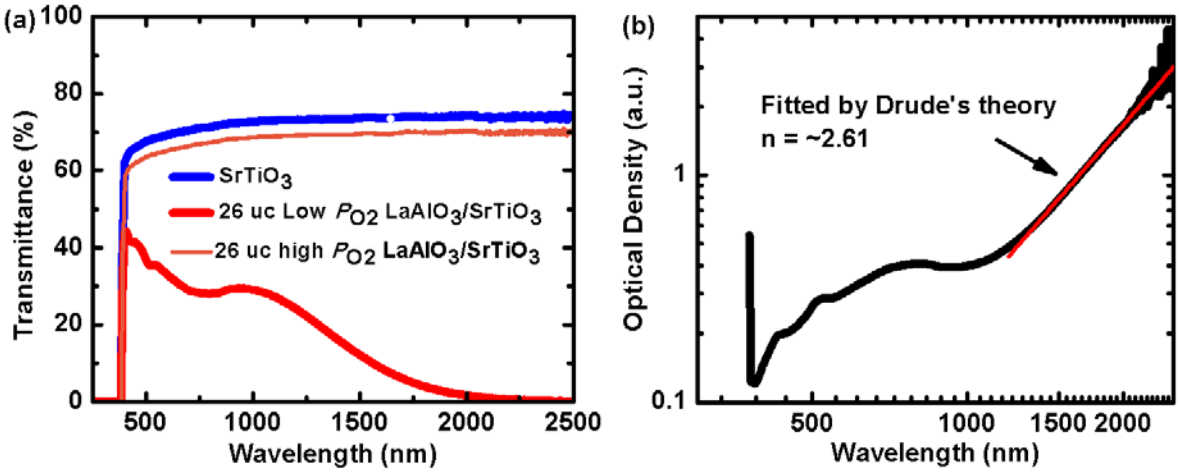

Figure 3. 1: *UV-Vis-NIR transmittance spectra. (a) UV-Vis-NIR transmittance spectra for STO (blue curve), high Po_2 LAO/STO heterostructures (orange) and low P_{O2} LAO/STO heterostructures (red curve). Three absorption peaks and a continuous absorption can be seen for low P_{O2} LAO/STO heterostructures. (b) OD of low P_{O2} LAO/STO heterostructures plotted in double log scale. A Drude fit is shown as a red straight line with fitted power n of ~2.61.*

After subtracting the free carrier absorption, three absorption peaks representing different type of defects are clearly visible as shown in Fig. 3.2a. This subtracted OD was fitted by three Lorentzian functions and the corresponding fitting parameters, peak positions, peak widths, and possible origins are listed in the Table 3.1. Since the samples were prepared at a very low P_{O2} (10^{-6} mbar) and same absorption peaks have been reported previously [26, 75, 76], it can be assumed that the dominant defects are associated with oxygen vacancies. A schematic of our proposed defect energy level model is shown in Fig. 3.2b. As summarized in Table 3.1, the 726 nm (1.71 eV) absorption is due to the transition from the defect level at 1.51 eV to CB, the 429 nm (2.90 eV) absorption is due to the transition from VB to the 2.90 eV defect level and the 513 nm (2.42 eV) absorption is due to the transition from the 0.80 eV defect level to the CB.

Table 3. 1**:** *Observed defect levels in LAO/STO heterostructures grown in P_{O2} of 10^{-6} mbar.*

Peak center (nm)	Position above VB (eV)	Position below CB (eV)	Full width half max. (eV)	Possible origin	Ref.s
429	2.90	0.33	0.20	Self-trapped exciton state / Impurity level	[23, 26, 27]
726	1.51	1.71	1.43	Deep vacancy level, i.e. oxygen vacancies trapped 1 electron	[23, 26, 27]
513	0.80	2.42	0.58	Impurity level/Energy level within CB	[25, 26]

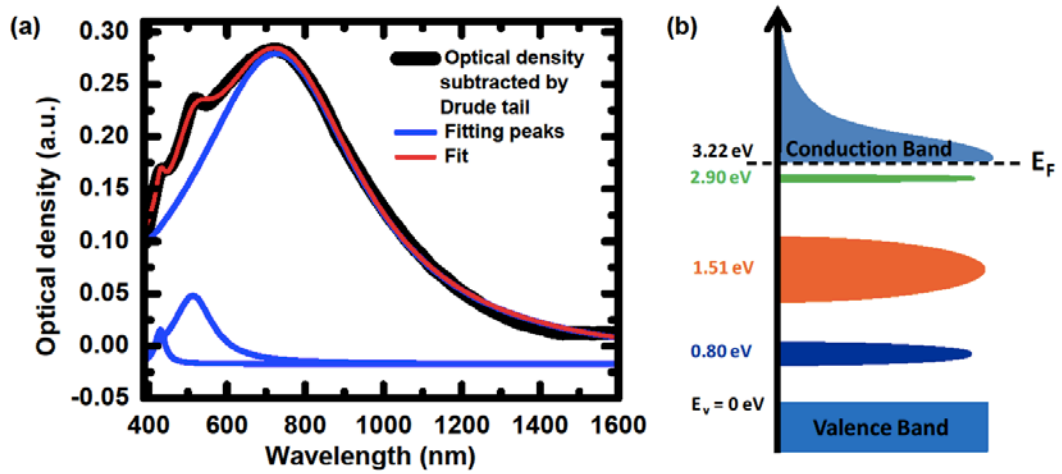

Figure 3. 2: *Defect absorption peaks and proposed energy level model. (a) Lorentzian fitting on OD of low P_{O2} LAO/STO heterostructures. Two sharp absorption peaks and a broad absorption band are demonstrated. (b) Proposed energy level model of low P_{O2} LAO/STO heterostructures. Defect levels drawn are not exactly to scale. For the exact full width half maximum, please refer to Table 3.1.*

3.3.2 Transient Absorption and Relaxation Time Determination

To understand the dynamic properties of these defect levels, the relaxation dynamics were determined by fs pump-probe technique. Figure 3.3 shows the transient absorption spectra of a low P_{O2} LAO/STO interface at different time delays after excitation with a wavelength of 800 nm. The linear power dependence of the signal indicates that only single photon

processes dominate in these experiments. There are two well defined regimes; 450-700 nm (regime 1) and 700-775 nm (regime 2).

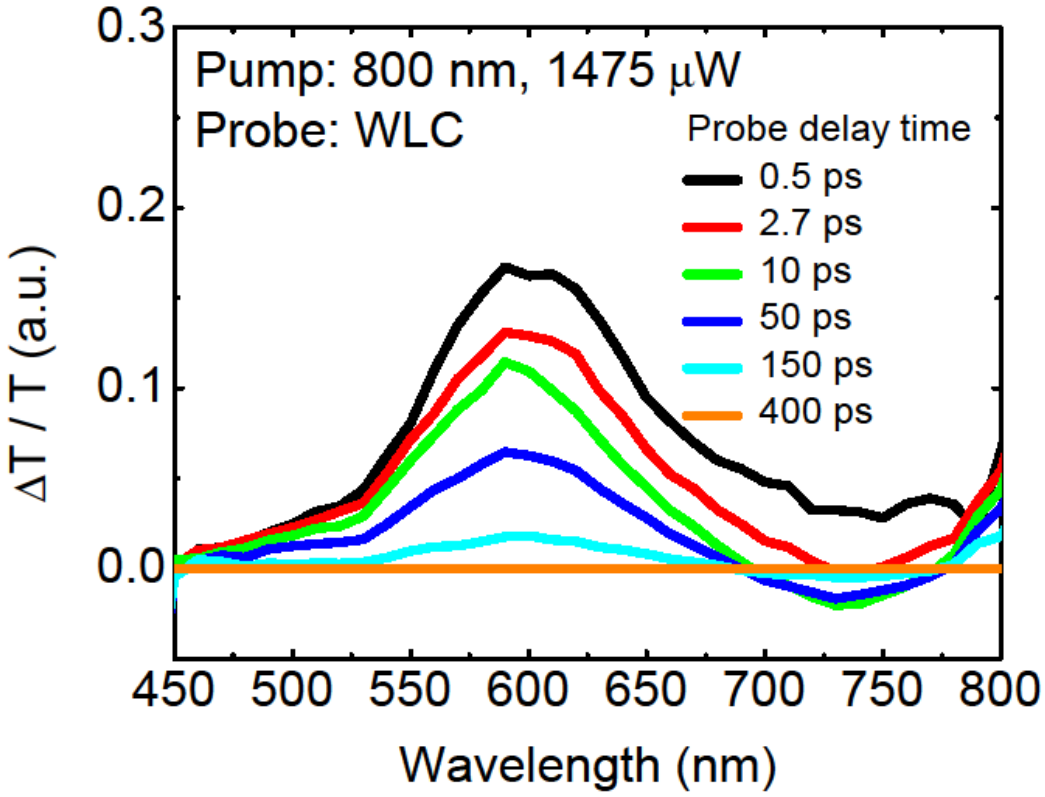

Figure 3. 3: *Transient absorption from heterostructures at different delay times.*

Single wavelength pump-probe was used to determine the relaxation process in these two regimes.

In probe regime 1 the time dependent signals at different pump intensities are shown in Fig. 3.4a. A well-defined bleaching signal was found to decay with a combination of two time constants *i.e.*, an ultra-fast component of ~1.9 ps with fitting error of 0.03 ps and a dominantly slow component of 72 ps with fitting error of 2.25 ps (Fig. 3.4b). However, in

probe regime 2, the time dynamics are considerably different as shown in Fig. 3.4c. By fitting with two exponential decay functions, a well-defined fast bleaching component with a time constant of 2.7 ps with fitting error of 0.04 ps and a slow absorption component with a time constant of 94 ps with fitting error is 1.74 ps can be clearly seen (Fig. 3.4d).

The initial state after the 800 nm pumping is an excited state with energetic hot electrons excited from both the 2.90 eV and the long wavelength side of 1.51 eV defect levels. After pump laser excitation, electrons thermalize (in sub-ps time) and then start decaying from CB minima to the various defect levels with different time constants [77].

The observed fast time component can be attributed to the decay from the CB to the nearest 2.90 eV defect level. The slow time constants (70-90 ps) correspond to the time constant involved in the filling of the broad 1.51 eV defect level from the CB. The depopulated 1.51 eV defect band is able to provide two processes namely, a bleaching process (which will give a positive change in the transmittance) corresponding to the excitation from 1.51 eV defect band and an induced absorption process (which will give a negative change in the transmittance) corresponding to the excitation from valence band (VB) to the 1.51 eV defect band. In contrast, the 2.90 eV bands can only provide a fast bleaching process at all excitations.

In probe regime 1, the accessible energy range is the excitation from the 1.51 and 2.90 eV bands to the CB. The excitations from the VB to available defect levels are not significant due to energy mismatch. Consequently, we only see a bleaching signal over this wavelength range. As can be seen in Fig. 3.4a, the dominant bleaching component consists of an excitation from the 1.51 eV band (on account of the large width of this band) with a decay

time on the order of 70 ps, consistent with the CB to 1.51 eV band decay time. The fast bleaching component in Fig. 3.4a arises from the excitation from the 2.90 eV to CB since we propose the CB to these defect levels has a fast decay component (~2 ps).

In probe regime 2, the dynamics clearly shows a dominant fast bleaching at the beginning stage and later a slow absorption component appears. The fast bleaching component can be related to the excitation from the 2.90 eV defect level and the slow absorptive component is related to the excitation from the VB to the depopulated 1.51 eV defect band (Fig. 3.4c). The slow time constant of 94 ps indicates the rate at which these defect levels are getting occupied by decay from the CB. The measured time of 94 ps is similar to the time constant obtained from the first energy regime (Fig. 3.4d). We would expect some difference between the two time constants since in regime 1 and 2 are measuring the time decay to different parts of the broad 1.51 eV defect level is measured.

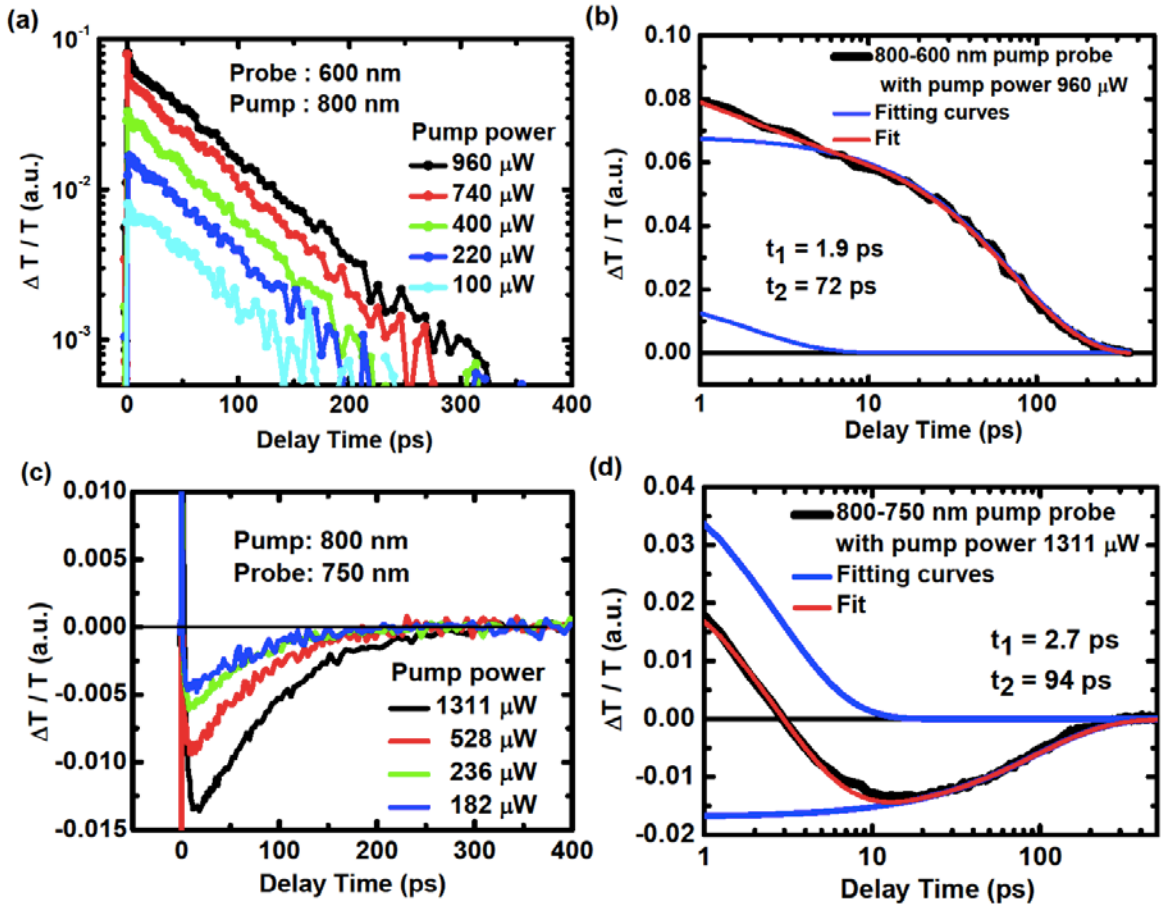

Figure 3. 4: *800-600 nm (regime 1) and 800-750 nm (regime 2) single wavelength pump-probe dynamics. (a) 800-600 nm pump-probe with different pumping powers. A single photon excitation is indicated by linear function between ΔT/T and pump power. (b) 800-600 nm pump-probe (on expanded time scale) with pump power of 960 μW are fitted by two fitted time constants. (c) 800-750 nm pump-probe (bleaching and absorption). (d) Fitting with two exponential curves (on expanded scale) with pump power of 1311 μW.*

3.3.3 Discussion on Substrate and High Oxygen Pressure Heterostructures

As we can see, in low P_{O2} samples where vast number of defects in STO substrate are dominating, three static defects are characterized by the UV-Vis-NIR spectrometer and the dynamic response of these defects is studied. The observed phenomena are found originating

from the oxygen defects deeply buried in the STO substrate. Furthermore, the results point out the similarity between low P_{O2} LAO/STO and oxygen defected STO [75].

As introduced, the conducting region in low P_{O2} LAO/STO is attributed to oxygen defects buried deeply in the STO substrate. However, for high P_{O2} samples, the conducting region is the 2D interface. Similar static and dynamic optical studies were also performed on high P_{O2} LAO/STO and as-received STO substrate. However there was no difference observed between high P_{O2} LAO/STO and as-received STO substrate. This is because the conducting region in high P_{O2} LAO/STO is too thin to be probed.

3.4 Conclusions

In summary, this chapter discusses optical studies of the defect levels in LAO/STO heterostructures grown mainly in a low P_{O2} of 10^{-6} mbar. The defects are dominated by those from the underlying STO with two sharp defect bands located at 0.8 and 2.90 eV and a broad defect band centered at 1.51 eV from the VB. By employing fs pump-probe technique, we have observed an ultrafast decay, which we have attributed to a transition from the CB to the 2.90 eV defect level and the decay time of the transition from the CB to the broad 1.51 eV defect level was found to be 72-94 ps.

Chapter 4 Magnetoresistance of Two-Dimensional and Three-Dimensional Electron Gas in $LaAlO_3/SrTiO_3$ Interfaces

4.1 Introduction

With the observations of fascinating transport properties such as superconductivity, Kondo and field effect at the LAO/STO interface [9–11, 48], understanding the role of magnetic ordering and various scattering processes has become important. To differentiate between various magnetic states, the behavior of the MR can be studied as a function of field and the angle between the current and field direction [5, 11, 78, 79]. For example, MR anisotropy measurements have been used to distinguish between weak localization and Kondo scattering [80]. In the case of the LAO/STO interfaces, several MR studies [52, 81–83] have been done to study interface anisotropy, long-range magnetism, magnetic inhomogeneities and spin-orbit scattering. Based on the observation of negative MR, Shalom *et al.* proposed the existence of magnetic ordering below 35 K for the samples prepared at the canonical P_{O2} from $5x10^{-5}$ to $1x10^{-3}$ mbar where the 2DEG is dominant [11, 83]. However, there has not been any study of the comparison of MR between the 2D and the 3D conductivity cases or the angular dependence of the MR as a function of field and the angle between the current and field direction. Such MR anisotropy measurements would be able to give us further information about magnetic ordering, transport dimensionality and various (*e.g.*, interface) scattering processes that can exist in electronic transport of a confined system.

On the other hand, there are two types of LAO/STO interfaces depending on the P_{O2} during the sample fabrication according to the discussion in the introduction chapter. Interfaces prepared in P_{O2} below 10^{-5} mbar are dominated by oxygen defects, which lead to conducting 3D electron gas buried within the STO substrates. The 2DEG occurs in interfaces prepared

in P_{O2} above 10^{-4} mbar, which most probably arises from polarization discontinuity at the interfaces. Hence, it is of great importance to study the different electrical properties from samples prepared in these two different regimes. In addition, the observed property difference can even serve as a dimensionality indicator for identifying the 2DEG in LAO/STO interfaces.

In this chapter, the MR anisotropy measurement for the LAO/STO interfaces is discussed not only for the 2DEG prepared under the conditions of $P_{O2} = 10^{-4}$ mbar, but also the 3D electron gas at $P_{O2} = 10^{-6}$ mbar. Fundamental differences were observed in MR behavior of high P_{O2} samples, where a 2DEG is expected, compared to those of low P_{O2} samples, where the electronic transport is 3D.

4.2 Experimental Procedure

Samples of 26 uc LAO were grown layer-by-layer on atomically flat TiO_2 terminated STO, under two different P_{O2} of 10^{-4} and 10^{-6} mbar. RHEED oscillations obtained from both types of the interface samples during growth are shown in Fig. 4.1a and 4.1b. Although those two oscillations are not as ideal as theory, they are typical very good RHEED oscillation in practice. These oscillations indicate good layer-by-layer growth up to the 26 uc thickness of LAO and very good sample quality. The resistance measurement was done by linear four-probe geometry.

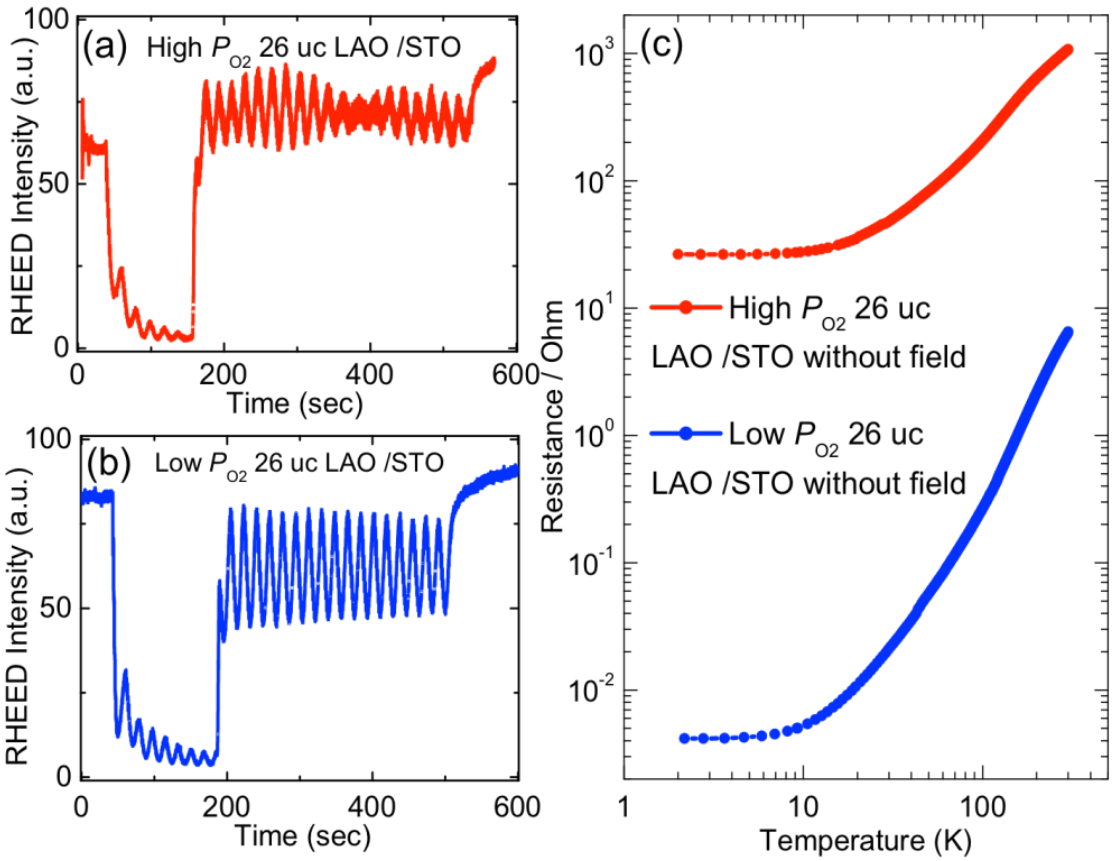

Figure 4. 1: *RHEED oscillation and resistance for samples prepared in (a) high P_{O2} and (b) low P_{O2}. Clear layer-by-layer growth was observed in both cases. (c) Large transport resistance difference for samples processed under different P_{O2}.*

Figure 4.1c shows the resistances of the two types interfaces. A large difference of two orders of magnitude in resistance values between the 2D and 3D samples was observed at room temperature and this increases to four orders of magnitude at 2 K. As commonly believed, the resistance difference is one of the key differences between the 2D and 3D interfaces with the carriers in the latter case arising from oxygen vacancies. Furthermore the growth pressure of 10^{-4} mbar also matches well with the reported critical P_{O2}, above which STO, when annealed, will remain an insulator and therefore conductance is generally at the interface [43].

MR anisotropy investigation was done in linear geometry with two different directions of magnetic field applied, namely, in-plane MR and out-of-plane MR as shown in Fig. 4.2a and 4.2b. Note that the magnetic field was always applied perpendicular to the current. The field was in the plane of the film at 0 degrees and normal to the film at 90 degrees.

4.3 Results and Discussion

4.3.1 MR Comparison for Samples Prepared under Different Pressures

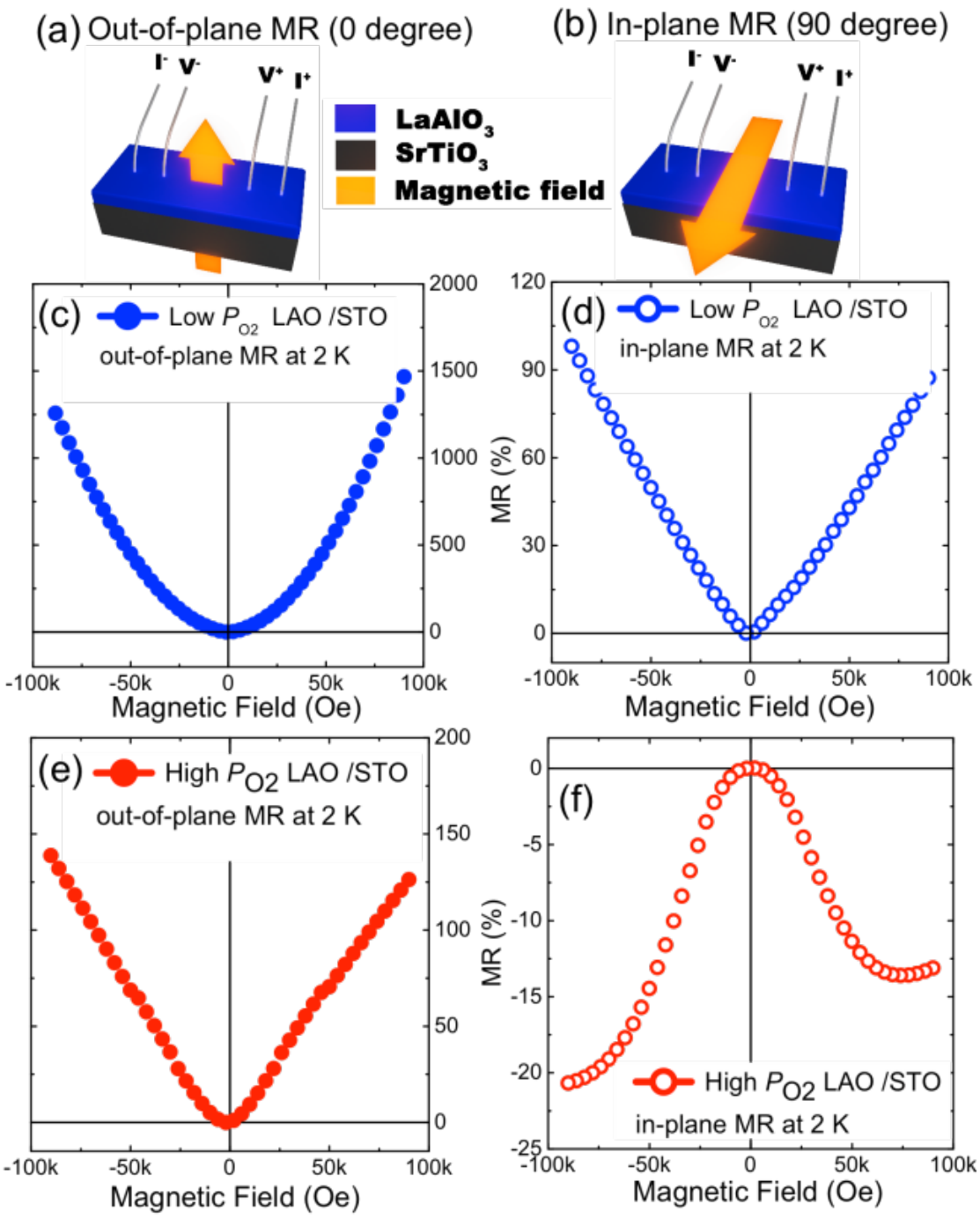

Figure 4. 2: *Comparison on MR between high P_{O2} and low P_{O2} with magnetic field applied at different directions at 2K. Illustrations for (a) out-of-plane and (b) in-plane linear measurement geometry. MR for four cases: (c) low P_{O2} LAO/STO interfaces out-of-plane MR, (d) low P_{O2} LAO/STO interface in-plane MR, (e) high P_{O2} interfaces out-of-plane MR, and (f) high P_{O2} interfaces in-plane MR. A small kink presents at ~ 40 kOe due to the changing the measuring range of multimeter.*

For the oxygen vacancies dominated 3D interfaces, a very large out-of-plane MR of ~1500% (Fig. 4.2c) and an order of magnitude lower in-plane MR of ~100% (Fig. 4.2d) were observed when magnetic field was increased up to 9 T at 2 K. While the out-of-plane MR has a quadratic relation, the in-plane MR has a linear relation with applied magnetic field. The behavior of the out-of-plane MR (quadratic dependence) is understood to be caused by increased defect scattering resulting from enhanced transit path of electrons [84]. On the other hand, the in-plane MR is mainly dominated by the interface scattering, primarily at the LAO/STO interface as the estimated cyclotron radius for the electron is of the order of micrometer at a 1 T field which is significantly larger than the thickness of the LAO layer. As a result the frequency of the interface scattering will be proportional to the cyclotron frequency, which has a linear dependence on the magnetic field. Furthermore, the reduced magnitude of the MR indicates that the interface scattering is significantly less dissipative (elastic scattering) than the defect scattering.

The MR of the 2D interfaces at 2K shows much more interesting phenomena. The out-of-plane MR in 2D interfaces is linear instead of quadratic (Fig. 4.2e). The magnitude of the MR is also an order of magnitude smaller compared to the 3D case under 9 T and closer to the case of in-plane 3D MR. Both observations support the idea of the 2D electrons scattering from the vicinal steps in STO, which have a width of the order of 200 nm, significantly smaller than the cyclotron radius. Surprisingly, a negative MR (Fig. 4.2f) is observed for the in-plane geometry, in contrast to all the other cases. The negative MR could be an indication of the onset of magnetic centers as the scattering becomes more coherent. The origin of magnetic scattering has been seen before in the form of Kondo scattering. The origin of the magnetic centers is most likely from cationic defects at the LAO/STO interface in the form of Ti vacancies or Ti^{3+}. Nakagawa and Hwang *et al*. have used electron energy

loss spectroscopy measurement of the interface to show the existence of Ti^{3+} [84]. Thus one expects a 2D plane of magnetic centers near the interface responsible for the negative MR.

Summarizing, there are three kinds of MR relations observed at 2 K: a quadratic positive MR arising from enhanced electron transit path (out-of-plane MR in low P_{O2} sample); a linear MR arising from interface scattering (in-plane MR in low P_{O2} sample and out-of-plane MR in high P_{O2} sample); and a negative MR arising from coherent scattering (in-plane MR in high P_{O2} sample). In samples prepared at high P_{O2}, the MR behavior is strongly influenced by the existence of magnetic scattering centers near the interface (a magnetic scattering plane), which are too small to be detected by other means and which accounts for a negative low temperature MR. The scattering most probably due to the vicinal steps at the substrate surface, which accounts for the linear MR observed even for the out-of-plane configuration.

4.3.2 MR Angular Dependence

Features of the MR anisotropy could also be seen from previous Fig. 4.2. To investigate the detailed features of the anisotropy, the MR under 9T for both the 2D and 3D interfaces are measured at different angles and different temperatures and are shown in Fig. 4.3. The MR and the anisotropy for both 2D and 3D interfaces are suppressed at temperatures above ~100 K. At lower temperatures, the resistance of the 3D interfaces exhibits a rough cosine relationship with respect to the measured angle and the out-of-plane (0 degree) resistance is about 4 times larger than in-plane (90 degree) resistance at 9 T and 2 K. The functional form of the angular dependence for the 2D interfaces shows the formation of a deep cusp at 90 and 270 degrees which is characteristic of 2D electron transport [42].

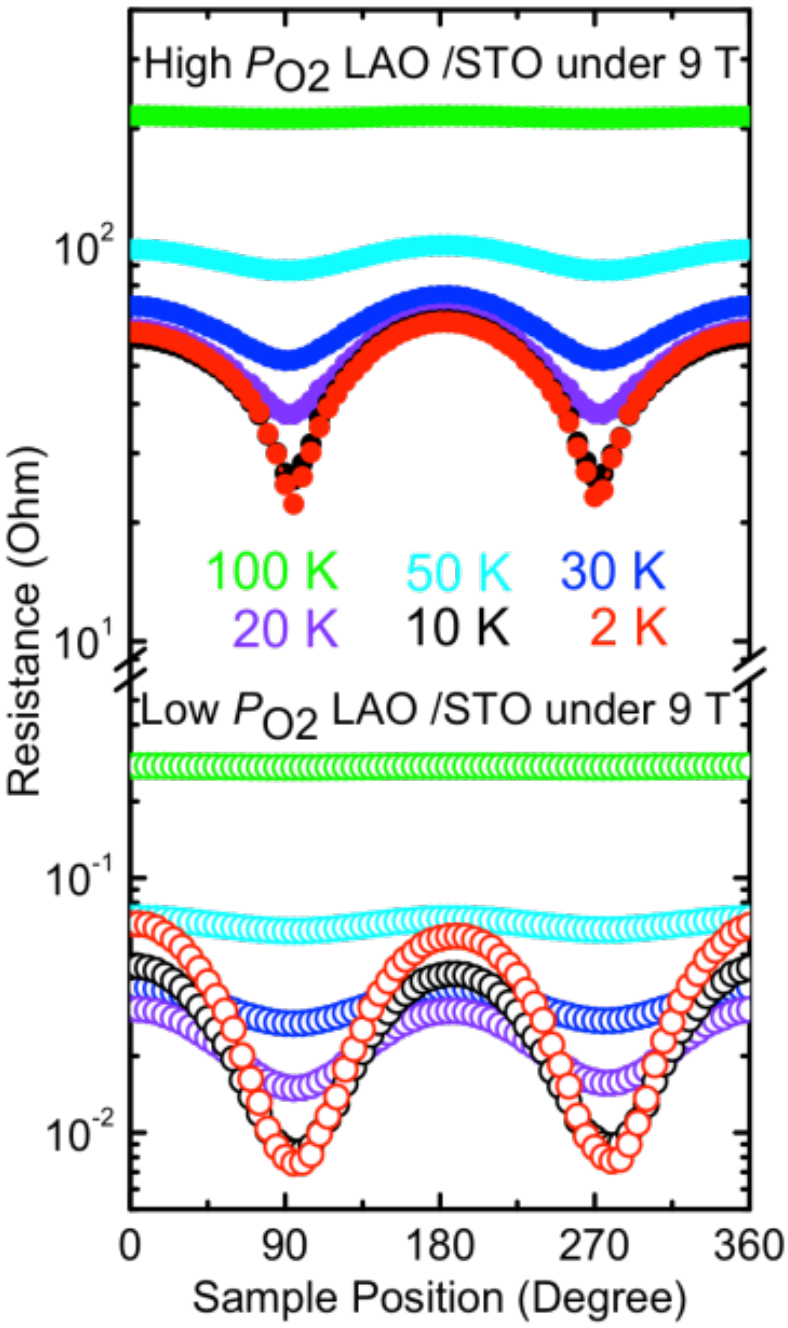

Figure 4. 3: *Resistance under 9 T magnetic field with respect to different angle for two types of interfaces.*

Figure 4.4 shows a closer comparison of the angular dependence of the 2D and the 3D cases at 2 K and 9 T. In the 2D interfaces, a negative MR is observed for the in-plane geometry

(90 degree) and positive MR for the out-of-plane geometry (0 degree). To vividly demonstrate the MR anisotropy of the different types of interfaces, two different plots were used to present the MR anisotropy at 2 K under 9 T. As can be seen in Fig. 4.4, the negative MR for the in-plane geometry for 2D interfaces is very obvious. The shape and amplitude differences between the 2D and 3D interfaces could be clearly observed in these plots.

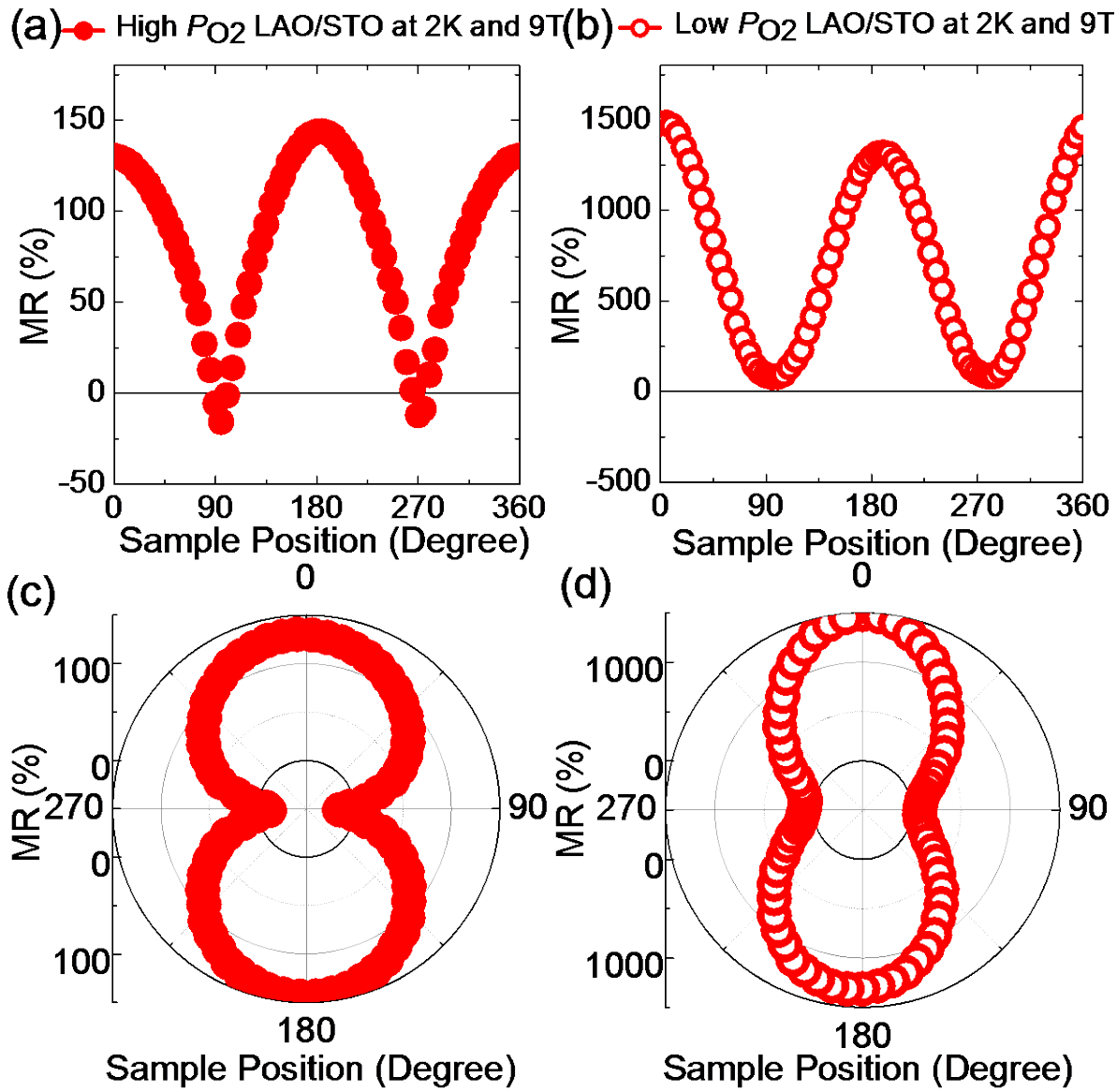

Figure 4. 4: *Various plots for MR of different interfaces under 9 T magnetic field at 2 K. Normal plot for 2D interfaces (a) and 3D interfaces (b); Polar plot for 2D interfaces (c) and 3D interfaces (d).*

4.3.3 MR Temperature Dependence

The observed different scattering mechanisms also have temperature dependences, as illustrated in Fig. 4.5 for the in-plane resistance and in-plane MR of the 2D interface. For the 2D samples prepared in higher pressures of 10^{-3} mbar, the Kondo effect has been clearly seen, but not for samples prepared in 10^{-4} mbar as the concentration of the magnetic centers is too low. However, a magnetic field can align these residual centers, which induces a more coherent scattering resulting in a negative MR. The negative MR is therefore an even more sensitive probe for the presence of magnetic centers than Kondo scattering. This negative MR vanishes beyond 20 K and turns progressively positive at higher temperatures, due to the disruption of the exchange interaction between the magnetic centers by thermal excitations. This accounts for the downward trend of the MR signal with decreasing temperature starting at 30 K and becomes negative below 20 K. However, the abruptness of the MR transition at 30 K suggests an effect of the structural phase transition in STO (orthorhombic to rhombohedral) [20–22] on the observed change in the MR behavior. Further study is required to elucidate this.

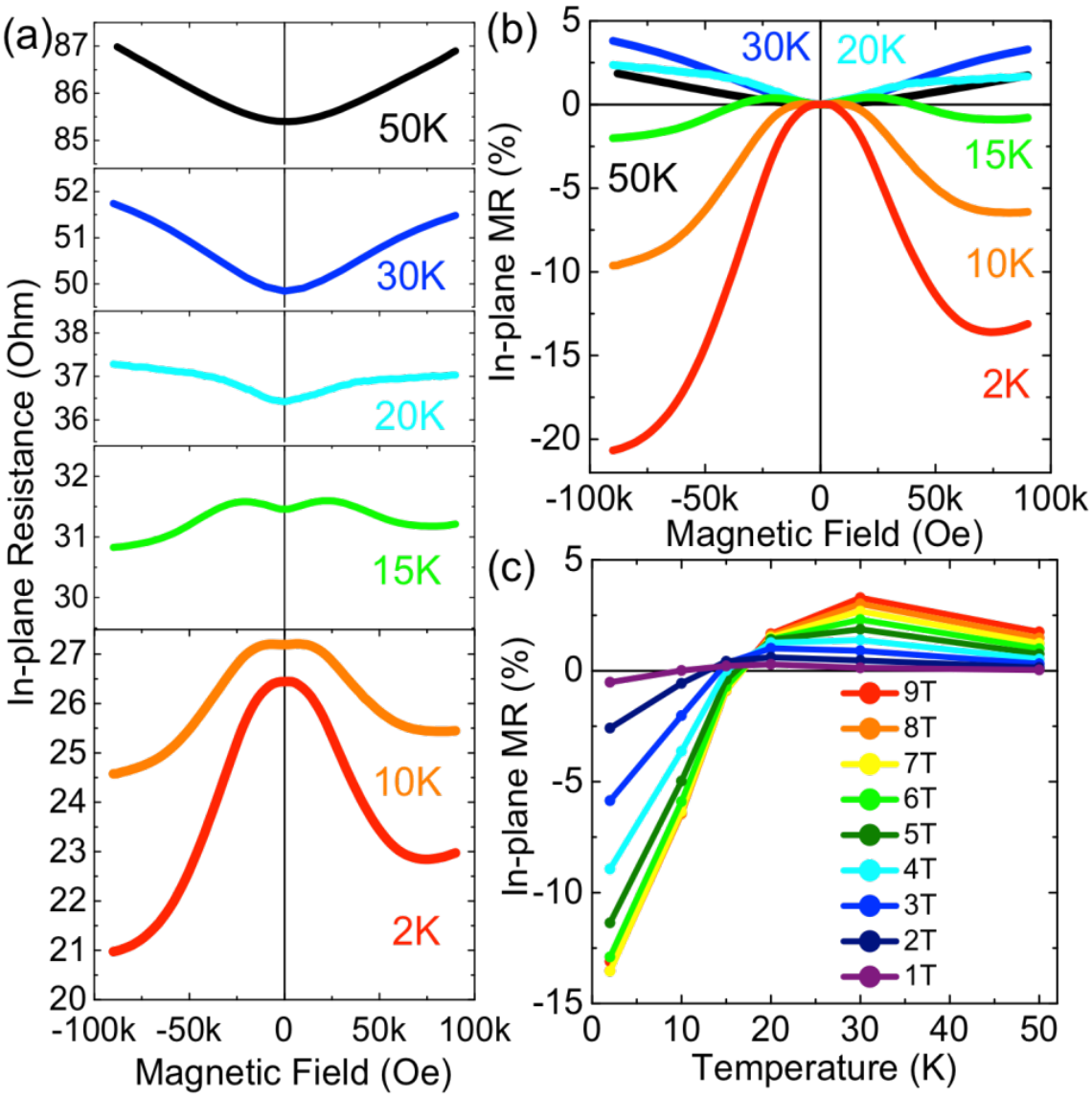

Figure 4. 5: *Temperature dependence for in-plane resistance (a) and in-plane MR (b and c) for high P_{O2} LAO/STO interfaces.*

4.4 Conclusions

In summary, a comparison of MR anisotropy in LAO/STO interfaces prepared under different P_{O2} is presented in this chapter. Large anisotropies were found in both 2D and 3D interface samples and three distinct scattering mechanisms were observed. The observed anisotropy features and temperature dependence suggest the role of interface scattering in

addition to enhanced electron paths under a magnetic field. The samples with the 2DEG also indicates the role of a magnetic plane that is effective at low temperatures in introducing a coherent scattering process leading to a negative MR. Furthermore, the MR anisotropy can serve as a dimensionality indicator.

This study also supports the formation of a magnetic scattering near the 2D electron interface and suggests the lower dissipation of scattering at interfaces as opposed to defect scattering losses due to enhanced electron transit paths. Therefore, MR anisotropy is a sensitive technique for understanding the role of magnetic ordering and various scattering processes in the transport of 2DEG.

Chapter 5 Electronic Phase Separation at the $LaAlO_3/SrTiO_3$ Interface

5.1 Introduction

Recently, Popovic *et al.* [85] have theoretically predicted that the transferred charges at the LAO/STO interface occupy nearly ten interface sub-bands. This suggests that magnetic phases are theoretically possible in this system, with most of the charges preferably transferred to a couple of sub-bands. Brinkman *et al.* [11] have shown recently that stronger magnetic property is expected if higher P_{O2} pressure is used during the preparation of the interfaces.

On the other hand, magnetic properties have been well-studied on complex oxide material systems such as underdoped cuprates and doped manganites in both bulk and thin films [86–91]. In these material systems, the spatially coexisted electronic and/ or magnetic phases exist as the nanoscopic phases and this phenomenon is generally called electronic phase separation (EPS). In the case of manganites, these phases have the similar energy, resulting in inhomogeneous ground state. Hence orbital selective occupancy, Coulomb interaction, Hund's coupling and Jahn-Teller distortions play a significant role in determining the nature of the electronic and magnetic state. However, there was no evidence on EPS at the LAO/STO interfaces yet.

This chapter presents for the first time evidence for the existence of electronic phase separation at LAO/STO interfaces.

5.2 Experimental Procedure

The LAO/STO interfaces were prepared by depositing 10 uc of LAO on a TiO_2-terminated 5×5×0.5 mm^3 STO (001) substrate (double-side polished) in a wide range of P_{O2} from 1×10^{-6} to 5×10^{-2} mbar at 850°C using PLD and a single-crystal LAO target. The laser pulse (248 nm) energy density was 1.8 J/cm^2 and the repetition rate was 1 Hz. During deposition, the film growth was monitored using *in-situ* RHEED, which revealed layer-by-layer growth for samples grown in 1×10^{-6} up to 1×10^{-2} mbar (close to 3D-growth) deposition pressure (Fig. 5.1a and 5.1b). For samples grown at 5×10^{-2} mbar, the RHEED oscillation started to deviate from normal layer-by-layer growth, indicating island growth (Fig. 5.1c). After deposition, all samples were cooled to room temperature in oxygen at the deposition pressure.

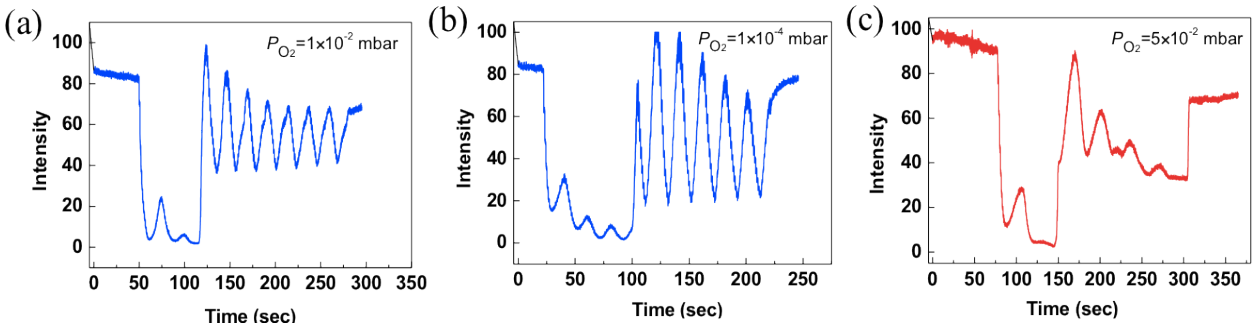

Figure 5. 1: *RHEED data for samples prepared at P_{O2} of (a) 1×10^{-2} mbar and (b) 1×10^{-4} mbar show clean oscillations that indicate 2D growth. (c) A deformed RHEED oscillation for a sample grown at 5×10^{-2} mbar indicates commencement of a 3D growth process.*

Before the electrical transport measurements, the magnetic properties of the samples were measured using SQUID. For measurements of the magnetization as a function of temperature, the samples were first cooled to 2 K. The magnetization data were then collected using a series of low magnetic fields ranging from 0.005 to 0.5 kOe during

warming from 2 K to room temperature. The magnetic field was applied parallel to the sample surface.

The sheet resistance, n and μ were measured using a Van der Pauw geometry. The sheet resistances (Fig. 5.2a) of the samples grown at $P_{O2} \leq 10^{-5}$ mbar (low pressure samples) are ~10 Ω/□ at 300 K and ~1 mΩ/□ at 5 K with an almost constant n of ~10^{17} cm^{-2} and an increase in μ (Fig. 5.2b) to ~10^{4} $cm^{2}V^{-1}s^{-1}$ at 5 K, which is consistent with earlier reports [9–13, 43, 48, 92, 93]. The sheet resistances of the samples grown at $P_{O2} \geq 10^{-4}$ mbar (high pressure samples) are 9–13 kΩ/□ at 300 K and gradually decrease to ~200 Ω/□ at 5 K; n is reduced by a factor of four from (0.8–1.0)×10^{14} cm^{-2} at 300 K to (2.0–2.5)×10^{13} cm^{-2} at 5 K, indicating significant charge localization. The μ increases significantly to ~10^{3} $cm^{2}V^{-1}s^{-1}$ at 5 K, which suggests that metallic and other (non-conducting) electronic phases coexist. Furthermore, the overall resistivity exhibits metallic behavior without any discontinuity, despite the change in n through localization by a factor of four and the μ enhancement of more than an order of magnitude.

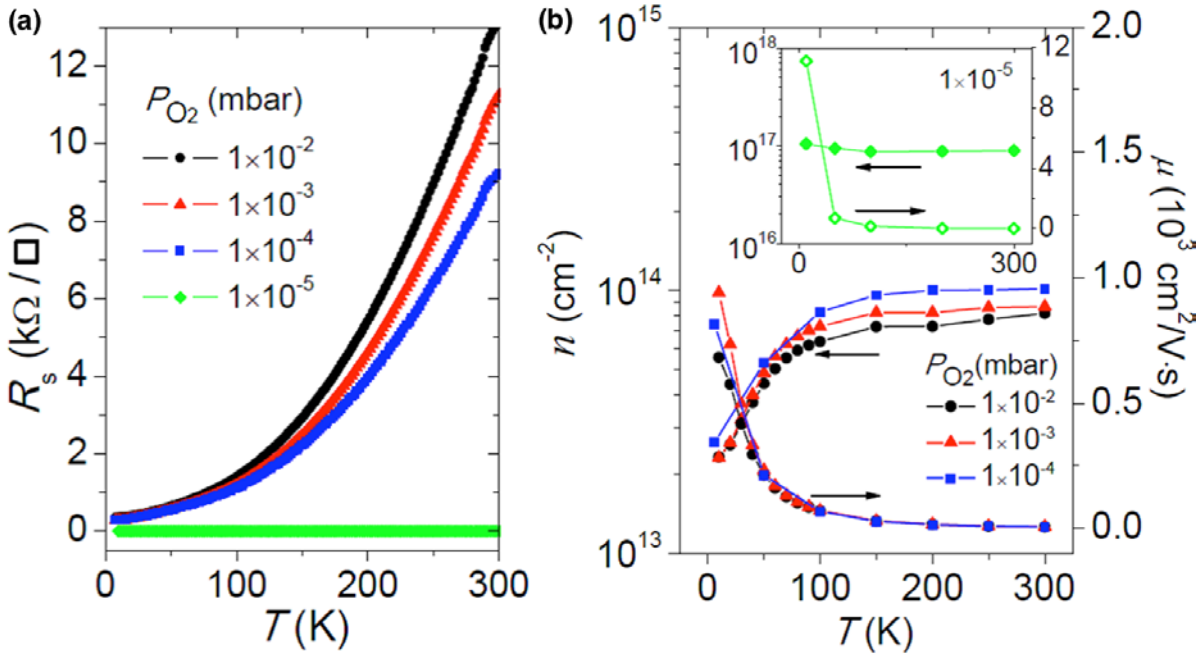

Figure 5. 2: *Electrical properties. (a) Temperature-dependent sheet resistance (R_s versus T) of 10 unit-cells of LAO on STO prepared at 850 °C under different P_{O2} of 10^{-5}, 10^{-4}, 10^{-3}, and 10^{-2} mbar while still maintaining two-dimensional growth. (b) n and μ of the corresponding samples in (a) as a function of temperature.*

To rule out any contamination issue, secondary ion mass spectrometry (SIMS) studies were performed on all samples. During the measurement, the samples were bombarded with high energy ions and some atoms were ionized and sputtered off the surface. Then, these secondary ions were collected, filtered according to atomic mass and projected onto an electron multiplier, Faraday cup, or charge-coupled device screen. Because the sputtering process could ionize deeper and deeper atoms as time goes by, the SIMS depth profile data can be achieved for different elements. The content of magnetic elements in the sample were calculated based on relative sensitivity factors from Stevie and Wilson [94]. The SIMS depth profile data (Fig. 5.3a) for the LAO (10 uc)/STO sample shows that the impurity (including magnetic elements such as Fe, Ni, Co, Cr and Mn) signals are within the measurement noise. As shown in Fig. 5.3b, it is clear that all the impurities [94] in all

samples are within the noise level, which is at a concentration level of greater than four orders of magnitude lower than the Sr/Ti concentration.

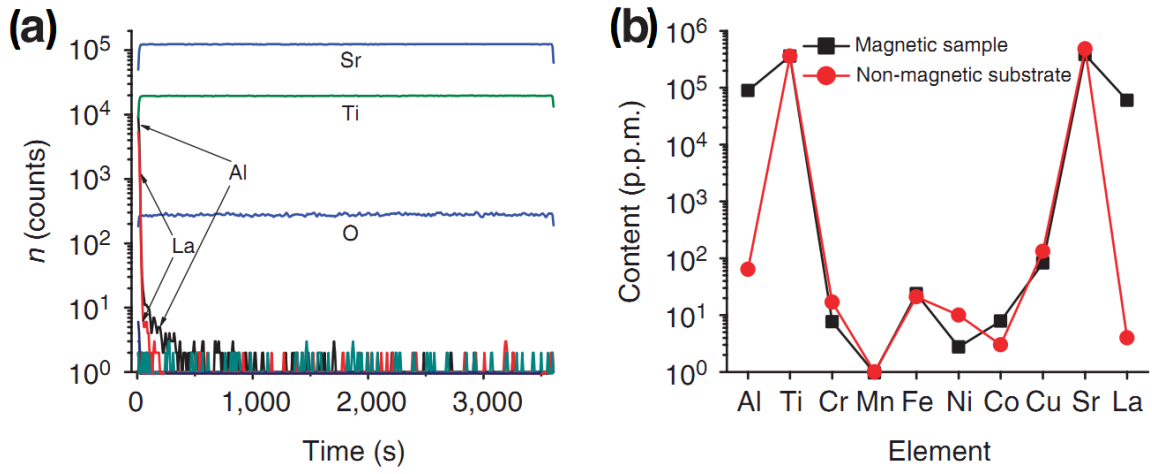

Figure 5. 3: *SIMS characterization on LAO/STO interface and STO substrate. (a) The SIMS depth profile data for the magnetic LAO (10 uc)/STO show the total counts versus sputtering time for all the det3ected elements (Sr, Ti, La, Al, B, C, Na, Mg, Si, K, Ca, Cr, Mn, Fe, Ni, Co, Cu, Nb, Ta and Bi). All impurity elements show traces below ten coundts. (b) The content of magnetic elements (Cr, Mn, Fe, Ni and Co) in the magnetic LAO (10 uc)/STO sample and the non-magnetic STO substrate.*

5.3 Results and Discussion

5.3.1 Magnetization versus Temperature and Magnetic Field

Figure 5.4 summarizes the magnetic properties of the samples grown at $P_{O2} = 1\times10^{-2}$ mbar. It must be noted that the P_{O2} under which these films were prepared is at least an order of magnitude higher than those used in previously published reports. Figure 5.4a shows the zero-field-cooled (ZFC) and field-cooled (FC) magnetization data of the samples as a function of temperature (collected while warming the sample from 2 K to 300 K using a small (0.1 kOe) applied magnetic field). For ZFC, a large negative magnetization value

indicating a giant diamagnetic response is observed below 60 K, whereas for FC (1 kOe), a positive value, which indicates a paramagnetic response, is seen. In a separate set of measurements, magnetization loops as a function of applied magnetic field (±2 kOe sweep) starting with a positive field were measured at several temperatures. Notably, there is an overlapping ferromagnetic response additional to the diamagnetic or paramagnetic response, as seen in the form of hysteresis loops extending up to room temperature (Fig. 5.4a, also shown in Fig. 5.4b after background subtraction). In these field sweep curves, the standard temperature independent diamagnetic contribution of the STO substrate is also discernible. Depending on the cool-down field, the starting point of the hysteresis loops is approximately centered on the diamagnetic (ZFC case) or paramagnetic (FC case) saturation value.

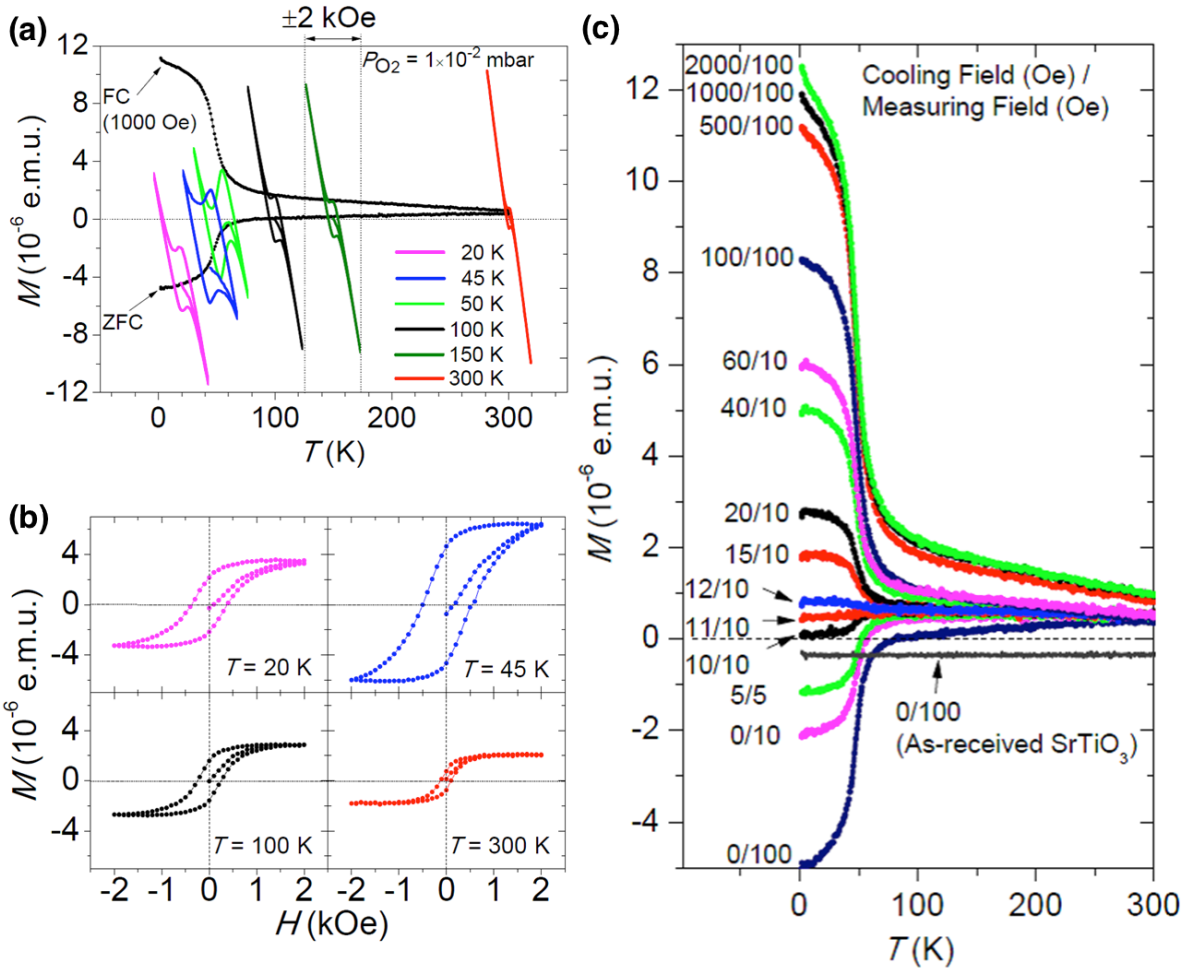

Figure 5. 4: *Magnetic properties. (a) The 1 kOe field-cooled (FC) and zero-field-cooled (ZFC) in-plane magnetisation (M) data as a function of temperature (T) and measured by a 0.1 kOe magnetic field applied while warming the sample from 2 K to 300 K (solid black lines) for the 10 unit-cells of LAO/STO samples prepared at an* P_{O2} *of* 1×10^{-2} *mbar. In a separate measurement after ZFC, ferromagnetic hysteresis loops centred on the diamagnetic branch are observed when sweeping a ±2 kOe magnetic field applied at each temperature. Similar ferromagnetic loops are also observed on the paramagnetic branch when the hysteresis loops are collected after FC (not shown here for clarity). (b) The temperature-dependent ferromagnetic loops in (a) after diamagnetic and paramagnetic subtraction. (c) Magnetisation as a function of temperature under various cooling temperatures and magnetic fields for the 10 unit-cells of LAO/STO samples prepared at* $P_{O2} = 1\times10^{-2}$ *mbar.*

5.3.2 Oxygen Partial Pressure Dependence

The existence of the magnetic state critically depends on the LAO/STO interface processing parameters, mainly P_{O2}. Figure 5.5a and 5.5b show the magnetic response of various samples grown at different P_{O2}. For samples grown at $P_{O2} \leq 1\times10^{-3}$ mbar, the magnetic responses are much smaller with an almost unnoticeable transition in the ZFC cases. The most interesting regime is the high P_{O2} region, which has not been explored thoroughly until now because it is too close to the 3D-growth regime. However, all our samples prepared at $P_{O2} \leq 1\times10^{-2}$ mbar show clean RHEED oscillations, indicating 2D-growth.

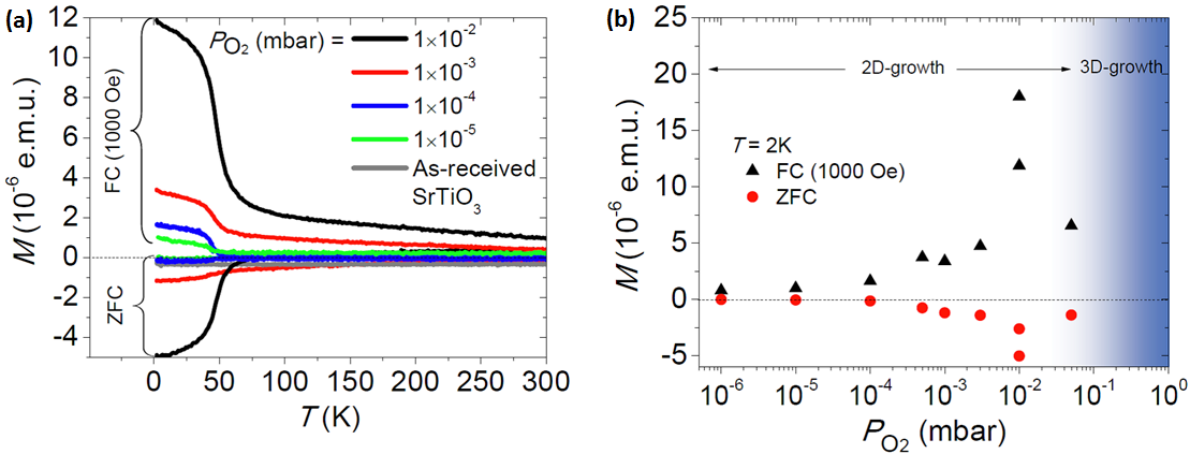

Figure 5. 5: *Influence of the processing parameters. (a) Magnetisation (M) as function of temperature (T) for samples prepared under different* P_{O2} *of* 10^{-5}, 10^{-4}, 10^{-3}, *and* 10^{-2} *mbar. (b) The zero-field-cooled (ZFC) and field-cooled (FC) magnetisation data as a function of* P_{O2} *conditions. The data were taken while warming the samples from 2 K to 300 K in a 0.1 kOe applied magnetic field.*

5.3.3 EPS Hypothesis

What is the magnetic contribution of each material in the LAO/STO interface structure? To answer these questions, we subjected the TiO_2-terminated STO substrates to identical surface preparation, temperature, P_{O2} and cool down conditions without deposition of any LAO layer on top. Surprisingly, the diamagnetic (ZFC) and paramagnetic (FC) transitions also appeared (Fig. 5.6) but with values 50% lower than those observed in the LAO/STO samples.

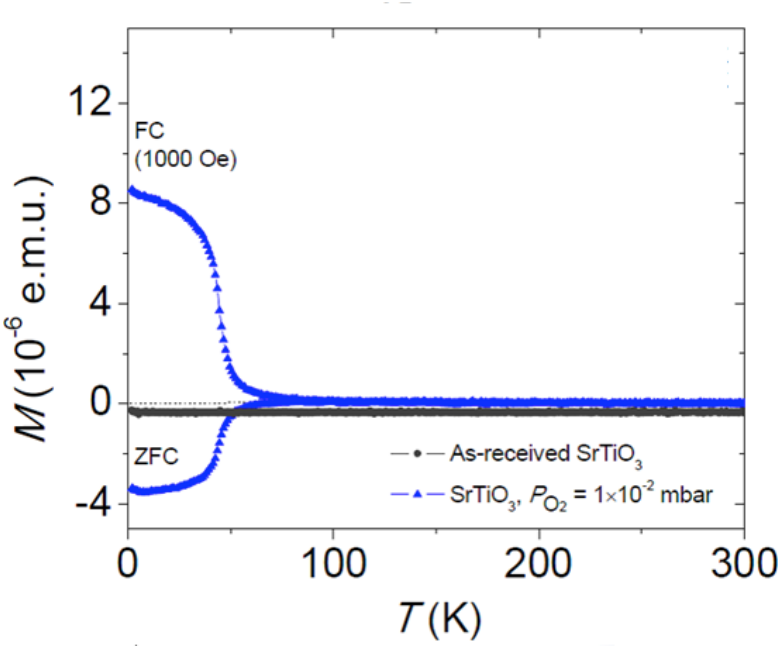

Figure 5. 6: *The ZFC and FC magnetisation data of STO prepared under conditions similar to those used for the 1×10^{-2} mbar LAO/STO samples.*

Furthermore, tiny magnetic hysteresis loops seen in annealed STO (Fig. 5.7a and 5.7c) were one order of magnitude smaller than that seen in the case of LAO/STO (Fig. 5.7b and 5.7d). It should be noted that as-received and TiO_2-terminated STO substrates that are not subjected to the above processing steps show no magnetic effect. And no loop was observed over the entire temperature range for the as-received STO. Because the thermally treated STO shows both the diamagnetism and paramagnetism below 60K, but with the LAO layer above it, very large ferromagnetic loops are observed, we argue this is a surface/interface effect enhanced by charge transfer.

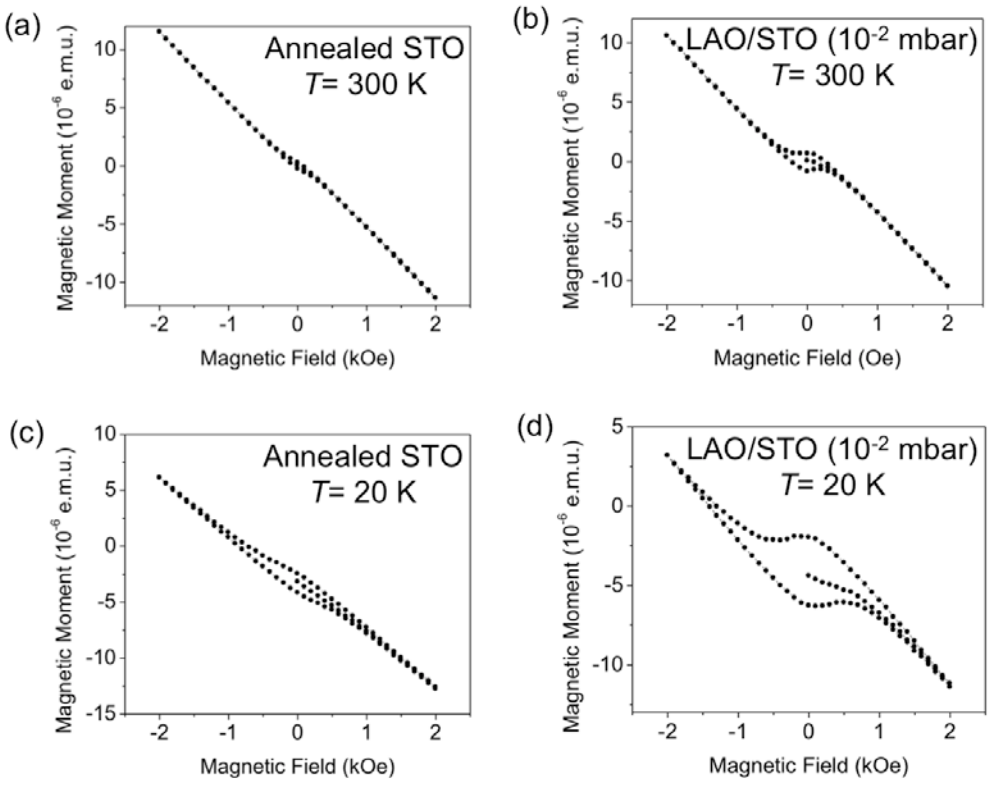

Figure 5. 7: *Magnetization hysteresis loops observed on both annealed STO and LAO/STO sample at 300 K and 20 K.*

Intriguingly, the ~60 K transition temperature below which a very large magnetic response is observed coincides with low-temperature structural phase transitions in STO (tetragonal to orthorhombic at 65 K and then to rhombohedral at a lower temperature around 30 K) [20, 21, 95]. As can be seen in the Fig. 5.8, the temperature-dependent X-ray diffraction data for the samples shows that splitting of the STO diffraction peaks starts to appear between 73 and 53 K and grows as the temperature is reduced to 12 K, indicating phase transformation in STO. This indicates that the surface of the STO and its phase transition are critical for the origin of these magnetic properties and that the role of LAO is to significantly amplify these effects via formation of a 2DEG at the LAO/STO interface. The observed magnetic effects in the treated STO samples can be explained by a migration of electron-like carriers from a

finite density of vacancies to the surface of the samples to gain free energies similar to those of the transferred charges at the LAO/STO interface.

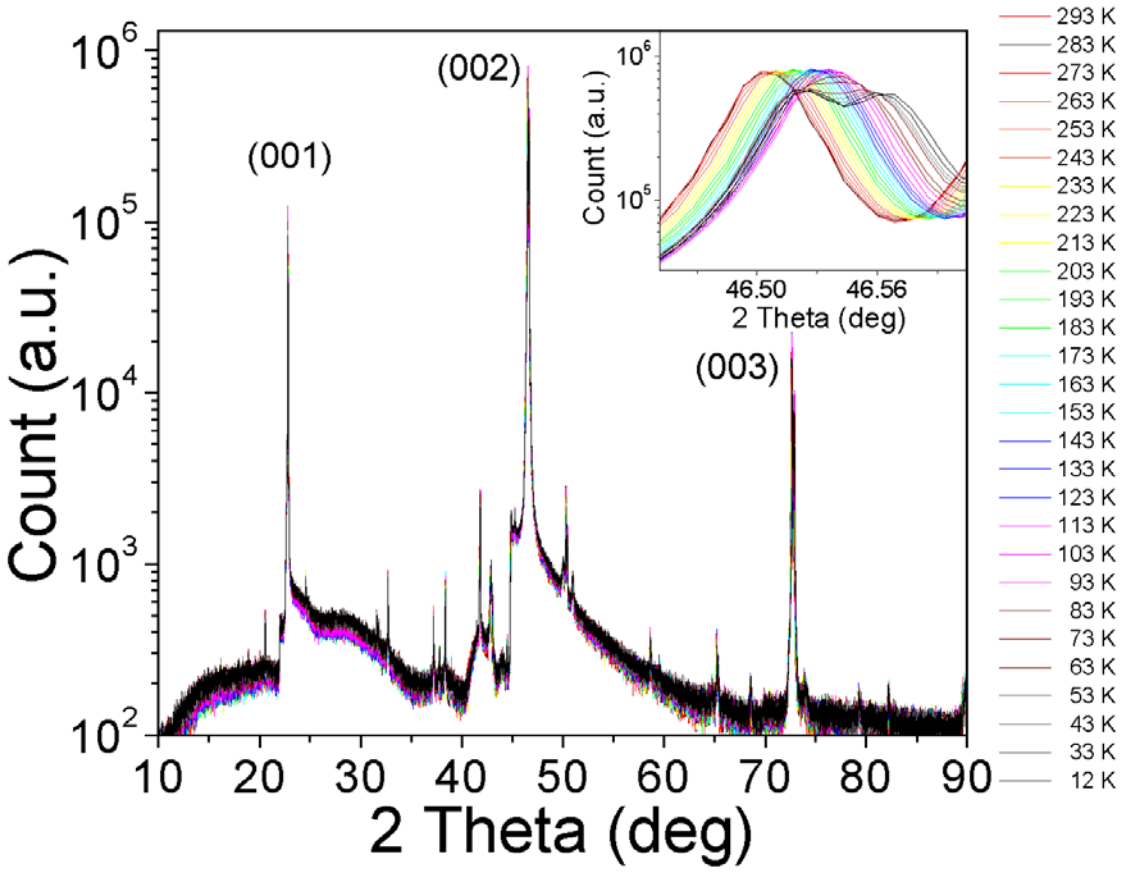

Figure 5. 8: *The temperature-dependent X-ray diffraction pattern of STO. Insert: The splitting of the (003) peaks (splitting of other peaks not shown) that appears at temperatures between 73 and 53 K and grows as the temperature is reduced to 12 K.*

In the following, the origin of these magnetic properties in this system is hypothesized. Electronic structure calculations by Popovic *et al.* [85] suggest that all the transferred electrons (~0.5*e* per interface La-atom) are shared by different interface bands near the Fermi energy. The corresponding charge density is spatially homogeneous in the direction parallel to the interface and quickly decays in the direction perpendicular to the layer. It is known that electron-electron or electron-lattice interactions, Jahn-Teller effects, strain and

disorder can modify the band picture considerably and lead to nanoscale charge inhomogeneities. Hence, we believe that there is a preferential occupancy of a smaller number of bands due to the possible interactions mentioned above. Depending on the preferred orbitals, the transferred charges from LAO in a few uc of thickness get organized into three states: i) 2D dense electron domains with a large diamagnetic moment, ii) 2D ferromagnetic nanoscopic regions and iii) a background of 2DEG. Illustrated in the Fig. 5.9, a schematic drawing of possible distribution in a spatially inhomogeneous fashion for these three states is plotted. Therefore, we attribute the origin of these magnetic properties to the EPS. The crucial factor that explains why the three states, that is, ferromagnetic, diamagnetic and/or paramagnetic, and the quasi-2D electron gas can coexist within a few unit cells of the LAO/STO interface is their nearly identical free-energy density. The polarization state of $SrTiO_3$ at nanoscopic scales and other factors, including temperature, control how the interface charges are distributed among the three electron reservoirs.

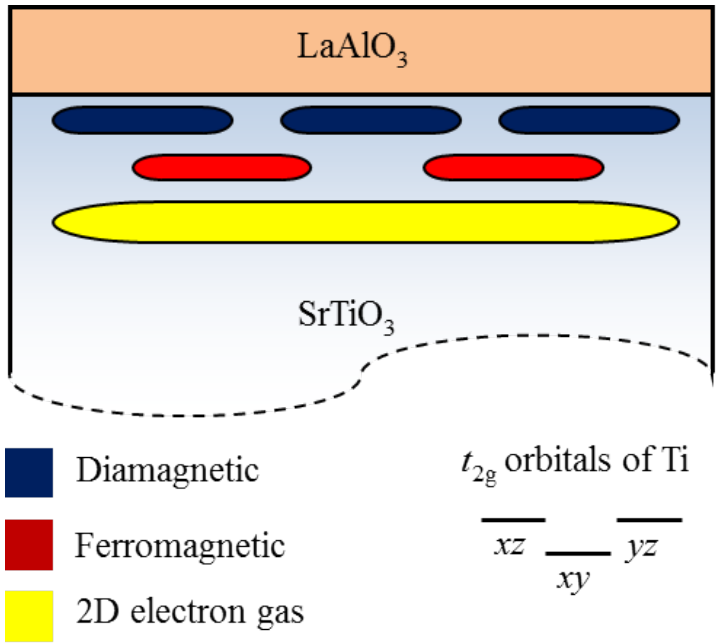

Figure 5. 9: *Schematic of the various phase separated domains as a function of depth from the interface.*

5.3.4 Nature of the Conducting Channel

In order to examine the above proposed spatially inhomogeneity, properties of each layer of STO need to be studied. This property can be investigated by growing the LAO/STO interface with different STO thicknesses on an insulating substrate. Considering its strain and highly insulating properties, NGO substrate was selected as the substrate in this study. The lattice constants in pseudocubic lattices of STO, NGO, and LAO are 3.905, 3.858, and 3.79 Å, respectively [44]. When LAO is directly grown on STO, the strain is as large as -3% and is mainly manifested at the LAO/STO interface. If the STO layer is first grown on NGO, the large mismatch between LAO and STO will be partially transferred from LAO/STO to the STO/NGO interface. Hence, LAO/STO interfaces on NGO substrates with fixed 15 uc LAO (above the 4 uc critical thickness [10]) were grown with the STO thickness controlled from 3 to 20 uc.

The room-temperature n (the n is not normalized by film thickness) and μ dependence on the numbers of STO layers are compared in Fig. 5.10a and 5.10b. Clearly, an abrupt enhancement on n from 0.9×10^{14} to 2.9×10^{14} cm^{-2} is seen when the STO thickness is increased from 6 to 8 uc. And n seems to saturate at about 2.7×10^{14} cm^{-2} in 12 and 16 uc STO layer, and falls to 0.8×10^{14} cm^{-2} at 20 uc due to the strain relaxation. On the other hand in Fig. 5.10b, the linear dependence of μ on STO thickness has been observed from 3 to 12 uc, which proves that the STO layer is truly the conducting channel for 2DEG. When further increasing the STO thickness to 16 and 20 uc, a nearly-constant μ (that is close to the conventional LAO/STO interface) is achieved. It suggests that the conducting channel for 2DEG cannot be increased for STO thickness beyond 12 uc. Therefore, the propagating

depth of 2DEG in STO layer can be determined to be very close to 12 uc. This is a clear proof of the 2DEG part of our hypothesis.

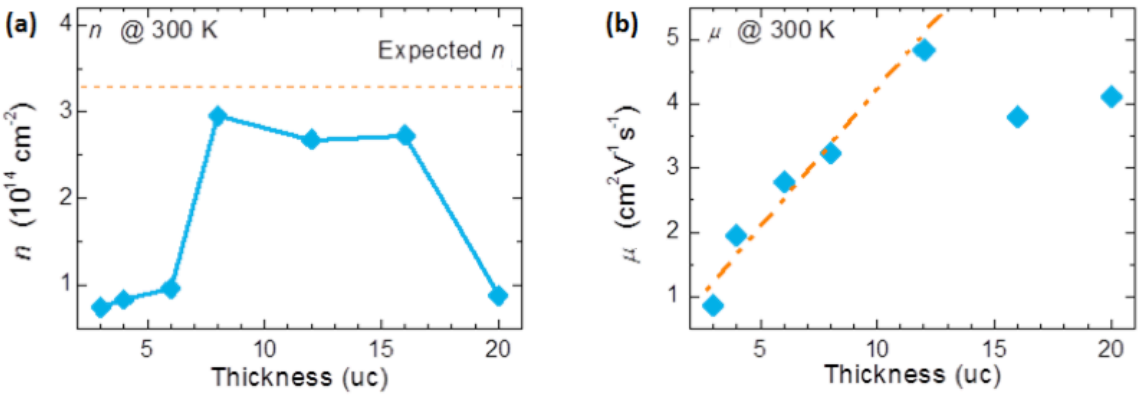

Figure 5. 10: *The STO-thickness-dependent n and μ at 300 K are shown in (a) and (b), respectively.*

For the smaller *n* and μ observed in 3 to 6 uc STO sample compared with samples with thicker STO, the multiply split Ti sub-bands at the interface [85, 96] should be taken into consideration according to the hypothesis. Within the 2DEG propagating depth of nearly 10 to 20 uc (~ 4 to 8 nm), the $3d_{xy}$, $3d_{yz}$ and $3d_{xz}$ orbits of Ti are no longer degenerate near the LAO/STO interface. The $3d_{xy}$ is thought to be the lowest singlet orbit because of the two-dimensional nature of the interface, while $3d_{yz}$ and $3d_{xz}$ orbits are degenerate but with a higher energy compared to $3d_{xy}$ energy. In recent theoretical calculations [96], it was shown that the $3d_{xy}$ orbit plays a dominant role in a 2 nm STO layer from the interface, while the $3d_{yz}/3d_{xz}$ bands begin to transport electrons beyond this interface. Based on this, for STO thickness below 6 uc, the conducting channel is dominated by localized $3d_{xy}$ orbitals, in which electrical conduction occurs by hopping. So, in the thinner STO layer ($n \leq 6$ uc) the observed smaller *n* and μ is understandable. When the STO thickness is 8 uc or above, the electrons are no longer dominated by the singlet $3d_{xy}$ orbitals, and the delocalized $3d_{xz}/3d_{yz}$

bands start to play a dominant role. As a result, the n_S reaches the highest value and the μ start to increase.

The above model that contains multiply split Ti sub-bands and the interface scattering can well explain all the data observed in the LAO/STO/NGO interfaces. In addition, if this model is correct, it perfectly proves the hypothesis we proposed in the previous section. As there are less electrons in a thinner STO layer, the localized states dominating here can be associated with the strong magnetic interaction observed in the previous section. Recent experimental results indicate that the magnetism in 2DEG is not influenced by itinerant electrons [97], and the localized electrons with Ti^{+3} may be the origin of magnetism. It means that the increasing number of Ti^{+3} from localized electrons in the limited STO conducting channel can provide a stronger magnetic interaction.

Figure 5.11 present thickness and temperature dependence of MR denoted as [R(H)-R(0)]/R(0). In Fig. 5.11a, the MR at different temperatures is presented for the 6 uc sample when the magnetic field is applied parallel to the current based on the technique discussed in the previous chapter. The MR can be divided into two components, one of which is the unsaturated positive MR at high fields and the other is the negative MR at low fields. Moreover, a typical butterfly-like hysteresis is observed. In order to exclude that the hysteresis is induced by thermal fluctuation or detrapping of trapped carriers, the MR at 2 K is measured twice continuously, and the same hysteretic behavior is obtained. So an intrinsic magnetism is needed to account for the negative MR in the 6 uc sample which is consistent with our expectations as discussed earlier. On increasing the temperature, both the positive and negative MR are suppressed indicating the reduction of magnetic interactions at the higher temperatures. For the transplanted LAO/STO interface with 12 uc STO layers in Fig.

5.11b, the positive MR is one-order of magnitude smaller with no hysteresis when compared with 6 uc sample, revealing the much weaker magnetic interaction and scattering at an ideal interface. These results are consistent with our observation that the thinner STO samples with strongly localized 2DEG show some magnetic effects from localized electrons while for the thicker samples such effects are buried by conducting layer. Recently, these in-plane ferromagnetic dipoles have also been confirmed and visualized in real space [50, 97], revealing the two-dimensional nature of this ferromagnetism in the 2DEG system. And the positive MR background further confirms that the singlet $3d_{xy}$ orbit is highly involved with electron transport. As shown in Fig. 5.11c, this high density of localized electron will induce a lot of spin flips during electron transport, resulting in a strong positive MR as observed.

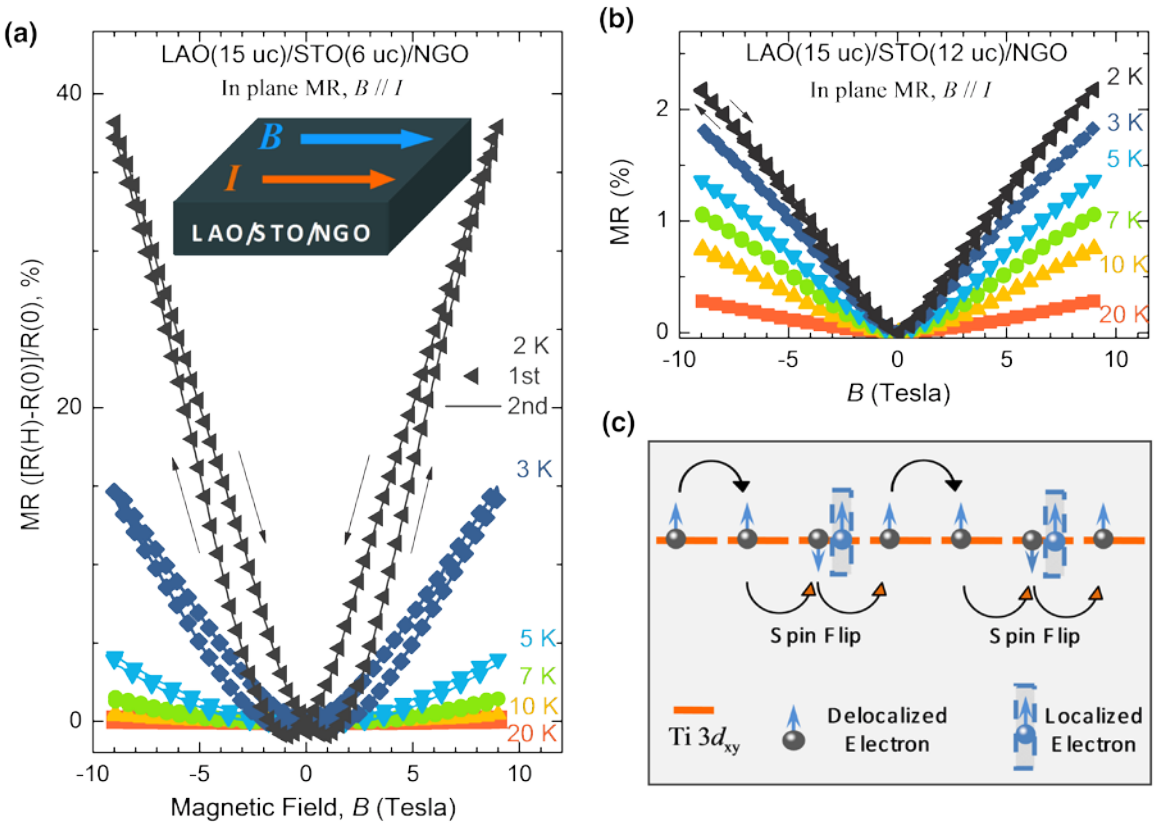

Figure 5. 11: *The in-plane MR with magnetic field B parallel to current I at different temperatures is shown for the transplanted interfaces with 6 uc STO in (a), and 12 uc STO*

in (b). (c) The sketch for spin flips during electron transport in the 6 uc sample, in which a strong localization of 2DEG is observed.

5.4 Conclusions

In this chapter, an EPS state at the LAO/STO interface prepared at high P_{O2}, where the interface charges are separated into regions of a 2DEG, a ferromagnetic phase, which persists above room temperature, and a diamagnetic/paramagnetic phase below 60 K is presented. In detail, there is strong magnetic hysteresis loop observed by SQUID magnetometer at low temperature together with strong paramagnetic response. And in high temperature, there is room temperature ferromagnetism observed, which is very significant for future device application. A hypothesis on the origin of the EPS is proposed based on the selective occupancy of interface sub-bands of the nearly degenerate Ti orbital in the STO. Moreover, the MR hysteresis loop evolution for LAO/STO/NGO samples with different STO layers thickness proved our hypothesis. The observation of EPS in this system opens up yet another exciting correlated electron system for scientific studies. Besides revealing new phenomena in physics, these unusual magnetic properties may be of use in the fabrication of novel magneto-electronic and tunable magneto-optic devices.

Chapter 6 Coexistence of Three-Dimensional Fermi Electron Liquid and Two-Dimensional electron gas in $La_{0.5}Sr_{0.5}TiO_3$ / $SrTiO_3$ Heterostructures

6.1 Introduction

Variants of oxide interfaces of LAO/STO have been studied intensely over the last decade as they show a 2DEG at the interface which exhibits a number of fascinating properties, such as critical thickness [10], 2D superconductivity [48], magnetism [11] and multi-type carriers [76, 98, 99]. Instead of crystalline LAO, other crystalline overlayers such as LTO [8] and $LaVO_3$ [100] and noncrystalline overlayers such as LAO [101] and ZrO_2:Y_2O_3 [39] have been shown to be able to produce the 2DEG on the STO substrate. To sum up, the essential underlying factor is that at these interfaces Ti in the STO substrate has two possible valence states, namely Ti^{3+} and Ti^{4+}, which lead to these interesting properties. The Ti in LSTO also exhibits these two valence states due to 50% La doping. Hence heterostructures with LSTO would be interesting systems to study.

LSTO is known as a metallic Fermi electron liquid system for several decades [102]. The parent compounds of LSTO are the band insulator STO and the Mott insulator LTO. When La substitutes Sr, LSTO evolves to an electron-doped conductor with a Fermi liquid behavior. Due to the complexity of the LSTO/STO system, such as Coulomb interactions, dual valences of Ti and structural phase transitions in LSTO and STO, new electronic phases are expected at the LSTO/STO interface.

In this chapter, LSTO thin films of various thicknesses were grown layer-by-layer by pulsed laser deposition on different substrates. For the first time, the co-existence of both a 3D

Fermi electron liquid and a 2DEG was found in films of LSTO grown on STO. The two conducting channel model was verified by the observed nonlinear HR and by fitting its dependence on film thickness, temperature and back gate voltage. Similar to the 2DEG at the LAO/STO interface, the observed 2DEG also shows a Rashba-like effect at low temperatures [52]. In contrast to the expected metallic nature of LSTO, an abrupt transition from a metallic to a highly insulating state was observed when the thickness of the LSTO thin films is reduced from 6 to 5 uc. This transition is characterized by a large conductance jump of more than six orders of magnitude. The resistance of the conducting LSTO samples shows a quadratic temperature dependence indicating that the dominant scattering mechanism is the electron-electron scattering. The strong electron-electron scattering proves the presence of Fermi liquid behavior in LSTO samples. Although the abrupt metal-insulator transition with the absence of an intermediate semiconducting state can be attributed to different mechanisms such as band bending, strain or dimensionality evolution, here we studied only the effect of strain on this transition. The results suggest a novel conducting system with potentially new physics and possible applications.

6.2 Experimental Procedures

Epitaxial LSTO films were grown on TiO_2-terminated (001) STO single-crystal substrates by PLD. The polycrystalline LSTO target used for the depositions was prepared from high purity La_2O_3 (99.999%), TiO_2 (99.999%) and SrO (99.9%) powders. The powders were carefully weighed, mixed and ground for one hour before being sintered at 600 °C for 8 hours and sintered again at 900 °C for 10 hour. Subsequently, the powders were pressed into pellets and calcinated at 1300 °C for 36 hours. During deposition of LSTO, the laser energy density was maintained at 1.6 J/cm^2 with a pulse frequency of 1 Hz. The temperature

on the samples was realized by a thermal radiation heater and was set at 850 °C during deposition and the pressure was fixed at 10^{-4} mbar during the whole process including warming, deposition and cooling. The layer-by-layer growth was monitored by *in-situ* RHEED (Fig. 6.1a). After growth, samples were cooled to room temperature with a ramping rate of 30 °C per minute.

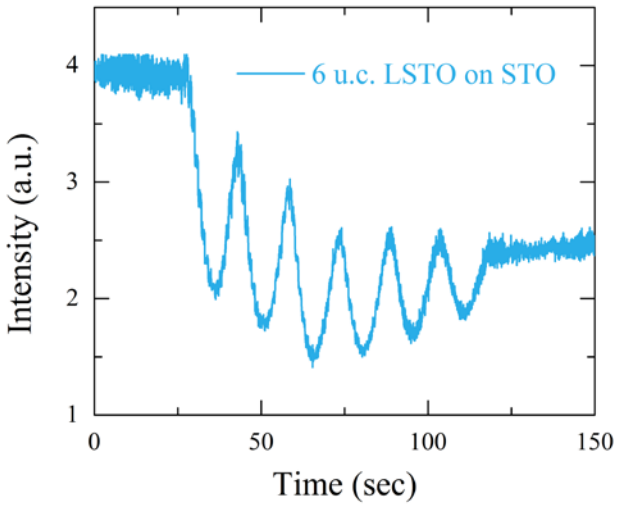

Figure 6. 1: *RHEED oscillations for an 6 uc LSTO growth on STO substrate.*

After sample growth, detailed quality investigations were done by utilizing an on-campus 3.5 million volt nuclear accelerator located at Center for Ion Beam Applications (CIBA). Information such as material composition, crystalline structure and La substitutionality were revealed by Rutherford backscattering (RBS) and Ion channeling spectrum.

The sheet resistance R_S and the carrier concentration n were obtained as a function of temperature from 300 to 2 K using a PPMS (Quantum Design Inc.) by applying a d.c. current of 1 μA. The measurement geometry was Van der Pauw geometry [66, 67] on square

shaped samples (5 x 5 mm^2) and Ohmic contacts of ultrasonically bonded Al wires to the sample corners were used.

The scanning tunneling microscopy (STM) investigation was conducted on the Omicron ultra-high vacuum room temperature STM. During scanning, 5 V was applied between the tip and the sample, which was connected to the sample holder by the bonded Al wire and the current was maintained at 0.05 nA. As changes in current are strongly influenced by the sample-to-tip distance and density of states, STM is able to reveal high resolution topography.

6.3 Results and Discussion

6.3.1 Basic Properties

In Fig. 6.2a, a typical RBS/Ion channeling spectrum on 200 uc LSTO film on STO is shown proving quantitatively the good crystal quality of the films (with a minimum yield of 2.7%) and the correct La/Sr ratio: a simulated curve of LSTO with 50% La was plotted in Fig. 6.2a which overlaps the measured curve well. Fig. 6.2b shows the sheet resistance of various thicknesses LSTO films on STO substrates. The quadratic sheet resistance versus temperature curves indicates Fermi liquid behavior [102].

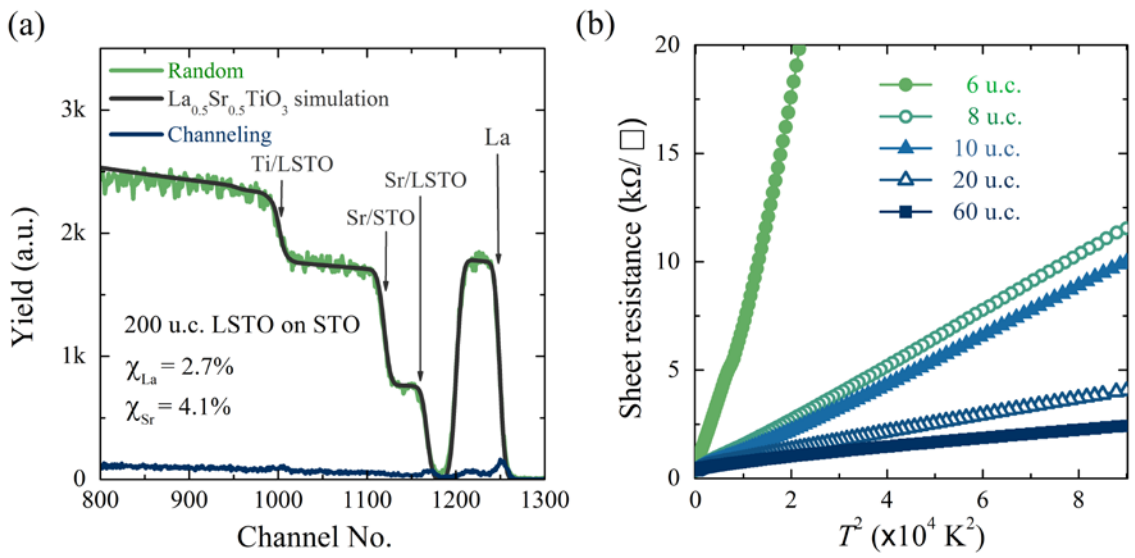

Figure 6. 2: *Rutherford channeling on 200 uc LSTO film and sheet resistance temperature dependence for various LSTO thicknesses. (a) The minimum channeling yield for La and Sr are 2.7% and 4.1% respectively indicates good substitutionality. And the measured random matches will with simulated LSTO curve proving the correct composition. (b) The quadratic relationship between resistance and temperature indicates a Fermi liquid behavior.*

6.3.2 Two Carrier Model

Interestingly, a strong nonlinear HR was observed at low temperature and under positive gate voltages.

Figure 6.3a shows an example of characterization of this nonlinear HR observed in a 60 uc thick LSTO film on STO. This nonlinear phenomenon can generally be attributed to two different mechanisms: ferromagnetism [103] or more than one type of carrier [104]. Based on other publications in similar Ti based systems, and the fact that no hysteresis loop is seen in the Hall measurements, a sophisticated two carrier model for semiconductors was applied here.

Generally, there are two equations used for the two carrier model in literature. When these two types of carriers are spatially separated in different channels, the following equation is used to describe the nonlinear HR [105]:

$$R_H = [(\mu_1^2 n_1 + \mu_2^2 n_2) + (\mu_1\mu_2 B)^2(n_1 + n_2)]/\{e[(\mu_1|n_1| + \mu_2|n_2|)^2 + (\mu_1\mu_2 B)^2(n_1 + n_2)^2]\}$$

Equation 6-1

in which $R_H = V_H/I$, n is sheet carrier density and μ is carrier mobility. When the two types of carriers are not spatially separated, another equation is used to describe the nonlinear HR [106]:

$$R_H = (B/e)[n_1\mu_1^2/(1 + \mu_1^2 B^2) + n_2\mu_2^2/(1 + \mu_2^2 B^2)]/\{[n_1\mu_1/(1 + \mu_1^2 B^2) + n_2\mu_2/(1 + \mu_2^2 B^2)]^2 + [n_1\mu_1^2 B/(1 + \mu_1^2 B^2) + n_2\mu_2^2 B/(1 + \mu_2^2 B^2)]^2\}.$$

Equation 6-2

There are four unknown variables both in Equation 6-1 and in Equation 6-2, so it is not possible to identify n and μ. An additional constraint is required to guarantee the unique value of n and μ. In our fitting,

$$R_{xx}(0) = 1/[e(n_1\mu_1 + n_2\mu_2)] \qquad \textbf{Equation 6-3}$$

was selected as constraint and fitting was conducted nicely.

To select the correct formula from above two, an essential question needs to be answered: are there one or two types of carriers in the LSTO film itself? To investigate this, the HR of 50 uc LSTO films grown on LAO substrates were compared with films grown on STO substrates. It was found that the HR are linear for the films on LAO substrates instead of the nonlinear HR for the films on STO substrates (Fig. 6.3b). This suggests there is only one type of carriers in only LSTO and that the two types of carriers observed in LSTO/STO systems are spatially separated. So the first formula was selected. The fitting accuracy based on the first formula is demonstrated in Fig. 6.3a.

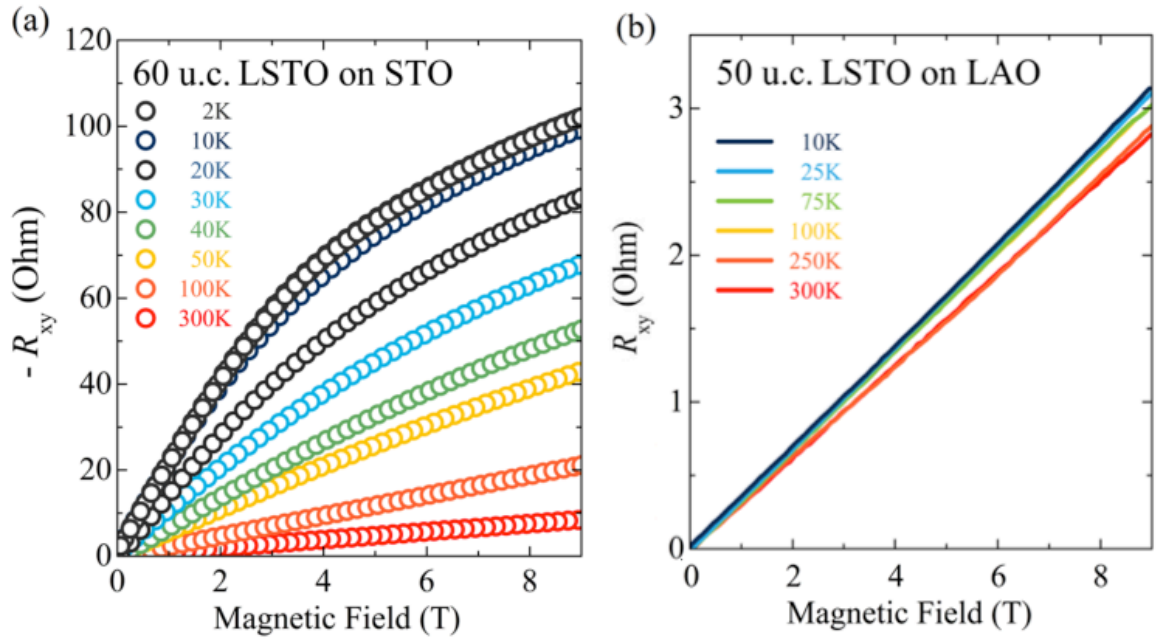

Figure 6. 3: *Nonlinear HR and linear HR in LSTO film on difference substrates. (a) Nonlinear HR for 60 uc LSTO on STO substrate at 0 V gate voltage and different. Experimental date are indicated in circles with different colors and fitted curved are plotted in lines with a single black color. (b) Linear HR for 50 uc LSTO on LAO substrate.*

6.3.3 Thickness, Temperature and Gate Voltage Dependence

A more complete set of nonlinear HR data is shown in Fig. 6.4. In Fig. 6.4a, the HR shows a clear nonlinear behaviour for LSTO films with a thickness above 8 uc and the HR goes from nonlinear to linear when the film thickness is reduced. This suggests two types of carriers in relative thick LSTO films on STO substrates. Owing to the more than an order of magnitude difference in *n*, the larger amount of carrier is assigned to be 3D and the smaller amount of carrier is assigned to be 2D. To investigate the scattering processes and origin of these two types of carriers, the temperature dependence was studied for 60 uc LSTO films and is shown in Fig. 6.4d. It is found that the nonlinear HR is only seen at temperatures lower than

100 K. Using the same equation mentioned above, n and μ at different temperatures are calculated and plotted in Fig. 6.4e and 6.4f. It is found that the n and μ of 3D carriers show opposite trends when varying the temperature. This is the typical behaviour of a Fermi liquid where dominating e-e scattering is enhanced with increasing n. The 2D carriers are only seen below 100 K and their n varies by more than an order of magnitude over the range of 100 K to 2K. However, the μ (more than an order larger than that of the 3D carriers) is independent of temperature indicating an electron gas behaviour. So we see the coexistence of a 3D Fermi liquid and a 2DEG in this system. From the thickness dependence it is clear that the 3D Fermi liquid is in the LSTO layer and the question is: where is the 2DEG, at the surface of the LSTO layer or at the LSTO/STO interface? And more specifically for the latter case: is the electron gas in the LSTO layer or the STO layer? To answer the above questions, field effect studies were conducted on 60 uc LSTO film due to the remarkable nonlinear HR. During the experiment, the STO substrate was used as back gate. The leakage current was well maintained in nA range and the source-drain current was fixed at 1 μA. The temperature was 40 K, because this is the temperature where the 2D carrier density is the most sensitive (Fig. 6.4d). With the insulating STO substrate serving as dielectric material in this capacitor structure, n is only able to be tuned by a back gate electrical field if the 2D carriers are located at the interface between the conducting LSTO film and STO substrate. Furthermore, the n will increase when a positive voltage is applied. If the 2D carriers are created by surface depletion resulting into a 2D electron channel located at the top surface of LSTO, n will not be tuneable by the back gate voltage due to the metallicity of LSTO. According to our observation in Fig 6.4g, nonlinear HR is indeed tuneable by the back gate voltage. The only obvious increase of the 2D carrier density happens by increasing the back gate voltage. Therefore, the 2D channel is confirmed to be at the interface between STO and LSTO with a non-Fermi liquid behaviour, as the mobility increases when n increases.

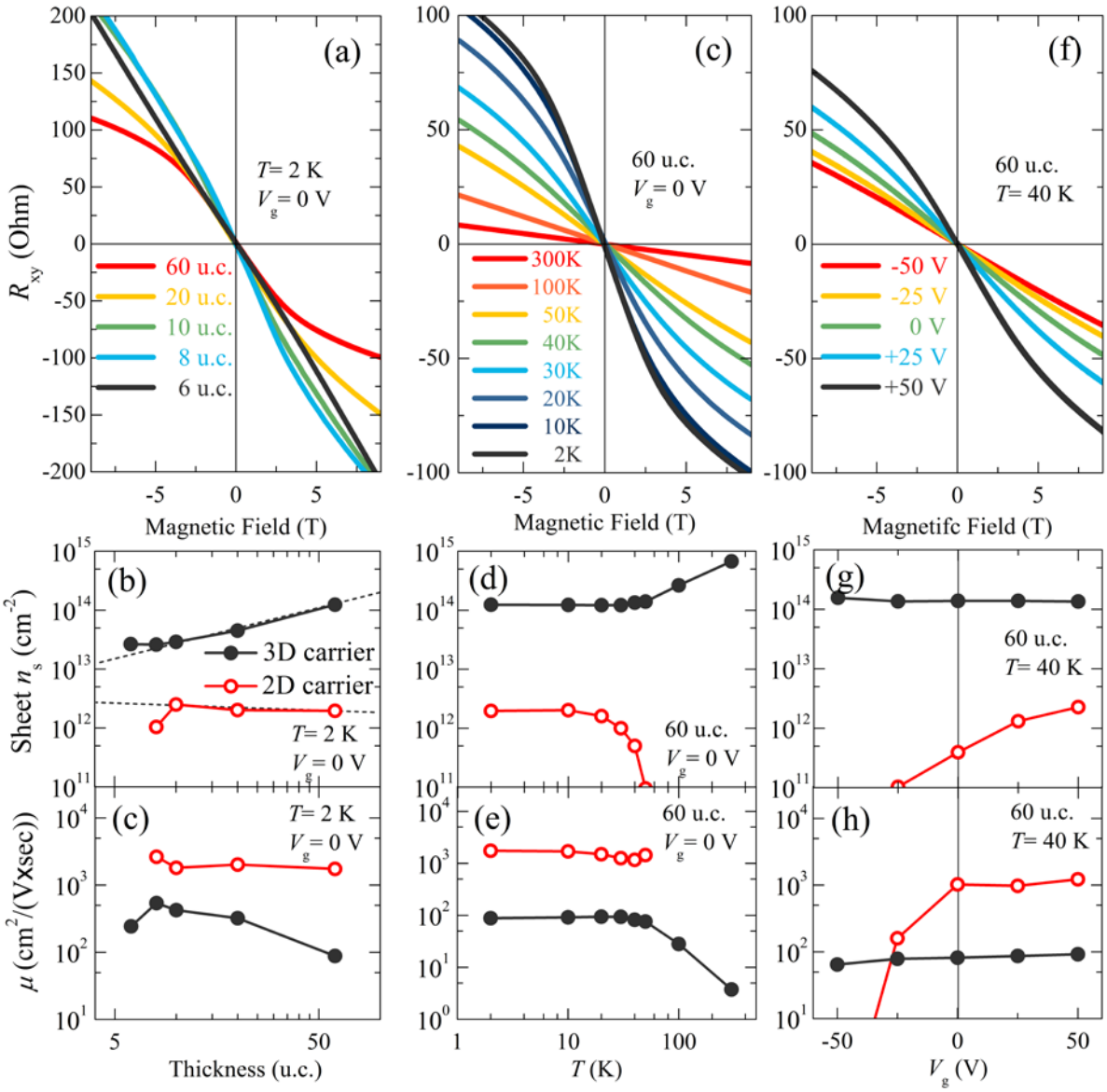

Figure 6. 4: *Nonlinear Hall effect in LSTO films. Nonlinear Hall effect for 60 uc LSTO under different temperatures T (a) and back gate voltages V_g (b). (c) Nonlinear Hall effect for various LSTO film at 2 K. Density changes of two types of carriers in 60 uc LSTO film under influence of temperature T (d) and back gate voltages V_g (e). (f) Density changes of two types of carriers at 2 K in various thicknesses LSTO films. Mobility changes of two types of carriers in 60 uc LSTO film under influence of temperature T (g) and back gate voltages V_g (h). (i) Mobility changes of two types of carriers at 2 K in various thicknesses LSTO films.*

To sum up the nonlinear HR results, we found there is a bulk 3D Fermi liquid in LSTO film and a low n and high μ 2DEG at the interface between the LSTO film and STO substrate.

6.3.4 Features of Electron Gas

The resistance and MR response under applying an electrical field at 2 K were also studied to reveal the features of the observed 2DEG. For the 60 uc LSTO film, the sheet resistances corresponding to the 2D carriers and 3D carriers under applying an electrical field, are calculated using the equation of $R = 1/(en\mu)$ and the n and μ values shown in Fig. 6.4g and 6.4h. The determined values are plotted in Fig. 6.5a. Experimentally shown in Fig. 6.5b, the measured modulations on sheet resistances match well with calculated sheet resistances. The stronger tuning effect observed for the 6 uc LSTO film on STO matches the 2D carrier behavior in Fig. 6.5a, while the weaker tuning effect in the thicker LSTO films on STO is similar to the 3D carrier behavior. These similarities further prove the dimensionality of the LSTO films. More interestingly, a Rashba-like effect, previously observed in the 2DEG at the LAO/STO interface [52], was also observed in 6 uc LSTO on STO. Although the resistance versus temperature curve for 6 uc LSTO on STO shows Fermi liquid behavior (Fig. 6.1b), our result indicates the interfacial 2DEG plays an important role in the thin LSTO film on STO and it can even be considered as 2DEG.

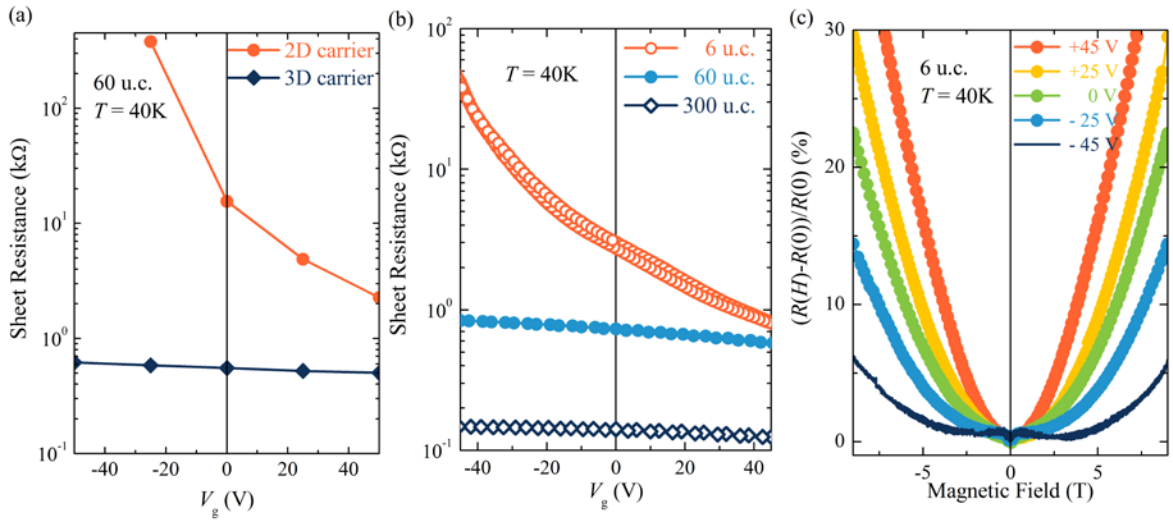

Figure 6. 5: *Back gate tuning effect on linear resistance and MR. (a) Behaviors of 2D and 3D carrier extrapolated from Fig. 6.4g and 6.4h. (b) Back gate voltage tuning effect on linear resistance of different thickness LSTO films at 2 K. (c) MR of 6 uc sample under different back gate electrical field. The sample shows Rashba-effect like behavior under negative back gate electric field.*

6.3.5 Conductivity Critical Thickness

According to the previous data, there are two types of carriers observed in LSTO/STO systems and the conductivity increases by reducing the LSTO thickness. Therefore, a natural question is triggered whether it is possible for the charge carriers in LSTO to exist in a confined 2D system? To examine this question, LSTO films were grown on STO substrate with a systematic thickness change. It was found the LSTO film with thickness smaller than 6 uc grown has a resistance larger than the measurement limit. The metallic behavior of 6 uc LSTO films on STO substrate varies from sample to sample and it can even become insulating after several cycles of resistance versus temperature transport measurements. Although the 6 uc LSTO film is not stable, the abrupt transition from conducting to insulating without a semiconducting intermediate state is still interesting. In fact, this

thickness dependent metal-insulator transition (MIT) is similar to the critical thickness phenomena observed in LAO/STO. To summarize the transport data, the measured conductivity versus thickness relation is plotted in Fig. 6.6a. Note that the conductivity was normalized by excluding the 6 uc insulating region. To illustrate the observed regions, the observed electrical properties are plotted in real space in Fig. 6.6b.

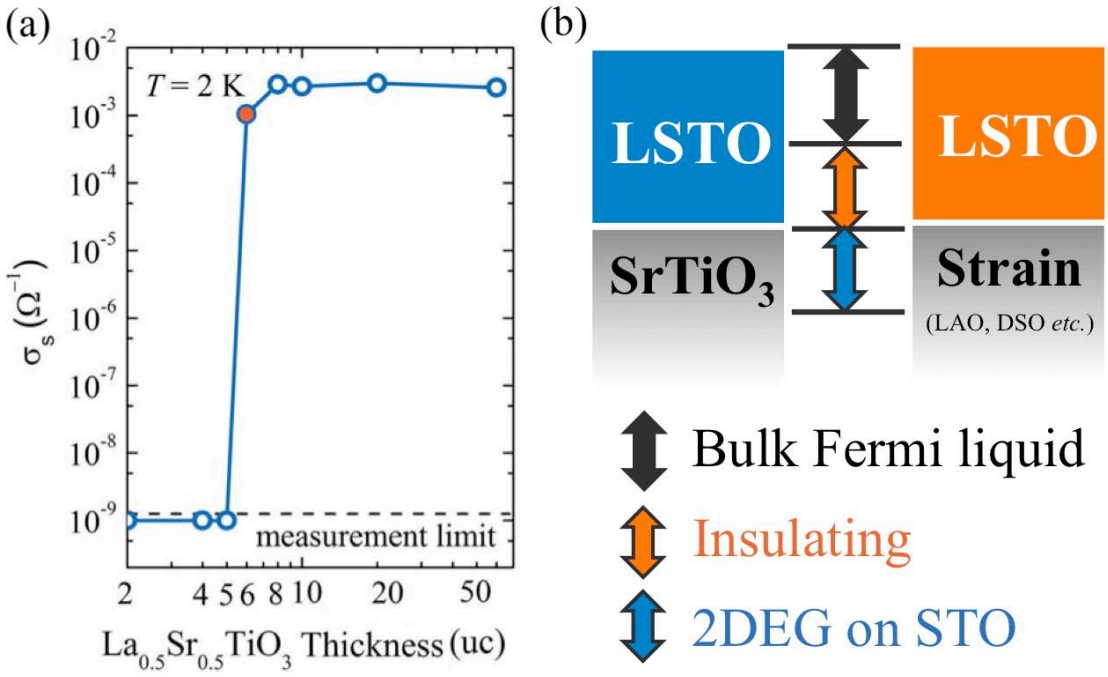

Figure 6. 6: *Abrupt MIT and sketch of observed regions in LSTO sytems. (a) 5 to 6 uc critical thickness for LSTO on STO with conductance changes of more than 6 orders of magnitude at 2K. The orange dot at 6 uc indicates the instability of the conductance. Samples with an LSTO thickness of 6 uc show either metallic or highly insulating, never an intermediate semiconducting phase. (b) Schematic drawing of observed regions in LSTO/STO system and LSTO/LAO system.*

The thickness dependent MIT has been found in many oxides. For example, $LaNiO_3$ [107] and $SrVO_3$ [108] as overlayers were shown to be insulating when the film thickness is reduced to 2 to 3 uc, although their bulk properties are conducting. However, the observed critical thickness for MIT in LSTO system is more similar to the critical thickness at

LAO/STO interfaces, because they both have no semiconducting intermediate state observed within the MIT.

There are several possible explanations for the critical thickness dependence. It can be conducting phase percolation, strain induced MIT, thickness dependent band structure, interface bandbending and also other possible mechanisms. So far, we have only investigated the first two mechanisms.

6.3.6 Conductance Uniformity

While LSTO is a conducting material, it is interesting that the LSTO film becomes insulating abruptly when the thickness crosses 6 uc. The abrupt transition from metal to insulator with more than 6 orders change of conductance might indicate a first order transition, such as phase separation phenomenon that is similar to the manganite. First order transitions are crucial for phase separation phenomena. The state with the lowest energy is itself phase separated due to the influence of small amounts of disorder [109]. The idea is that the effects of minute amounts of disorder on a first order phase transition can cause a drastic change in the state, creating actually an inhomogeneous state due to the importance of disorder. This effect in 2D is much stronger than that in 3D, maybe because the amount of disorder is amplified and a first order transition could easily become phase separation. If the phase separation, which contains insulating islands, was the origin of the insulating behavior for films below 6 uc, a STM should be able to resolve the insulating islands.

To study the conductance homogeneity, STM was employed to scan the 7 uc LSTO film on STO substrate. Figure 6.7 shows two typical images with different field of views. During the scan, a fixed current of 0.05 nA and voltage of 5 V was applied between the STM tip and

sample. To maintain the current and voltage, the tip has to adjust the height if the material is inhomogeneous in conductance. Therefore, the sample topography would directly demonstrate the homogeneity. As can be seen in Fig. 6.7a, the 1um field of view shows only the terraces of films, no insulating islands are observed where very high spots should be observed. Even after zoom in Fig. 6.7b, there is no obvious high spot observed with roughness less than 1 uc. This is a direct proof of conductance homogeneity. Furthermore, it could even indicate the conducting layer is only 1 uc in thickness.

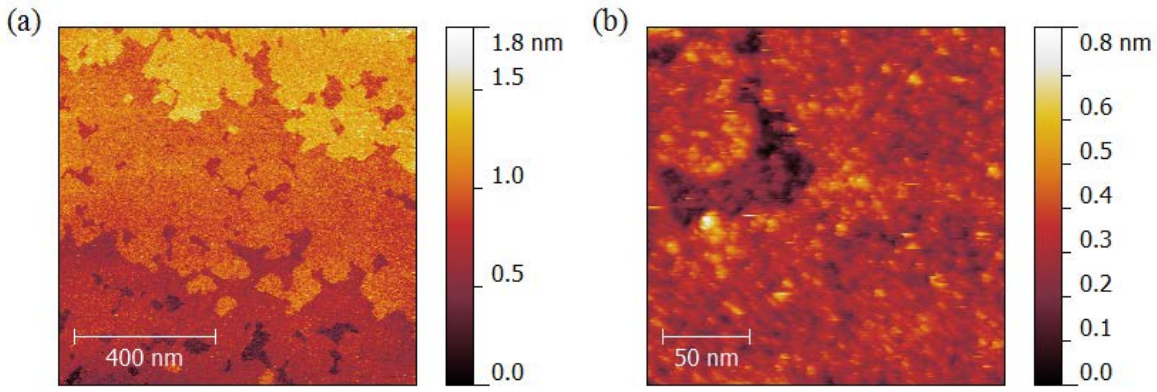

Figure 6. 7: *Room temperature Scanning Tunneling Microscopy images on 7 uc LSTO on STO substrate with I = 0.05 nA and V = 5 V. Images with (a) 1 um field of view and (b) 200 nm field of views.*

6.3.7 Strain Effect

The metallic behavior or dead layer of LSTO can also be tuned by strain. To study the strain effect, a 15 uc thick LSTO film, which has a lattice constant around 3.91 Å [37], was grown on different substrates with different lattice constants. For the chosen substrates, the lattice constants [44] are 3.791 Å for LAO, 3.868 Å for LSAT [37], 3.859 Å for NGO [110], 3.905 Å for STO and 3.944 Å for $DyScO_3$ (110) [111].

Figure 6.8 shows a summary of the strain effect on LSTO including the AFM topography and the corresponding transport properties. As can be seen in the AFM images, surface roughnesses are all round 1 uc with some substrates showing clear steps. Comparing the transport data, it was found that tensile strain introduced by $DyScO_3$ substrates switches the behavior of the 15 uc LSTO film from conducting to insulating. The minimum compressive strain provided by STO causes the best conducting behavior in LSTO. As the compressive strain becomes stronger from STO, LSAT, NGO to LAO, the quality of the conductivity decreases progressively. In the 15 uc LSTO film example, the material can be tuned to an insulator by large compressive strain. Comparing with LSAT and NGO, the stronger compressive strain induced by the NGO substrate causes a complete semiconducting behavior in LSTO and the weaker compressive strain from LSAT causes only localization at low temperatures.

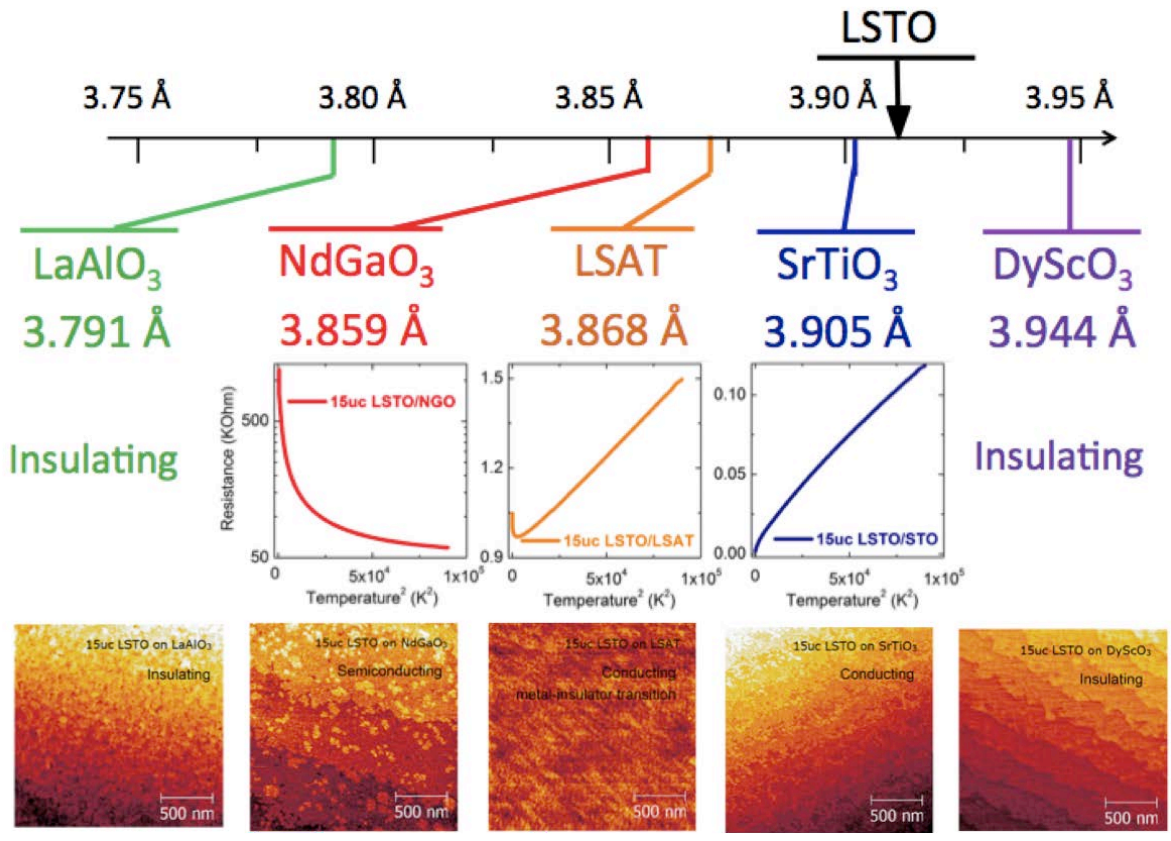

Figure 6. 8: *Strain influence and AFM topography data on 15 uc LSTO on different substrates. Roughness are confirmed below 1 uc with some samples showing clear atomically flat steps. With compressive strain increasing, the conductivity evolved from conducting to localication at low temperature to semiconducting and to even insulating. For the tensile strain induced by $DyScO_3$, it switched LSTO from conducting to insulating.*

As the ultrathin LSTO film is very sensitive to strain, we conclude that the strain effect is a very possible reason for the critical thickness phenomenon observed in LSTO films. As the LSTO has to be grown on a substrate to get a confined 2D system, the critical thickness phenomenon can be observed due to the influences provided by the lattice mismatch.

6.4 Conclusions

In summary, two types of coexisting carriers characterized by nonlinear Hall effect were observed in LSTO films on STO substrates: a 3D Fermi liquid in the LSTO film and a 2DEG at the interface between LSTO and STO. Interestingly, these two types of carriers have remarkable differences in their electric field and temperature response. By reducing the LSTO film thickness, an abrupt metal-insulator transition was observed in LSTO grown on STO. The transition is abrupt as the transition width is less than 2 uc and there is no semiconducting intermediate state. To investigate the conductance uniformity, surface conductance was investigated on 7 uc thick LSTO films on STO by employing STM and it was found there is no conductance inhomogeneity. This result suggests that the conducting layer could be as thin as one uc and there is an insulating layer of around 5 uc. To investigate the insulating layer properties, 15 uc LSTO were grown on substrates with different lattice constants. We observed that the tensile strain introduced by $DyScO_3$ (110) is able to switch metallic LSTO to the insulating state. For compressive strain, with increasing strain the conductance is progressively destroyed. The largest compressive strain introduced

by LAO is able to switch 15 uc LSTO from the conducting to insulating state as well. This result indicates that the effect of strain is of great importance in fabricating conducting LSTO films. Finally, these results on the coexistence of the 2DEG and 3D Fermi liquid can shed light on the mechanism of 2DEG at the LAO/STO interface and the mechanism of possible reconstructions at complex oxide interfaces.

Chapter 7 Summary and Future Research

7.1 Summary

7.1.1 Optical Properties of LAO/STO Interface

A detailed defect energy level map was investigated for heterostructures of 26 uc of LAO on STO prepared at a low P_{O2} of 10^{-6} mbar. The origin is attributed to the presence of dominating oxygen defects in the STO substrate. Using femtosecond laser spectroscopy, the transient absorption and relaxation times for various transitions were determined. An ultrafast relaxation process of 2–3 ps from the conduction band to the closest defect level and a slower process of 70–92 ps from conduction band to intraband defect level were observed. The results are discussed on the basis of the proposed defect-band diagram.

7.1.2 Electrical Properties of LAO/STO Interface

Magnetoresistance anisotropy in LAO/STO interfaces is compared between samples prepared in high P_{O2} of 10^{-4} mbar exhibiting 2DEG and low P_{O2} of 10^{-6} mbar exhibiting 3D conductivity. While MR of an order of magnitude larger was observed in low P_{O2} samples compared to those of high P_{O2} samples, large MR anisotropies were observed in both cases. The MR with the out-of-plane field is always larger compared to the MR with in-plane field, suggesting lower dissipation of electrons from interface versus defect scattering. The 2D interfaces show a negative MR at low temperatures while the 3D interfaces show positive MR for all temperatures. Furthermore, the angle relationship of the MR anisotropy for these two types of samples different cases and temperature dependence of the in-plane MR are also presented. Our study demonstrates that MR can be used to distinguish the dimensionality of

the charge transport and various (defect, magnetic center, and interface boundary) scattering processes in this system.

7.1.3 Magnetic Properties of LAO/STO Interface

A variety of new and unusual electronic phases at interfaces between complex oxides, in particular between the non-magnetic insulators LAO and STO, have stimulated the oxide community. However, no EPS has been observed in this system despite a theoretical prediction. In this thesis, we reported an EPS state at the LAO/STO interface, where the interface charges are separated into regions of a 2DEG, a ferromagnetic phase, which persists above room temperature, and a (superconductor like) diamagnetic/paramagnetic phase below 60 K. The EPS is due to the selective occupancy (in the form of 2D-nanoscopic metallic droplets) of interface sub-bands of the nearly degenerate Ti orbital in the STO. The observation of this EPS demonstrates the electronic and magnetic phenomena that can emerge at the interface between complex oxides mediated by the Ti orbital.

7.1.4 Two Types of Carriers in LSTO Film

Variants of oxide interfaces of LAO/STO have been studied intensely over the last decade as they show a 2DEG at the interface that exhibits a number of fascinating properties. In this thesis we showed that LSTO thin films of various thicknesses grown on STO substrates show both a 3D Fermi electron liquid and a 2DEG. This two channel conducting model was verified by the observed nonlinear HR and by fitting its dependence on film thickness, temperature and back gate. The thickness dependence and strain dependence of LSTO thin film were also investigated. Interestingly, LSTO on STO is found to be an insulator when the thickness is below 6 uc, although the bulk material is a conductor. The intriguing metal

to insulator transition is interesting as the transition width is less than 2 uc and there is no semiconducting intermediate state. By using STM, surface conductance is confirmed to be uniform and the thickness of the conducting layer could be only one to two uc. To investigate the strain effect, 15 uc LSTO were grown on five types of substrates with different lattice constants. It was found that the tensile strain is able to cause the insulating state. The compressive strain is able to cause insulating state as well, but with weaker capability. The study on LSTO could help on understanding LAO/STO interface and even some basic fundamental issues in complex oxides and their interfaces.

7.2 Future Research

Atomically flat interfaces and heterostructures, in particular LAO/STO interfaces and LSTO ultrathin films, content rich physics and have potential for technical applications. To investigate the physics behind and accelerate the application process, the following projects seem important:

1. One dimensional electron gas

With help of lithography, a one dimensional electron gas based on LAO/STO could be achieved. Following the same scenario where novel functions are observed when the electron gas is confined into a two dimensional interface between LAO and STO, new properties are expected when the dimension evolves from two dimension to one dimension. For instance, the quantum resistance could be the first very possible observation, as the channel dimension is reduced smaller than the electron mean free path.

2. Interface Junctions

The 2DEG at LAO/STO interfaces has already exhibited novel properties. How about making a junction between this 2DEG and other system, *e.g.* superconductor, p-type oxide, ferromagnetic electrodes? The combination possibility is numerous and functions to be explored are promising.

3. Angle-resolved photoemission spectroscopy (APRES) on LSTO

How does the electronic band structure evolve in the LSTO during the abrupt metal-insulator transition? Experimentally, APRES on *in-situ* grown film surfaces is the best way to discover the band structure evolution. This direct observation on the band structure could introduce a completely new area for oxide research.

4. Critical thickness for different LSTO concentration

In this thesis, critical thickness of metal-insulator-transition was only studied for 50% La substituted STO. Does the critical thickness have La concentration dependence? If dependences would be found and the critical thickness is smaller for higher La concentration, this could be a very interesting evidence of charge injection from polar LTO to STO. This would also be the first system with a polarization catastrophe existing in a conducting material.

BIBLIOGRAPHY

[1] G. E. Moore, “Cramming more components onto integrated circuits,” *Electronics*, 38, 114 (1965).

[2] http://en.wikipedia.org/wiki/Moore’s_law.

[3] R. Waser and M. Aono, “Nanoionics-based resistive switching memories,” *Nature Materials*, 6, 833-840 (2007).

[4] M. K. Wu *et al*., “Superconductivity at 93K in a new mixed-phase Y-Ba-Cu-O compund system at ambient pressure,” *Physical Review Letters*, 58, 908-910 (1987).

[5] S. Jin, T. H. Tiefel, M. Mccormack, R. A. Fastnacht, R. Ramesh, and L. H. Chen, “Thousandfold change in resistivity magnetoresistive La-Ca-Mn-O films,” *Science*, 264, 413-415 (1994).

[6] C. H. Ahn, J.-M. Triscone, and J. Mannhart, “Electric field effect in correlated oxide systems,” *Nature*, 424, 1015-1018 (2003).

[7] K. J. Choi *et al*., “Enhancement of ferroelectricity in strained $BaTiO_3$ thin films.,” *Science*, 306, 1005-1009 (2004).

[8] A. Ohtomo, D. A. Muller, J. L. Grazul, and H. Y. Hwang, “Artificial charge-modulationin atomic-scale perovskite titanate superlattices,” *Nature*, 419, 378-380 (2002).

[9] A. Ohtomo and H. Y. Hwang, “A high-mobility electron gas at the $LaAlO_3/SrTiO_3$ heterointerface,” *Nature*, 427, 423-426 (2004).

[10] S. Thiel, G. Hammerl, A. Schmehl, C. W. Schneider, and J. Mannhart, “Tunable quasi-two-dimensional electron gases in oxide heterostructures,” *Science*, 313, 1942-1945 (2006).

[11] A. Brinkman, M. Huijben, M. V. Zalk, J. Huijben, U. Zeitler, and J. C. Maan, “Magnetic effects at the interface between nonmagnetic oxides,” *Nature Materials*, 6, 493-496 (2007).

[12] A. D. Caviglia *et al*., “Electric field control of the $LaAlO_3/SrTiO_3$ interface ground state,” *Nature*, 456, 624-627 (2008).

[13] C. Cen *et al*., “Nanoscale control of an interfacial metal-insulator transition at room temperature,” *Nature Materials*, 7, 298-302 (2008).

[14] http://en.wikipedia.org/wiki/Perovskite_(structure).

[15] H. Y. Hwang, Y. Iwasa, M. Kawasaki, B. Keimer, N. Nagaosa, and Y. Tokura, “Emergent phenomena at oxide interfaces,” *Nature Materials*, 11, 103-113 (2012).

[16] J. Chakhalian, A. J. Millis, and J. Rondinelli, "Whither the oxide interface," *Nature Materials*, 11, 92-94 (2012).

[17] M. Fujimoto, Y.-M. Chiang, A. Roshko, and W. D. Kingery, "Microstructure and electrical properties of Sodium-diffused and Potassium-diffused $SrTiO_3$ barrier-layer capacitors exhibiting varistor behavior," *J. Am. Ceram. Soc*, 68, 11 (1985).

[18] J. Gerblinger and H. Meixner, "Fast oxygen sensors based on sputtered strontium titanate," *Sensors and Actuators B: Chemical*, 4, 99-102 (1991).

[19] M. Kawai, S. Watanabe, and T. Hanada, "Molecular beam epitaxy of $Bi_2Sr_2CuO_X$ and $Bi_2Sr_2Ca_{0.85}Sr_{0.15}Cu_2O_X$ ultra thin films at 300 C," *Journal of Crystal Growth*, 112, 745-752 (1991).

[20] F. W. Lytle, "X-Ray diffractometry of low-temperature phase transformations in strontium titanate," *Journal of Applied Physics*, 35, 2212-2215 (1964).

[21] E. Tosatti and R. Martonak, "Rotational melting in displacive quantum paraelectrics," *Solid Sate Communications*, 92, 167-180 (1994).

[22] S. K. Mishra and D. Pandey, "Low temperature x-ray diffraction study of the phase transitions in $Sr_{1-X}Ca_XTiO_3$ (x = 0.02, 0.04): evidence for ferrielectric ordering," *Applied Physics Letters*, 95, 232910 (2009).

[23] W. S. Baer, "Free-carrier absorption in reduced $SrTiO_3$," *Physical Review*, 144, 734-738 (1966).

[24] H. Yamada and G. R. Miller, "Point defects in reduced strontium titanate," *Journal of Solid State Chemistry*, 6, 169-177 (1973).

[25] R. L. Wild, E. M. Rockar, and J. C. Smith, "Thermochromism and electrical conductivity in doped $SrTiO_3$," *Physical Review B*, 8, 3828-3835 (1973).

[26] C. Lee, J. Destry, and J. L. Brebner, "Optical absorption and transport in semiconducting $SrTiO_3$," *Physical Review B*, 11, 2299-2310 (1975).

[27] D. Kan *et al*., "Blue-light emission at room temperature from Ar^+-irradiated $SrTiO_3$," *Nature Materials*, 4, 816-819, (2005).

[28] S. Mochizuki, F. Fujishiro and S. Minami, "Photoluminescence and reversible photo-induced spectral change of $SrTiO_3$," *J. Phys.: Condens. Matter*, 17, 923-948 (2005).

[29] A. Lotnyk, S. Senz, and D. Hesse, "Epitaxial growth of TiO_2 thin films on $SrTiO_3$, $LaAlO_3$ and yttria-stabilized zirconia substrates by electron beam evaporation," *Thin Solid Films*, 515, 3439-3447 (2007).

[30] J. Chrosch and E. K. H. Salje, “Temperature dependence of the domain wall width in $LaAlO_3$,” *Journal of Applied Physics*, 85, 722-727 (1999).

[31] S. A. Hayward, S. A. T. Redfern, and E. K. H. Salje, “Order parameter saturation in $LaAlO_3$,” *Journal of Physics: Condensed Matter*, 14, 10131-10144 (2002).

[32] Y. Okimoto, T. Katsufuji, Y. Okada, T. Arima, and Y. Tokura, “Optical spectra in $(La,Y)TiO_3$: variation of Mott-Hubbard gap features with change of electron correlation and band filling,” *Physical Review B*, 51, 9581-9588 (1995).

[33] K. H. Kim *et al*., “Epitaxial structure and transport in $LaTiO_{3+X}$ films on (001) $SrTiO_3$,” *Physica Status Solidi (a)*, 200, 346-351 (2003).

[34] K. Yoshii, A. Nakamura, and H. Abe, “Magnetic study of the mixed orthotitanate $La_{1-X}Sm_XTiO_3$ (0<=x<=1),” *Journal of Alloys and Compounds*, 290, 236-243 (1999).

[35] H. Y. Hwang, “Atomic control of the electronic structure at heterointerfaces,” *MRS Bulletin*, 31, 28-35 (2006).

[36] J. Hemberger *et al*., “Evidence for Jahn-Teller distortions at the antiferromagnetic transition in $LaTiO_3$,” *Physical Review Letters*, 91, 066403 (2003).

[37] J. E. Sunstron IV, S. M. Kauzlarich, and P. Klavinst, “Synthesis, structure, and properties of $La_{1-X}Sr_XTiO_3$(0<= x<=1),” *Chem. Mater.*, 4, 346-353 (1992).

[38] J. Chakhalian *et al*., “Orbital reconstruction and covalent bonding at an oxide interface,” *Science*, 318, 1114-1117 (2007).

[39] J. Garcia-Barriocanal *et al*., “Colossal ionic conductivity at interfaces of epitaxial ZrO_2:Y_2O_3/$SrTiO_3$ heterostructures,” *Science*, 321, 676-680 (2008).

[40] A. Gozar *et al*., “High-temperature interface superconductivity between metallic and insulating copper oxides,” *Nature*, 455, 782-785 (2008).

[41] D. D. Fong *et al*., “Ferroelectricity in ultrathin perovskite films,” *Science*, 304, 1650-1653 (2004).

[42] N. Nakagawa, H. Y. Hwang, and D. A. Muller, “Why some interfaces cannot be sharp,” *Nature Materials*, 5, 204-209 (2006).

[43] A. Kalabukhov, R. Gunnarsson, E. Olsson, T. Claeson, and D. Winkler, “Effect of oxygen vacancies in the $SrTiO_3$ substrate on the electrical properties of the $LaAlO_3$/$SrTiO_3$ interface,” *Physical Review B*, 75, 121404(R) (2007).

[44] C. W. Bark *et al*., “Tailoring a two-dimensional electron gas at the $LaAlO_3$/$SrTiO_3$ (001) interface by epitaxial strain,” *Proceedings of the National Academy of Sciences*, 108, 4720-4724, (2011).

[45] Ariando *et al*., "Electronic phase separation at the $LaAlO_3/SrTiO_3$ interface," *Nature Communications*, 2, 188, (2011).

[46] T. Higuchi and H. Y. Hwang, "General considerations of the electrostatic boundary conditions in oxide heterostructures," *arXiv:1105.5779v1 [cond-mat.mes-hall]*.

[47] P. Willmott *et al*., "Structural basis for the conducting interface between $LaAlO_3$ and $SrTiO_3$," *Physical Review Letters*, 99, 155502 (2007).

[48] N. Reyren *et al*., "Superconducting interfaces between insulating oxides," *Science*, 317, 1196-1199 (2007).

[49] D. A. Dikin, M. Mehta, C. W. Bark, C. M. Folkman, C. B. Eom, and V. Chandrasekhar, "Coexistence of superconductivity and ferromagnetism in two dimensions," *Physical Review Letters*, 107, 056802 (2011).

[50] J. A. Bert *et al*., "Direct imaging of the coexistence of ferromagnetism and superconductivity at the $LaAlO_3/SrTiO_3$ interface," *Nature Physics*, 7, 767-771 (2011).

[51] L. Li, C. Richter, J. Mannhart, and R. C. Ashoori, "Coexistence of magnetic order and two-dimensional superconductivity at $LaAlO_3/SrTiO_3$ interfaces," *Nature Physics*, 7, 762-766 (2011).

[52] A. D. Caviglia, M. Gabay, S. Gariglio, N. Reyren, C. Cancellieri, and J.-M. Triscone, "Tunable Rashba spin-orbit interaction at oxide interfaces," *Physical Review Letters*, 104, 126803 (2010).

[53] J. W. Park *et al*., "Creation of a two-dimensional electron gas at an oxide interface on silicon," *Nature Communications*, 1, 94 (2010).

[54] C. W. Schneider, S. Thiel, G. Hammerl, C. Richter, and J. Mannhart, "Microlithography of electron gases formed at interfaces in oxide heterostructures," *Applied Physics Letters*, 89, 122101 (2006).

[55] G. Cheng *et al*., "Sketched oxide single-electron transistor.," *Nature Nanotechnology*, 6, 343-347 (2011).

[56] M. Kawasaki *et al*., "Atomic control of the $SrTiO_3$ crystal surface," *Science*, 266, 1540-1542 (1994).

[57] G. Koster, B. L. Kropman, G. J. H. M. Rijnders, D. H. A. Blank, and H. Rogalla, "Quasi-ideal strontium titanate crystal surfaces through formation of strontium hydroxide," *Applied Physics Letters*, 73, 2920-2922 (1998).

[58] http://en.wikipedia.org/wiki/Atomic_force_microscopy.

[59] D. Dijkkamp *et al*., "Preparation of Y-Ba-Cu oxide superconductor thin films using pulsed laser evaporation from high Tc bulk material," *Applied Physics Letters*, 51, 619-621 (1987).

[60] M. Prutton, "Introduction to surface physics," Clarendon (1994).

[61] F.C. Frank and J.H. van der Merwe, "One-Dimensional dislocations," *I. Static Theory. Proc. Roy. Soc. London A*, 198, 205 (1949).

[62] M. Volmer and A. Weber, "Nucleus formation in supersaturated systems," *Z. Phys. Chem.* 119, 277, (1926).

[63] I.N. Stranski and Krastanov. "Theory of orientation separation of ionic crystals," *Acad. Wiss. Math. Naturw. Klasse IIb*, 146, 797 (1938).

[64] Auciello. O., Krauss. A.R.. "In situ real-time characterisation of thin film," John Wiley & Sons, Inc. (2001).

[65] E. E. Fullerton, I. K. Schuller, H. Vanderstraeten, and Y. Bruynseraede, "Structural refinement of superlattices from X-ray diffraction," *Physical Review B*, 45, 9292-9310 (1992).

[66] L. J. van der Pauw, "A method of measuring the resistivity and Hall coefficient on Lamellae of arbitary shape," *Philips Technical Review*, 20, 220-224 (1958).

[67] O. Bierwagen, T. Ive, C. G. Van de Walle, and J. S. Speck, "Causes of incorrect carrier-type identification in van der Pauw–Hall measurements," *Applied Physics Letters*, 93, 242108 (2008).

[68] http://en.wikipedia.org/wiki/SQUID.

[69] http://en.wikipedia.org/wiki/Time-resolved_spectroscopy.

[70] B. J. W. Reiner *et al*., "Crystalline oxides on silicon," *Advanced Materials*, 22, 2919-2938 (2010).

[71] J. Son *et al*., "Epitaxial $SrTiO_3$ films with electron mobilities exceeding 30,000 $cm^2V^{-1}s^{-1}$," *Nature Materials*, 9, 482-484 (2010).

[72] R. von Helmolt, J. Weeker, B. Holzapfel, L. Schultz, and K. Samwer, "Giant negative magnetoresistance in perovskitelike $La_{2/3}Ba_{1/3}MnO_X$ ferromagnetic films," *Physical Review Letters*, 71, 2331-2333 (1993).

[73] T. Riste, E. J. Samuelsen, and K. Otnes, "Critical behaviour of $SrTiO_3$ near the 105 K phase transition," *Solid State Communications*, 9, 1455-1458 (1971).

[74] J. Mannhart, D. H. A. Blank, H. Y. Hwang, A. J. Millis, and J.-M. Triscone, "Two-dimensional electron gases at oxide interfaces," *MRS Bulletin*, 33, 1027-1034 (2008).

[75] K. V. Yumashev, P. V. Prokoshin, A. M. Malyarevich, and V. P. Mikhailov, "Transient bleaching/ induced absorption in reduced $SrTiO_3$ under picosecond excitation," *Journal of the Optical Society of America B*, 14, 415-419 (1997).

[76] S. S. A. Seo *et al*., "Multiple conducting carriers generated in $LaAlO_3/SrTiO_3$ heterostructures," *Applied Physics Letters*, 95, 082107 (2009).

[77] S. K. Sundaram and E. Mazur, "Inducing and probing non-thermal transitions in semiconductors using femtosecond laser pulses," *Nature Materials*, 1, 217-224 (2002).

[78] G. J. C. L. Bruls, J. Bass, A. P. van Gelder, H. van Kempen, and P. Wyder, "Linear magnetoresistance caused by sample thickness variations," *Physical Review Letters*, 46, 553-555 (1981).

[79] G. J. C. L. Bruls, J. Bass, A. P. van Gelder, H. van Kempen, and P. Wyder, "Linear magnetoresistance due to sample thickness variations: applications to Aluminum," *Physical Review B*, 32, 1927-1939 (1985).

[80] S. Zhang *et al*., "Electronic manifestation of cation-vacancy-induced magnetic moments in a transparent oxide semiconductor: Anatase Nb:TiO_2," *Advanced Materials*, 21, 2282-2287 (2009).

[81] S. Seri, E. Shimshoni, S. Paetel, J. Mannhart, and L. Klein, "Angular dependence of the magnetoresistance of the $SrTiO_3/LaAlO_3$ interface," *IEEE Transactions on Magnetics*, 46, 1630-1632 (2010).

[82] F. J. Wong, R. V. Chopdekar, and Y. Suzuki, "Disorder and localization at the $LaAlO_3/SrTiO_3$ heterointerface," *Physical Review B*, 82, 165413 (2010).

[83] M. Ben Shalom *et al*., "Anisotropic magnetotransport at the $SrTiO_3/LaAlO_3$ interface," *Physical Review B*, 80, 140403(R) (2009).

[84] O. N. Tufte and E. L. Stelzer, "Magnetoresistance in semiconducting strontium titanate," *Physical Review*, 173, 775-777 (1968).

[85] Z. S. Popovic, S. Satpathy, and R. M. Martin, "Origin of the two-dimensional electron gas carrier density at the $LaAlO_3$ on $SrTiO_3$ interface," *Physical Review Letters*, 101, 256801 (2008).

[86] E. Dagotto, T. Hotta, and A. Moreo, "Colossal magnetoresistant materials: the key role of phase separation," *Physics Reports*, 344, 1-153 (2001).

[87] V. B. Shenoy, D. D. Sarma, and C. N. R. Rao, “Electronic phase separation in correlated oxides: the phenomenon, its present Status and future prospects,” *Chem. Phys. Chem.*, 7, 2053-2059 (2006).

[88] A. Moreo, S. Yunoki, and E. Dagotto, “Phase separation scenario for manganese oxides and related materials,” *Science*, 283, 2034-2040 (1999).

[89] M. Uehara, S. Mori, C. H. Chen, and S.-W. Cheong, “Percolative phase separation underlies colossal magnetoresistance in mixed-valent manganites,” *Nature*, 399, 560-563 (1999).

[90] G. Allodi, R. D. Renzi, and G. Guidi, “Electronic phase separation in lanthanum manganites: evidence from ^{55}Mn NMR,” *Physical Review B*, 56, 6036-6046 (1997).

[91] V. J. Emery and S. A. Kivelson, “Frustrated electronic phase separation and high-temperature superconductors,” *Physica C*, 209, 597-621 (1993).

[92] M. Breitschaft *et al*., “Two-dimensional electron liquid state at $LaAlO_3$-$SrTiO_3$ interfaces,” *Physical Review B*, 81, 153414 (2010).

[93] C. Bell, S. Harashima, Y. Hikita, and H. Y. Hwang, “Thickness dependence of the mobility at the $LaAlO_3/SrTiO_3$ interface,” *Applied Physics Letters*, 94, 222111 (2009).

[94] F. A. Stevie and R. G. Wilson, “Relative sensitivity factors for positive atomic and molecular ions sputtered from Si and GaAs,” *Journal of Vacuum Science and Technology A*, 9, 3064-3070 (1991).

[95] R. C. Neville, B. Hoeneisen, and C. A. Mead, “Permittivity of strontium titanate,” *Journal of Applied Physics*, 43, 2124-2131 (1972).

[96] P. Delugas, A. Filippetti, V. Fiorentini, D. l. Bilc, D. Fontaine, and P. Ghosez, “Spontaneous 2-dimensional carrier confinement at the n-type $SrTiO_3/LaAlO_3$ interface,” *Physical Review Letters*, 106, 166807 (2011).

[97] B. Kalisky *et al*., “Critical thickness for ferromagnetism in LaAlO3/SrTiO3 heterostructures,” *arXiv:1201.1063v1*.

[98] C. Bell *et al*., “Dominant mobility modulation by the electric field effect at the $LaAlO_3/SrTiO_3$ interface,” *Physical Review Letters*, 103, 226802 (2009).

[99] T. Fix, F. Schoofs, J. L. MacManus-Driscoll, and M. G. Blamire, “Charge confinement and doping at $LaAlO_3/SrTiO_3$ interfaces,” *Physical Review Letters*, 103, 166802 (2009).

[100] Y. Hotta, T. Susaki, and H. Y. Hwang, "Polar discontinuity doping of the $LaVO_3/SrTiO_3$ interface," *Physical Review Letters*, 99, 236805 (2007).

[101] Y. Chen *et al*., "Metallic and insulating interfaces of amorphous $SrTiO_3$-based oxide heterostructures.," *Nano Letters*, 11, 3774-3778 (2011).

[102] Y. Tokura, Y. Taguchi, Y. Okada, Y. Fujishima, and T. Arima, "Filling dependence of electronic properties on the Verge of metal-Mott-insulator transitions in $Sr_{1-X}La_XTiO_3$," *Physical Review Letters*, 70, 2126-2129 (1993).

[103] N. Nagaosa, J. Sinova, S. Onoda, A. H. Macdonald, and N. P. Ong, "Anomalous Hall effect," *Reviews of Modern Physics*, 82, 1539-1592 (2010).

[104] J. S. Kim *et al*., "Nonlinear Hall effect and multichannel conduction in $LaTiO_3/SrTiO_3$ superlattices," *Physical Review B*, 82, 201407(R) (2010).

[105] H. H. Wieder, "Transport coefficients of InAs epilayers," *Applied Physics Letters*, 25, 206-208 (1974).

[106] J. Biscaras *et al*., "Two-dimensional superconductivity induced by high-mobility carrier doping in $LaTiO_3/SrTiO_3$ hetero-structures," *arXiv:1112.2633v1[cond-mat.supr-con]*.

[107] R. Scherwitzl, S. Gariglio, M. Gabay, P. Zubko, M. Gibert, and J.-M. Triscone, "Metal-Insulator Transition in Ultrathin $LaNiO_3$ Films," *Physical Review Letters*, 106, 246403 (2011).

[108] K. Yoshimatsu *et al*., "Dimensional-crossover-driven metal-insulator transition in $SrVO_3$ ultrathin films," *Physical Review Letters*, 104, 147601 (2010).

[109] J. Burgy, M. Mayr, V. Martin-Mayor, A. Moreo, and E. Dagotto, "Colossal effects in transition metal oxides caused by intrinsic inhomogeneities," *Physical Review Letters*, 87, 277202 (2001).

[110] S. C. Tidrow *et al*., "New Substrates For HTSC Microwave Devices," *IEEE Transactions on Applied Superconductivity*, 7, 1766-1768 (1997).

[111] D. Nuzhnyy *et al*., "Infrared phonon spectroscopy of a compressively strained (001) $SrTiO_3$ film grown on a (110) $NdGaO_3$ substrate," *Journal of Physics: Condensed Matter*, 23, 045901 (2011).

[112] "JCPDS Powder Diffraction File: Sets 27 to 2872 (Card 27–204, JCPDS International Centre for Diffraction Data, Swarthmore, 1986)."